NUMERICAL STUDY OF BIO-FLUIDS AND MASS TRANSFER PROCESSES THROUGH MEMBRANES

Jonathan Florez Giraldo

NUMERICAL STUDY OF BIO-FLUIDS AND MASS TRANSFER PROCESSES THROUGH MEMBRANES

Doctoral Thesis

Jonathan Florez Giraldo

Tarragona, June 2018

UNIVERSITAT ROVIRA I VIRGILI
NUMERICAL STUDY OF BIO-FLUIDS AND MASS TRANSFER PROCESSES THROUGH MEMBRANES
Jonathan Florez Giraldo

NUMERICAL STUDY OF BIO-FLUIDS AND MASS TRANSFER PROCESSES THROUGH MEMBRANES

Doctoral Thesis

UNIVERSITAT ROVIRA i VIRGILI

Jonathan Florez Giraldo

Supervised by:
Dr. Anton Vernet Peña
Dr. Clara Salueña
Dr. Salvatore Cito

Mechanical Engineering Department

Tarragona, June 2018

UNIVERSITAT ROVIRA I VIRGILI
NUMERICAL STUDY OF BIO-FLUIDS AND MASS TRANSFER PROCESSES THROUGH MEMBRANES
Jonathan Florez Giraldo

I state that the present study, entitled:

Numerical study of bio-fluids and mass transfer processes through membranes.

Presented by **Jonathan Florez Giraldo** for the award of the degree of Doctor, has been carried out under our supervision at the Department of Mechanical Engineering of Rovira i Virgili university.

Tarragona, 12 June 2018

Supervised by:

Dr. Anton Vernet **Dr. Clara Salueña** **Dr. Salvatore Cito**

Associate professors of Mechanical Engineering Department in Universitat Rovira i Virgili. Research Group ECOMMFIT.

UNIVERSITAT ROVIRA I VIRGILI
NUMERICAL STUDY OF BIO-FLUIDS AND MASS TRANSFER PROCESSES THROUGH MEMBRANES
Jonathan Florez Giraldo

Abstract

Blood rheology (haemorheology) plays a key role in tissue perfusion and its alteration from physiological conditions is often the main cause of cardiovascular pathologies. Therefore, the study of blood velocity profiles and wall shear stress distribution along micro-vessels is important in the field of cardiovascular diseases research. Recent advances in organ-on-a-chip highlighted the possibility of using artificial lung-on-chips which have been developed to replace the respiratory functions of the human lungs in pharmaceutical tests. We studied micro-separation processes through micro-porous membranes developing a numerical tool able to model the behavior of lung-on-a-chip micro-devices in both two and three dimensional geometries, where an artificial membrane is separating two channels with two different fluids and thus two different flow regimes. To face the multiscale nature of the problem, the numerical couples into a hybrid LBM-FD model computed on a non-uniform geometrical grid. The code models computes mass transfer processes occurring within non-Newtonian flows. After a thorough validation and verification of the code, we used the code to find correlations of the non-dimensional numbers involved in mass transfer processes and the dependence on porosity, and the study of concentration profiles under steady (pipe flow) and the beginning of the study in non-steady (Womersley flow) conditions.

The conventional Lattice Boltzmann model (LBM) is used to solve the isothermal Navier-Stokes and continuity equations. The non-Newtonian nature of blood is accounted by using a separated module which correlates the kinematic viscosity to the local shear rate computed by the LBM method. For simplicity, we focused our study in the reproduction of the blood flow behavior using the well-known truncated power-law model, but the code can be easily modified to reproduce any non-Newtonian flow model. The length of the transition zone for Non-Newtonian fluids in the 2D velocity-driven flow case is not constant. Flows with high shear-thinning behavior $n \to 0$ have a faster convergence, producing smaller transition zones. While, the velocity field in the pulsatile flow is well-reproduced compared to Womersley flow case ($n = 1$, Newtonian fluid). The velocity profiles are independent of the Womersley number (unlike the Newtoninan case), only their magnitude was reduced significantly, using the parameters for the power-law blood flow model found by Kim et al. ($k = 0.00927$ (Pa s^n), $n = 0.828$). Also the maximum value of the normalized velocity developed in a

complete period is directly related with the Reynolds number, meanwhile a reduction in the Womersley number means an increase of the normalized velocity.

Lax-Wendroff (L-W) finite differences solver (FD) is used to model the evolution of a passive scalar (concentration). The FD method was tested simulating two conventional cases: first, the advection-diffusion of a Gaussian pulse, and second, the heat transfer by advection-diffusion in a moving bar. In both cases, the results shows the capability of the FD method to reproduce this kind of process with a low computational cost

Finally, A LBM-FD hybrid routine that couples the two models has been developed. Unlike the LBM grid, the finite difference model is implemented in a non-uniform grid (stretching grid) to improve the stability and accuracy of the method in high gradients zones. The difference between both model grids was solved implementing a bilinear interpolation method. The LBM-FD hybrid code was validated solving the Graetz-Leveque problem of boundary layer mass flux. The results reproduce accurately the mean Sherwood number measurements of the Holzbecher study [21]. However, we observed that only the highest mesh refinement ($r = 1.1$) is capable to reproduce accurate results for Pe $\gtrsim 10^6$ showing the advantages provided by the non-uniform grid.

Once validated, the LBM-FD hybrid model was used to study the mass transport through a hydrophobic micro-porous membrane located in-between a co-current flow passing through rectangular channels, which is similar to the micro-device used in Lung-On-a-Chip research. This code has been used to perform a parametric study to find the empirical correlation between Péclet number in the permeate channel and the mass transfer processes across the membrane which is quantified by mean of Sherwood number. The correlations in the two-dimensional micro-device reproduce correctly the linear scaling law of $< Sh >$ with the number of pores. The correlations give a power value equal to $1/3$ for the scaling exponent of the average Sherwood number with Pe (Note that this corresponds to the value found for the Graetz-Leveque problem). This analysis has been extended to 2D and 3D models. In the three-dimensional case, we compared the results obtained using the power-law flow with a shear-thinning degree of $n = 0.7$ against the results obtained using the Newtonian hypothesis ($n = 1$). The non-Newtonian case showed 5% increase of mass transfer ($< Sh >$) over the Newtonian case.

Acknowledgements

I would like to thank to my advisors Anton, Clara and Salvatore, because they were always involved to take the project forward, without their help and understanding it would have been impossible to finish my work.

I also want to thank to the workers of the URV Mechanical Engineering Department, specially to the ECoMMFIT research group for giving me the opportunity to carry out my studies with their support. Thanks to my office colleagues to have a lot of patience and always have a smile for me.

Finally, I want to thank all the support received by my family, they have always been and will continue to be my motivation to move forward.

UNIVERSITAT ROVIRA I VIRGILI
NUMERICAL STUDY OF BIO-FLUIDS AND MASS TRANSFER PROCESSES THROUGH MEMBRANES
Jonathan Florez Giraldo

Contents

List of Figures

List of Tables

Chapter 0 x

Chapter 1

Introduction

Advances in the field of haemorheology (science of the deformation and flow of materials applied to the study of flow properties of blood and its formed elements) have contributed to the fundamental understanding of the changes in the rheological properties of blood and its elements due to pathological disturbances, and are based on the evidence that they might be the primary cause of many cardiovascular diseases. Deviations in haemorheological parameters may affect tissue perfusion and be manifested as circulatory problems. Basically, pathologies with haematological origin like leukemia, haemolytic anemia, thalassemia or pathologies associated with the risk factors of thrombosis and atherosclerosis like myocardial infarction, hypertension, strokes or diabetes are mainly related to disturbances of local homeostasis. Therefore, the mathematical and numerical study of powerful, yet simple, constitutive models that can capture the rheological behavior of blood over a range of flow conditions is recognized as an important tool for clinical diagnosis. [13, 33].

Blood is a complex mixture of cells, proteins, lipoproteins, and other formed elements suspended in plasma. An understanding of the velocity profile of blood flow and the distribution of wall shear stress in small vessels of the microcirculation system is of vital important for preventing cardiovascular diseases [17, 1]. The most important rheological property of blood that influences its motion is the apparent viscosity. As the shear rate is low ($< 100\ s^{-1}$), the major formed elements, red blood cells (RBCs), aggregate and form rouleaux. Rouleaux aggregations in plasma are responsible for the shear-thinning behavior and are the main causes of the non-Newtonian behavior of the blood flows

[27, 16]. The apparent viscosity of a non-Newtonian fluid is not constant at a given temperature and pressure but a function of the shear rate. There are various non-Newtonian models developed for characterizing the shear-thinning behavior.

The development of artificial lungs that replace the respiratory functions of the human lungs or that can mimic the behavior of the respiratory system in the presence of toxins, has been of great interest in the treatment of patients suffering from severe lung diseases. In the same way, it has been used by pharmaceuticals to reduce the time and costs in the experiments performed on animals. One of the most important applications performed in the last years is known as Lung-On-a-Chip [11]. Dongeun et al. constructed a biomimetic micro-system that reconstitutes the critical function alveolar-capillary interface of the human lung. This bioinspired micro-device reproduces complex integrated organ-level responses to bacteria and inflammatory cytokines introduced into the alveolar space. This micro-device has a co-current air-blood flow passing through rectangular conducts as used in separation processes. The channels are divided by a thin interleaved micro-porous PDMS membrane where they introduced human aleolar epithelial cells and microvascular endothelial cells into their respective channels, where they attached to opposite surfaces of the membrane and formed intact monolayers composed of cells.

Simulations of micro-separation processes through micro-porous membranes become relevant in the design and manufacture of this micro-devices with the aim of predicting the best conditions to ensure greater efficiency in this processes. On the other hand, the first step on the development of a tool able to simulate the behaviors found in a biological micro-devices will expand the understanding of this complex systems.

Microfluidic mass-transfer experimental models have been applied in a wide range of studies to test experimentally the performance of membrane contactors, and most of the numerical models are oriented to the treatment of the membrane as a continuum medium [15, 14, 34]. One of the problems for this type of simulations is the multi-scale character of the mechanisms involved. Even in those problems where the chemical kinetics can be neglected, small diffusivities (high Schmidt numbers) and the geometrical details of the micro-scale (porosity and tortuosity) impose extremely high demands on the flow solvers, even at the typical low Reynolds numbers characterizing microfluidics. Since realistic problems often involve more than one scale, it is not easy to solve a

multi-scale problem using only one numerical method.

In this work, a hybrid model was built using a well-established methodology to capture phenomena occurring at different scales, in order to study the mass transfer through a hydrophobic micro-porous membrane between a co-current blood-air flow passing through rectangular channels, taking as a reference the micro-device used in Lung-On-a-Chip research [11]. For this purpose, we selected the Lattice Boltzmann Method (LBM) to reproduce the hydrodynamics of Newtonian (air) and non-Newtonian (blood) flows. The LBM is a simplified kinetic equation to simulate fluid flows and has been applied to general problems including hydrodynamics [46, 37], magnetohydrodynamics [38, 5], and aerodynamics [41, 42], as well as in areas relevant to blood flow simulation such as in steady and pulsating flow [23, 58], and flows with complex boundaries [36], where the LBM has been shown to be suitable for modeling a number of features that are important to arterial hemodynamics, due to its kinetic essence, the LBM allows straightforward calculations of the local shear rate to the second-order accuracy.

On the other hand, a Lax-Wendroff (L-W) finite differences solver (FD) is used to simulate the evolution of a passive scalar (concentration). Simplifications were assumed to avoid stability problems at high Schmidt numbers, since the mass transfer boundary layer surrounding the membrane becomes thinner as the Schmidt number increases. To be able to numerically solve high concentration gradients in the direction normal to the flow, a highly refined grid is needed in the vicinity of the membrane. This method offers the advantage of an easy implementation of non-uniform meshes, which allows the accurate modeling of the material boundary layer at high Péclet numbers. A geometric series was used at the upper half of the channel. By symmetry, the mesh is built in the bottom half for further refinement at the channel walls.

A LBM-FD routine was designed to couple both methods. The development of a LBM module to compute the value of the apparent viscosity from the value of the shear rate (non-Newtonian fluid requirement) in each node was realized. Additionally, the inclusion of the generalized multiple-relaxation-time LBM (MRT-LBM) offers a robust tool to affront the non-Newtonian simulation challenges compared with the conventional LBM. A non-uniform grid (stretching grid) was implemented in the L-W method to have a better resolution and in turn more stability and accuracy in high gradients areas. The difference between grids was mapped by means of a bilinear interpolation applied over the

velocity field, being this field the link between both methods. The LBM-FD hybrid code was validated solving the Graetz-Leveque problem of boundary layer mass flux. Finally, the hybrid model reproduced the mass transport through a hydrophobic micro-porous membrane between a co-current blood-air flow micro-device and correlations between Péclet and mean Sherwood numbers was found.

1.1 Objectives of the thesis

- To build a LBM that reproduces the physical and mechanical characteristics of non-Newtonian fluids (choosing the power-law model), with the aim of simulate blood flow in micro-devices.
- To show the ability of the LBM to simulate time-dependent blood flows, focusing in flows produced in arteries and veins as the pulsatile flow.
- To build a finite differences model that reproduces the mass transport in a flow (resolving the advection-diffusion equation) and testing the ability to solve this type of processes properly.
- To design a routine that involves both methods properly, making the necessary numerical developments to generate a robust LBM-FD hybrid model (non-uniform grid and 2D interpolation velocity field).
- To use the validated hybrid model to reproduce the mass transport through a hydrophobic micro-porous membrane between a co-current blood-air flow micro-device.

1.2 Document structure

The present document is organized as follows:

- Chapter 2 introduces the lattice Boltzmann method and its basic concepts, models, boundary schemes and stability conditions.
- Chapter 3 shows the basic concepts of the Lax-Wendroff method and its equations to three-dimensional grid considering the implementation of a non-uniform grid.

- In chapter 4 an explanation about the non-Newtonian behavior and different constitutive equations used to model this kind of fluids are described. Additionally, the relations between the blood flow and non-Newtonian fluids are written, giving relevance to the truncated power-law model and the parameters experimentally found to reproduce blood flow.
- Chapter 5 shows the implementation of the MRT-LBM in 2D and 3D steady state power-law flow to validate the non-Newtonian simulation module comparing with analytical solutions. This implementation was made using two different ways to produce a gradient-pressure flow (force-driven flow and velocity-inlet flow) showing the benefits and limits of both.
- Chapter 6 analyzes the ability of the MRT-LBM to reproduce non-Newtonian flows with time-dependent conditions (pulsatile flow) and makes a first description of the macroscopic behavior obtained with the truncated power-law model in a pulsatile flow.
- Chapter 7 presents the validation of the Lax-Wendroff method applying our code to the simulation of two problems: first, the advection-diffusion of a Gaussian pulse, and second, the heat transfer by advection-diffusion in a moving bar.
- Chapter 8 explains the hybrid model routine design, and the implementations made to couple both methods. The hybrid model was validated solving the Graetz-Leveque problem of boundary layer mass flux.
- In chapter 9, results are shown on the simulation of mass transport through a hydrophobic micro-porous membrane located in-between a co-current flow using our LBM-FD hybrid model, similar to the micro-device used in Lung-On-a-Chip research. This code has been used to perform a parametric study to find the empirical correlation between the Péclet number in the permeate channel and the mass transfer processes characterized by the average Sherwood number $< Sh >$ across the membrane.
- Chapter 10 summarizes all the remarks and conclusions obtained in this work.

Chapter 2

Lattice Boltzmann Method

The Lattice Boltzmann method (LBM) is presented as an alternative way to solve partial differential equations, and is derived from the Lattice Gas Cellular Automata (LGCA). The LBM is more stable numerically, implicitly includes the convergence criteria, and is easily suited to complex or time-varying boundary conditions. This method has been widely used in simulations of fluids, with great relevance in areas such as hydrodynamics [46, 37], aerodynamics [41, 42] and magnetohydrodynamics [38, 5], among others.

There are different methods to solve a set of partial differential equations that work in different scales. On a macro-scale, there are two ways of address the problem, i) in a continuum approach, ordinary or partial differential equations can be resolved by applying the conservation of energy, mass and momentum, to an infinitesimal control volume; ii) difficulties like nonlinearity, complex boundary conditions and complex geometry mostly appear trying to solve the system analytically. On the other hand, different methods exist for discretizing and converting the system of partial differential equations into a set of algebraic equations that can be solved iteratively until convergence (finite difference, finite volume, finite element, etc.) [24, 9].

On a micro-scale, the medium (gas or liquid) can be considered as made of small particles interacting (colliding) with each other. Molecular dynamics methods identify the forces acting on the particles and solve the Newton's second law (conservation of momentum) to find the position and the velocity of each particle in the next step of time. Although this method has a very strong physical

view, tracing the position and velocity of each particle in a fluid, along with the calculation of the macroscopic quantities (such as pressure, temperature, energy, etc.) has a high computational cost [48].

In the middle of these scales (meso-scale), the LBM emerges as an alternative that considers the behavior of a collection of particles and his evolution in the system as a unit, maintaining the advantages of both macroscopic and microscopic approaches, with manageable computer resources. The density of the collection of particles is represented by a distribution function. The distribution function acts as a representative for the collection of particles in the meso-scale.

2.1 The Boltzmann equation

The system under consideration in the classical kinetic theory of gases is a dilute gas of N particles enclosed in a box of volume V, where every particle has a well-defined position and momentum. The molecules interact with each other through collisions whose nature is specified through a given differential scattering cross section. We are not interested in the motion of each molecule in detail. Instead, we are interested in the distribution function $f(\vec{x}, \vec{v}, t)$, such that, $f(\vec{x}, \vec{v}, t)d^3xd^3v$, is the number of molecules which, at time t, have positions lying within a volume d^3x about $\vec{x}$ and velocity lying within a velocity-space element d^3v about $\vec{v}$. The aim of kinetic theory is to find the distribution function $f(\vec{x}, \vec{v}, t)$ for a given form of molecular interaction. The limiting form of $f(\vec{x}, \vec{v}, t)$ as $t \to \infty$ would then contain all the equilibrium properties of the system [22].

To fulfill this aim, our first task is to obtain the evolution equation for the distribution function. The moments of the distribution function are related to the macroscopic variables such as fluid density ρ, fluid velocity vector $\vec{u}$ and internal energy E as

$$\rho(\vec{x}, t) = \int f(\vec{x}, \vec{v}, t)d\vec{v} \quad , \tag{2.1}$$

$$\rho\vec{u}(\vec{x}, t) = \int \vec{v} f(\vec{x}, \vec{v}, t)d\vec{v} \quad , \tag{2.2}$$

$$\rho E(\vec{x}, t) = \int \frac{|\vec{v}|^2}{2} f(\vec{x}, \vec{v}, t)d\vec{v} \quad , \tag{2.3}$$

and the second order moment gives the momentum flux tensor,

$$\rho u_\alpha u_\beta + p\delta_{\alpha\beta} - \sigma_{\alpha\beta} = \int v_\alpha v_\beta f d\vec{v} = \Pi_{\alpha\beta} \quad . \tag{2.4}$$

The particles contained in a control volume $d^3x d^3v$ at time t will be found inside $d^3x' d^3v'$ at time $t + \delta t$. In the absence of collisions, the number of particles in both control volumes at different times will be the same, but if there are collisions, a collision term must be included in the relation,

$$f(\vec{x} + \vec{v}\delta t, \vec{v} + \vec{F}/m\delta t, t + \delta t) = f(\vec{x}, \vec{v}, t) + \Omega(f)\delta t \quad , \tag{2.5}$$

Expanding the left-hand side to the first order in δt, we obtain the evolution equation for the distribution function as we let $\delta t \to 0$:

$$\frac{\partial f}{\partial t} + \vec{v} \cdot \nabla f + \frac{\vec{F}}{\rho} \cdot \nabla_{\vec{v}} f = \Omega(f) \quad , \tag{2.6}$$

The Boltzmann equation concerns the behavior of a thermodynamic system in an equilibrium or non-equilibrium state. The evolution of the distribution function in time (first term of Eq. 2.6) depends on three factors that modify f. First, the advection of particles, second, the total external force which depends on the fluid density ρ, and third, the collisions between particles (right hand side term in Eq. 2.6).

We now analyze the nature and applicability of the Boltzmann equation. The zeroth order moment of Eq. 2.6 must recover the mass conservation equation,

$$\frac{\partial}{\partial t} \int f d\vec{v} + \nabla \cdot \int \vec{v} f d\vec{v} + \frac{\vec{F}}{\rho} \cdot \int \nabla_{\vec{v}} f d\vec{v} = \int \Omega(f) d\vec{v} \quad . \tag{2.7}$$

Since the integral $\int \nabla_{\vec{v}} f d\vec{v} = 0$, and the collision operator is invariant, by combining Eqs. 2.1 and 2.2, the zeroth order moment of Eq. 2.6 is the continuity equation,

$$\frac{\partial}{\partial t} \int f d\vec{v} + \nabla \cdot \int \vec{v} f d\vec{v} = \int \Omega(f) d\vec{v} = \frac{\partial \rho}{\partial t} + \nabla(\rho \vec{u}) = 0 \quad . \tag{2.8}$$

Now using the same procedure, for the first order moment of the Boltzmann equation we obtain

$$\frac{\partial}{\partial t} \int \vec{v} f d\vec{v} + \nabla \cdot \int v_\alpha v_\beta f d\vec{v} + \frac{\vec{F}}{\rho} \cdot \int v_\alpha \nabla_{v_\beta} f d\vec{v} = \int \vec{v} \Omega(f) d\vec{v} \quad , \tag{2.9}$$

where the integral $\int v_\alpha \nabla_{v_\beta} f d\vec{v} = -\int \frac{\partial v_\alpha}{\partial v_\beta} f d\vec{v} = -\rho\delta_{\alpha\beta}$, $\delta_{\alpha\beta}$ being the Kronecker delta.

The equation that results from combining Eq. 2.2, Eq. 2.4 and Eq. 2.9 leads to

$$\frac{\partial \rho\vec{u}}{\partial t} + \nabla \cdot \Pi_{\alpha\beta} - \vec{F} = 0 \quad . \tag{2.10}$$

This latter formulation can be expressed as the Cauchy momentum equation [44]

$$\frac{\partial \rho\vec{u}}{\partial t} + \nabla \cdot \rho u_\alpha u_\beta = -\nabla \cdot \vec{p} + \nabla \cdot \sigma_{\alpha\beta} + \vec{F} \quad . \tag{2.11}$$

2.2 Lattice Boltzmann method

In the LBM, the space is divided by a grid and the time moves on discrete steps. Each node of the lattice has associated a set of discrete microscopic velocities denoted by $\vec{v}_i$, that link with the neighboring nodes. To each microscopic velocity on the lattice, we associate a distribution function $f_i(\vec{x}, t)$ which describes the probability of streaming in one particular direction. The macroscopic variables (as density and flow velocity) are calculated from the distribution functions in each node. In one time step, the distribution functions are recombined inside each node following the collision term of the lattice Boltzmann equation (different collision terms are described in Sec. 2.3), and then streamed to the neighboring nodes depending on these velocity directions.

2.2.1 Lattice Arrangements

The common terminology used in LBM regarding the dimension of the problem and the number of microscopic velocities used is $DdQq$, where d represent the dimension of the problem (1 for 1D, 2 for 2D and 3 for 3D) and q refers to number of velocities or linkages. For simulations in one dimension the $D1Q2$, $D1Q3$ and $D1Q5$ arrangements are frequently used, in two dimensions, $D2Q4$, $D2Q5$ and $D2Q9$ models are the most common. For three dimensional simulations, the usual arrangements are $D3Q15$, $D3Q19$ and $D3Q27$. In the following sections, we use different lattice arrangements for our simulations.

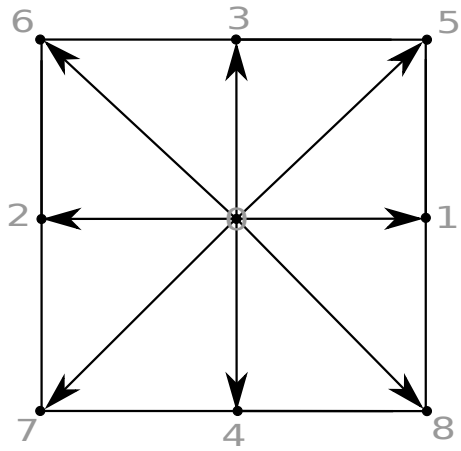

Figure 2.1: **Velocity directions in the $D2Q9$ lattice arrangement.**

D2Q9 model

In the $D2Q9$ model, a particle is restricted to stream along one out of nine possible directions, including the one staying at rest. Figure 2.1 shows a typical lattice node of the $D2Q9$ arrangement. The microscopic lattice velocities are defined as

$$\vec{v}_i = \begin{cases} 0 & for\ i = 0 \\ \hat{i}\|v\|\cos\left(\frac{(i-1)\pi}{2}\right) + \hat{j}\|v\|\sin\left(\frac{(i-1)\pi}{2}\right) & for\ i = 1-4 \\ \hat{i}\|v\|\cos\left(\frac{(i-1/2)\pi}{2}\right) + \hat{j}\|v\|\sin\left(\frac{(i-1/2)\pi}{2}\right) & for\ i = 5-8 \end{cases} . \quad (2.12)$$

In a uniform grid, all the lattice nodes must be equidistant and additionally, a grid must fulfill symmetry in order to satisfactorily recover from the moments, the macroscopic equations. In a discretized formalism, this is done by means of the weighting factor w_i, this weights must fulfill the following properties

$$\sum_i = w_i v_{i\alpha} = 0 \quad , \quad \sum_i = w_i v_{i\alpha} v_{i\beta} = \frac{1}{3}\delta_{\alpha\beta} \quad , \quad \sum_i = w_i v_{i\alpha} v_{i\beta} v_{i\gamma} = 0 \quad (2.13)$$

$$\sum_i = w_i v_{i\alpha} v_{i\beta} v_{i\gamma} vi\delta = \frac{1}{9}(\delta_{\alpha\beta}\delta_{\gamma\delta} + \delta_{\alpha\gamma}\delta_{\beta\delta} + \delta_{\alpha\delta}\delta_{\beta\gamma}) \quad (2.14)$$

The weight factors for the $D2Q9$ model are

$$w_i = \begin{cases} 4/9 & for\ i = 0 \\ 1/9 & for\ i = 1-4 \\ 1/36 & for\ i = 5-8 \end{cases} . \tag{2.15}$$

D3Q19 model

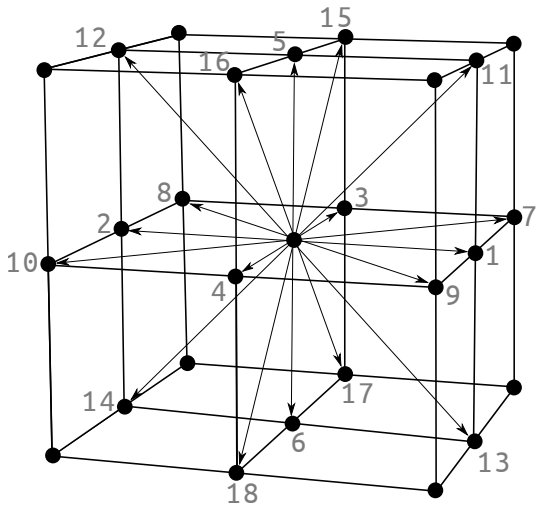

Figure 2.2: **Velocity directions in the $D3Q19$ lattice arrangement.**

The $D3Q19$ model has 19 microscopic velocity directions including the zero velocity vector. Equation 2.16 shows the velocities

$$\vec{v}_i = \begin{cases} (0,0,0) & for\ i = 0 \\ \|v\|(\pm 1,0,0), \|v\|(0,\pm 1,0), \|v\|(0,0,\pm 1) & for\ i = 1-6 \\ \|v\|(\pm 1,\pm 1,0), \|v\|(\pm 1,0,\pm 1), \|v\|(0,\pm 1,\pm 1) & for\ i = 7-18 \end{cases} \tag{2.16}$$

and the weight factors are

$$w_i = \begin{cases} 1/3 & for\ i = 0 \\ 1/18 & for\ i = 1-6 \\ 1/36 & for\ i = 7-18 \end{cases} . \tag{2.17}$$

Macroscopic variables like the local density ρ, and the velocity $\vec{u}$ can be recovered from the distribution functions at each node,

$$\rho = \sum_i f_i \qquad , \qquad \rho u_\alpha = \sum_i f_i v_{i\alpha} \quad . \tag{2.18}$$

By performing a Chapman-Enskog expansion, consisting in a Taylor series expansion of the left hand side of the lattice Boltzmann equation (Eq. 2.25 below), plus a perturbative first order expansion in space and second order in time of the distribution functions, using the Eqs. 2.18, we can recover the Cauchy momentum equation (see Eq. 2.11).

2.2.2 Equilibrium distribution function

Determining a suitable local equilibrium function plays an essential role in the LBM. This function relates to the differential equation being resolved, by means of the lattice Boltzmann equation. According to the theory, in a system of particles in local equilibrium state, there is no significant redistribution of density and momentum, which means, that the distribution function in equilibrium remains unchanged over time. In other words, the collision operator $\Omega(f)$ should be zero. Hence, the Boltzmann equation is expressed as

$$\frac{\partial f}{\partial t} + \vec{v} \cdot \nabla f = \Omega(f) = 0 \quad . \tag{2.19}$$

For the case of a two-dimensional ideal gas, the solution of this equation is known as the Maxwell-Boltzmann distribution:

$$f^{eq}(\rho, \vec{v}, \vec{u}) = \frac{\rho}{2\pi RT} \exp\left(-\frac{(\vec{v}-\vec{u})^2}{2RT}\right) \quad . \tag{2.20}$$

Under the assumption that f^{eq} is a normal distribution, the speed of sound is $(c_s = \sqrt{RT})$, the standard deviation. Thus the Maxwell-Boltzmann distribution for isothermal systems (T = constant) is:

$$f^{eq}(\rho, \vec{v}, \vec{u}) = \frac{\rho}{2\pi c_s^2} \exp\left(-\frac{(\vec{v}-\vec{u})^2}{2c_s^2}\right) \quad . \tag{2.21}$$

Developing an expansion of the velocity in Eq. 2.21 up to second order, at low Mach numbers ($Ma = u/c_s \leq 0.3$) and by means of a Gauss-Hermite

quadrature, the continuum velocity space can be converted to a discrete set of velocities (see [19]),

$$f_i^{eq}(\rho,\vec{u}) = \rho\omega_i\left(1+\frac{\vec{v}\cdot\vec{u}}{c_s^2}+\frac{(\vec{v}\cdot\vec{u})^2}{2c_s^4}+\frac{\vec{u}\cdot\vec{u}}{2c_s^2}\right) \quad , \tag{2.22}$$

where the exponential term that arises from the expansion is linearized in the weights ω_i. The use of this local equilibrium distribution function in the lattice Boltzmann equation (as will be seen in the next section) can recover the Navier-stokes equations.

There is an alternative way, which assumes that an equilibrium function can be expressed as a power series in the macroscopic velocity $\vec{u}$, that allows the use of the LBM to solve different systems of partial differential equations. The method to obtain the equilibrium functions in a general way is explained in [59].

2.3 Lattice Boltzmann equation

For numerical implementations of the Boltzmann equation without considering external forces

$$\frac{\partial f}{\partial t}+\vec{v}\cdot\nabla f = \Omega(f) \quad , \tag{2.23}$$

a finite difference discretization is applied to time and phase space variables. The discretization in the phase space is performed on a square lattice with uniform grid spacing $\Delta x = \Delta y = \Delta z$, where a constant time step Δt is imposed. First order finite differences and a forward time stepping applied on Eq. 2.23 results in

$$\frac{f_i(\vec{x},t+\Delta t)-f_i(\vec{x},t)}{\Delta t}+\vec{v}_i\cdot\frac{f_i(\vec{x}+\vec{v}_i\Delta t,t+\Delta t)-f_i(\vec{x},t+\Delta t)}{\Delta x} = \Omega \quad . \tag{2.24}$$

If the speed of the lattice velocities (a finite set of velocities $\vec{v}_i$) is the same speed of propagation of distribution functions f over the grid (moving one unit lattice spacing at each time step) $\|\vec{v}_i\| = \Delta x/\Delta t$, the Generalized Lattice Boltzmann equation (GLBE) that determines the evolution of the distribution functions in the system is obtained,

$$f_i(\vec{x}+\vec{v}_i\Delta t,t+\Delta t)-f_i(\vec{x},t) = \Omega(f) = -\mathbf{\Omega}(f_i(\vec{x},t)-f_i^{eq}(\vec{x},t))+\omega_i\frac{v_{i\alpha}}{c_s^2}F_\alpha \quad .$$

(2.25)

The last term on the right hand side of Eq. 2.25 is incorporated to reproduce the possible forces acting over the fluid (source of momentum). In incompressible flows, the driving mechanism of the pressure gradient field may be equivalently described by any divergence-free body force [51]. In some flow problems, it may be convenient to replace a driving pressure gradient by effective body forces acting over the fluid [51, 29] because the LBM may lose accuracy when solving pressure fields, due to compressibility errors.

It is difficult to solve the (GLBE) because the collision term is a complex integral of all collision events along the trajectory of the moving volume. It is possible to simplify the collision term under the assumption of sufficiently decoupled events (binary collisions) [4]. Hence, it is possible to approximate the collision operator with a simpler one, without introducing significant errors. This operator must not only fulfill mass, momentum and energy conservation, but also approach the distribution functions towards their local equilibrium state f_i^{eq}.

Different approaches have been developed to introduce a simplified version of the collision term in the GLBE. Each one offers some advantages with respect to the others. The choice of the approach to use in the simulations will depend on the physical conditions of the problem to be solved. Two of the most common used are the Bhatnagar-Gross-Krook (BGK) and Multiple Relaxation Time (MRT) collision terms.

2.3.1 BGK collision term

A simple linearized version of the collision operator, which relaxes towards the local equilibrium using a single relaxation time is the Bhatnagar-Gross-Krook (BGK) model,

$$\Omega = \omega(f_i^{eq} - f_i) = \frac{1}{\tau}(f_i^{eq} - f_i) \quad , \tag{2.26}$$

It can be interpreted as the tendency of the distribution functions f_i to approach its equilibrium state f_i^{eq} after a time τ. This process is also called relaxation towards equilibrium, and τ is therefore denoted as the relaxation parameter or relaxation time. Substituting the BGK collision operator into the GLBE (Eq. 2.25) gives the lattice Boltzmann equation with BGK collision operator

(BGK-LBM):

$$f_i(\vec{x}+v_i\Delta t,\vec{t}+\Delta t)-f_i(\vec{x},t)=\frac{1}{\tau}(f_i^{eq}(\vec{x},t)-f_i(\vec{x},t))+\omega_i\frac{v_{i\alpha}}{c_s^2}F_\alpha \quad . \quad (2.27)$$

2.3.2 MRT collision term

The BGK-LBM is the most common scheme used in LBM due to its simplicity, but it has a main problem: the inability to simulate problems with high Reynolds numbers (using the LBM to solve Navier-Stokes equations), this means that for high Reynolds numbers the relaxation parameter τ approaches 0.5. For this value, the BGK-LBM becomes unstable (see Sec. 2.5). This issue reduces significantly the range of Reynolds numbers suitable to obtain results with this method. This deficiency can be overcome using the Multiple Relaxation time (MRT) collision term. It is worth noting that this generalization of the BGK method provides a greater stability, but does not mean that the method is stable for any Reynolds number: as this value is increased, the stability is lost again. However MRT represents a more robust tool (more stable and accurate) to face simulation challenges in the different research fields of fluid dynamics.

The Lattice Boltzmann equation in a generalized form is 2.25:

$$f_i(\vec{x}+\vec{v}_i\Delta t,t+\Delta t)-f_i(\vec{x},t)=-\mathbf{\Omega}(f_i(\vec{x},t)-f_i^{eq}(\vec{x},t))+\omega_i\frac{v_{i\alpha}}{c_s^2}F_\alpha \quad , \quad (2.28)$$

where $\mathbf{\Omega}$ is the collision matrix. The collision step in the velocity space is difficult to perform. It is more convenient to perform the collision process in the momentum space. Hence Eq. 2.25 can be transformed into the following form,

$$f_i(\vec{x}+\vec{v}_i\Delta t,t+\Delta t)-f_i(\vec{x},t)=\Omega(f)=-\boldsymbol{M}^{-1}\boldsymbol{S}[\boldsymbol{m}(\vec{x},t)-\boldsymbol{m}^{eq}(\vec{x},t)]+\omega_i\frac{v_{i\alpha}}{c_s^2}F_\alpha \quad . \quad (2.29)$$

For simplicity, we give the corresponding matrix values for the $D2Q9$ model (the MRT-LBM theory for $D3Q19$ can be found in [10]). In Eq. 2.29, $\boldsymbol{S}$ is a diagonal matrix containing the inverse of the relaxation times (some of these will have a direct connection with physical variables, whereas the rest will be used for calibrating the method to make it more stable) for the following moment vector $\boldsymbol{m}(\vec{x},t)$

$$\boldsymbol{m}=(\rho,e,\epsilon,j_x,q_x,j_y,q_y,P_{xx},P_{xy})^T \quad , \quad (2.30)$$

where $m_0 = \rho$ is the density of the fluid, and $m_1 = e$ and $m_2 = \epsilon$ are related with the total energy and the square of the energy respectively. Moreover, $(m_3, m_5) = (j_x, j_y)$ is the momentum in x and y directions, $(m_4, m_6) = (q_x, q_y)$ represents the heat flow in x and y directions and $m_7 = P_{xx}$ and $m_8 = P_{xy}$ are the diagonal and off-diagonal components of the stress tensor respectively. These moments can be divided into conservative quantities $(m_0 = \rho, (m_3, m_5) = (j_x, j_y))$, that can be computed in a traditional way via Eq. 2.18, and non-conservative quantities $(m_1 = e, m_2 = \epsilon, (m_4, m_6) = (q_x, q_y), m_7 = P_{xx}, m_8 = P_{xy})$.

The mapping between velocity and moment spaces can be performed by a linear transformation where the distribution functions can be grouped in a vector $\boldsymbol{f} = (f_0, f_1, f_2, ..., f_8)^T$.

$$\boldsymbol{m} = \boldsymbol{M}\boldsymbol{f} \qquad and \qquad \boldsymbol{f} = \boldsymbol{M}^{-1}\boldsymbol{m} \quad , \tag{2.31}$$

where $\boldsymbol{M}$ is the transformation matrix between both spaces and $\boldsymbol{M}^{-1}$ its inverse. The matrix $\boldsymbol{M}$ for $D2Q9$ is,

$$M = \begin{pmatrix} 1 & 1 & 1 & 1 & 1 & 1 & 1 & 1 & 1 \\ -4 & -1 & -1 & -1 & -1 & 2 & 2 & 2 & 2 \\ 4 & -2 & -2 & -2 & -2 & 1 & 1 & 1 & 1 \\ 0 & 1 & 0 & -1 & 0 & 1 & -1 & -1 & 1 \\ 0 & -2 & 0 & 2 & 0 & 1 & -1 & -1 & 1 \\ 0 & 0 & 1 & 0 & -1 & 1 & 1 & -1 & -1 \\ 0 & 0 & -2 & 0 & 2 & 1 & 1 & -1 & -1 \\ 0 & 1 & -1 & 1 & -1 & 0 & 0 & 0 & 0 \\ 0 & 0 & 0 & 0 & 0 & 1 & -1 & 1 & -1 \end{pmatrix} \quad . \tag{2.32}$$

The inverse of matrix $\boldsymbol{M}$ is

$$M^{-1} = a \begin{pmatrix} 4 & -4 & 4 & 0 & 0 & 0 & 0 & 0 & 0 \\ 4 & -1 & -2 & 6 & -6 & 0 & 0 & 9 & 0 \\ 4 & -1 & -2 & 0 & 0 & 6 & -6 & -9 & 0 \\ 4 & -1 & -2 & -6 & 6 & 0 & 0 & 9 & 0 \\ 4 & -1 & -2 & 0 & 0 & -6 & 6 & -9 & 0 \\ 4 & 2 & 1 & 6 & 3 & 6 & 3 & 0 & 9 \\ 4 & 2 & 1 & -6 & -3 & 6 & 3 & 0 & -9 \\ 4 & 2 & 1 & -6 & -3 & -6 & -3 & 0 & 9 \\ 4 & 2 & 1 & 6 & 3 & -6 & -3 & 0 & -9 \end{pmatrix} \quad , \tag{2.33}$$

where $a = 1/36$. The equilibrium moment $\boldsymbol{m}^{eq}$ is calculated from the equilibrium functions $\boldsymbol{f}^{eq}$. Using the transformation matrix $\boldsymbol{M}$, $\boldsymbol{m}^{eq} = \boldsymbol{M}\boldsymbol{f}^{eq}$ is

$$
\begin{aligned}
m_0^{eq} &= \rho \\
m_1^{eq} &= -2\rho + 3(j_x^2 + j_y^2) \\
m_2^{eq} &= \rho - 3(j_x^2 + j_y^2) \\
m_3^{eq} &= j_x \\
m_4^{eq} &= -j_x \\
m_5^{eq} &= j_y \\
m_6^{eq} &= -j_y \\
m_7^{eq} &= (j_x^2 - j_y^2) \\
m_8^{eq} &= j_x j_y \quad .
\end{aligned}
\tag{2.34}
$$

The inverse of the relaxation times in the diagonal matrix $\boldsymbol{S} = diag(s_i)$, with dimensions $q \times q$ are:

$$
\begin{aligned}
s_0 &= 1.0 \\
s_1 &= \frac{1}{(2\mu' + 0.5)} \\
s_2 &= s_1 \\
s_3 &= 1.0 \\
s_4 &= 1.2 \\
s_5 &= 1.0 \\
s_6 &= S_4 \\
s_7 &= \frac{1}{\tau} \\
s_8 &= s_7 \quad .
\end{aligned}
\tag{2.35}
$$

s_0, s_3 and s_5 are arbitrarily set to 1, because they will not have significance in the simulation, due to the fact that they refer to the conservation of mass and momentum, and the values of these equilibrium moments are always the same ($\boldsymbol{m}^{eq} = \boldsymbol{m}$). The coefficient μ is the bulk viscosity, and both s_1 and s_2 can alternatively be fixed to other values (close to 1) as we assume an incompressible LB model. The values of s_4 and s_6 are chosen like those used by other authors

(e.g. [35, 45]). Finally, we see that s_7 and s_8 are relaxation rates related with the viscosity of the fluid.

As a particular case, the BGK collision model can be recovered from the MRT model by setting all the $\boldsymbol{S}$ diagonal elements to the single relaxation rate $1/\tau$. $\boldsymbol{S} = 1/\tau \boldsymbol{I}$ where $\boldsymbol{I}$ is the identity matrix.

2.4 Chapman-Enskog Analysis

The idea behind the Chapman-Enskog analysis applied to the lattice Boltzmann equation is that different physical phenomena happen on different time scales. While the advection of the fluid is the fastest process, the diffusion of mass, momentum and energy happens on a slower time scale. For this reason, the time derivative is usually split into two parts. One can also extend this approach and take into account more time scales [55],

$$\partial_t = \epsilon \partial_{t_0} + \epsilon^2 \partial_{t_1} + \epsilon^3 \partial_{t_2} + O(\epsilon^4) \quad . \tag{2.36}$$

Since the spatial variations of all processes are of the same order, the gradient is not decomposed, $\nabla = \epsilon \nabla_1$. The distribution functions are expanded about the equilibrium,

$$f_i = f_i^{(0)} + \epsilon f_i^{(1)} + \epsilon^2 f_i^{(2)} + \epsilon^3 f_i^{(3)} + O(\epsilon^4) \quad , \tag{2.37}$$

where $f_i^{(0)} = f^{eq}$ and $\epsilon \ll 1$ can be interpreted as the Knudsen number. The expansions for time, the gradient and the distribution functions are inserted into the Taylor-expanded lattice Boltzmann Eq. 2.25, and the terms are sorted by the powers of ϵ. For recovering the Navier-Stokes equations in terms of ρ and $\vec{u}$, the first and second order equations, and the same equations multiplied by $\vec{v}_i$ are summed over i (for a detailed explanation see [50]). The following four macroscopic equations are obtained,

$$\partial_{t_0} \rho + \nabla \cdot (\rho \vec{u}) = 0, \quad \partial_{t_0} (\rho \vec{u}) + \nabla \cdot \Pi^{(0)} = 0 \quad , \tag{2.38}$$

$$\partial_{t_1} \rho = 0, \quad \partial_{t_1} (\rho \vec{u}) + \left(1 - \frac{1}{2\tau}\right) \nabla \cdot \Pi^{(1)} = 0 \quad , \tag{2.39}$$

where

$$\Pi_{\alpha\beta} = \sum_i v_{i\alpha} v_{i\beta} f_i \quad , \tag{2.40}$$

$$\Pi^{(0)}_{\alpha\beta} = \sum_i v_{i\alpha} v_{i\beta} f^{(0)}_i \quad ,$$

$$\Pi^{(1)}_{\alpha\beta} = \sum_i v_{i\alpha} v_{i\beta} f^{(1)}_i \quad .$$

The combined form of the equations for the two time scales t_0 and t_1 in the incompressible limit ($Ma \to 0$ and $\Delta x \to 0$) finally reads

$$\nabla \cdot \vec{u} = 0, \quad \rho \partial_t \vec{u} + \rho \nabla \cdot (\vec{u}\vec{u}) = -\nabla p + 2\nu\rho \nabla \cdot \vec{S} \quad , \tag{2.41}$$

where $p = c_s^2 \rho$. The kinematic viscosity of the LB fluid is given by

$$\nu = c_s^2 (\tau - 1/2) \quad , \tag{2.42}$$

and the shear rate tensor $\vec{S}$ has the components

$$S_{\alpha\beta} = \frac{1}{2}(\partial_\alpha u_\beta + \partial_\beta u_\alpha) \quad . \tag{2.43}$$

This means that the LBM asymptotically solves the incompressible Navier-Stokes equations.

2.4.1 Shear stress in lattice Boltzmann method

If the fluid is incompressible, the shear stress tensor can be defined as [55],

$$\sigma_{\alpha\beta} = \eta(\partial_\alpha u_\beta + \partial_\beta u_\alpha) \quad , \tag{2.44}$$

where $\eta = \rho\nu$ is the dynamic viscosity. For Newtonian fluids, the shear rate tensor $\vec{S}$ and the shear stress tensor $\vec{\sigma}$ are related by $2\rho\nu\vec{S} = \vec{\sigma}$. Both tensors are symmetric and traceless.

From the Chapman-Enskog expansion, the pressure (with the equilibrium part) and the shear stress (with the non-equilibrium part) can be approximated by the second moments of the distribution functions,

$$\Pi^{(0)}_{\alpha\beta} = \sum_i v_{i\alpha} v_{i\beta} f^{(0)}_i = c_s^2 \rho \delta_{\alpha\beta} \quad , \tag{2.45}$$

$$\Pi^{(1)}_{\alpha\beta} = \sum_i v_{i\alpha} v_{i\beta} f_i^{(1)} = -\frac{\tau}{3}[\partial_\alpha(\rho u_\beta) + \partial_\beta(\rho u_\alpha) + \partial_{t_0}(\rho u_\alpha u_\beta)] \approx -\frac{\tau}{3\nu}\sigma_{\alpha\beta} \quad . \tag{2.46}$$

Sometimes the tracelessness of the shear stress tensor is enforced explicitly by writing [47]

$$\sigma_{\alpha\beta} = -\left(1 - \frac{1}{2\tau}\right) \sum_i \left(v_{i\alpha} v_{i\beta} - \frac{\delta_{\alpha\beta}}{D} \vec{v}_i \cdot \vec{v}_i\right) f_i^{neq} \quad , \tag{2.47}$$

where D is the number of spatial dimensions. Due to the approximation $f_i^{(1)} \rightarrow f_i^{neq}$ it is expected that the LBM result for the shear stress converges with a first order rate.

The shear rate tensor $\vec{S}$ (see Eq. 2.43) can be calculated from Eq. 2.47 ($2\rho\nu\vec{S} = \vec{\sigma}$),

$$S_{\alpha\beta} = -\frac{3}{2\tau} \sum_i \left(v_{i\alpha} v_{i\beta} - \frac{\delta_{\alpha\beta}}{k} \vec{v_i} \cdot \vec{v_i}\right) f_i^{(1)} \quad . \tag{2.48}$$

The shear rate is measured from the second invariant of the strain rate tensor $D_{II} = \sum_{\alpha\beta=1}^{k} S_{\alpha\beta} S_{\alpha\beta}$ as

$$\dot{\gamma} = 2\sqrt{D_{II}} \quad , \tag{2.49}$$

This local form to compute the shear stress and shear rate efficiently avoids calculation of derivatives over the velocity field.

2.5 Non-dimensionalization and choice of simulation parameters

Mapping the physical values of the macroscopic variables onto the lattice system and vice-versa, in order to interpret the simulation results is one of the most important causes of confusion among LBM beginners. Not only it is necessary a good knowledge of unit conversion; due to the inherent restrictions of the method, it is also crucial to balance the simulation parameters such that

accuracy, stability and efficiency can be achieved.

There is not a unique recipe to set in a proper manner the simulation parameters associated with the values in the physical system, but we can list some considerations to make it easier. Furthermore, we will enunciate the restrictions that one must consider to maintain the LB simulations into the stability and accuracy recommended ranges.

Most of the LB simulations use dimensionless macroscopic variables called *lattice variables*, such that the non-dimensionalization is achieved by dividing a dimensional quantity associated to a physical parameter by a chosen reference quantity of the same dimension. The result is known as the *lattice* value of the parameter or variable. For example, to make a conversion to the *lattice units* of any physical length l, we can use:

$$l_{lb} = \frac{l_p}{C_l} \quad . \tag{2.50}$$

The subscripts lb and p indicate whether the variable is in non-dimensional (LB units) or physical units, respectively. We have named C the conversion factor, where the subscript clarifies the physical property that is being converted. The basic or independent conversion factors most frequently used in the LBM are C_l, C_t (or C_u) and C_ρ because length, time (or velocity) and density are natural quantities in LB simulations. From these, it is possible to construct the conversion factors for the rest of the macroscopic variables [54]:

$$C_u = \frac{C_l}{C_t}, \qquad C_\nu = C_l C_u = \frac{C_l^2}{C_t}, \qquad C_P = \frac{C_\rho C_l^2}{C_t^2} \quad . \tag{2.51}$$

The components of the stress tensor $\vec{\sigma}$ have the same dimensions as pressure, and the conversion factor for the body force density acting over the fluid is

$$C_\sigma = \frac{C_\rho C_l^2}{C_t^2}, \quad C_F = \frac{C_\rho C_l}{C_t^2} \quad . \tag{2.52}$$

Additionally, the *law of similarity* plays a relevant role connecting both systems (lattice and physical). It can be summarized as follows: two incompressible flow systems are dynamically similar if they have the same Reynolds number and geometry [31]. This means that the Reynolds number must be identical in both

unit systems,

$$Re = \frac{l_{lb} u_{lb}}{\nu_{lb}} = \frac{l_p u_p}{\nu_p} \quad , \tag{2.53}$$

where l, u and ν are the characteristic length, velocity and kinematic viscosity of the system, respectively.

The first step to relate the physical parameters to their lattice counterparts is to set the independent lattice parameters to unity $\Delta x_{lb} = 1$, $\Delta t_{lb} = 1$ and $\rho_{lb} = 1$. This choice is arbitrary but highly recommended for most of the LB simulations, leading to the conversion factors for these parameters,

$$C_l = \Delta x, \quad C_t = \Delta t, \quad C_\rho = \rho \quad . \tag{2.54}$$

On the other hand, the direct connection between LB simulations and physical systems can be found through the Chapman-Enskog analysis. We know that the kinematic lattice viscosity ν_{lb} is related to the relaxation parameter τ (see Eq. 2.42),

$$\nu_{lb} = c_{slb}^2 \left(\tau - \frac{1}{2} \right) \quad , \tag{2.55}$$

$c_{slb} = 1/\sqrt{3}$ being the speed of sound in the lattice system. Using Eq. 2.51, it follows that the physical kinematic viscosity ν_p is related to the simulation parameters as follows,

$$\nu_p = c_{slb}^2 \left(\tau - \frac{1}{2} \right) \frac{\Delta x^2}{\Delta t} \quad . \tag{2.56}$$

This equation implies that the three basic simulation parameters τ, Δx and Δt are not independent, and only two of them can be chosen freely.

There is an infinite number of combinations to get the correct physical viscosity by balancing τ, Δx and Δt, but we have to consider the restrictions of the LBM, in such a way that conditions of simulation accuracy, stability and efficiency are fulfilled.

- The value of the relaxation parameter τ affects the accuracy. $\tau \gg 1$ should be avoided because the error of the BGK model grows with $(\tau - 1/2)^2$

[12]. It is generally recommended to choose relaxation times around unity [12, 55]. For large Reynolds numbers and small viscosities (or τ close to 0.5) this is not possible. This problem can be solved by using more advanced collision operators, like MRT among others.

- In order to operate in the quasi-incompressible limit, the Mach number must be small ($Ma_{lb} = u_{lb}/c_{slb} < 0.3$). To guarantee this condition, all simulated velocities have to be significantly smaller ($u_{lb} \ll c_{slb}$). This means that the value of u_{lb} should be less than 0.2. If the relaxation parameter approaches 0.5, the maximum velocity allowed should be lowered appropriately, to maintain the stability of the method.

- Increasing the lattice resolution only (decreasing Δx) does not necessarily reduce the error because the compressibility error will grow and eventually dominate. Reducing the time step only (decreasing Δt) does not decrease the spatial error. It is necessary to take into account certain relationships between Δx and Δt to control the error. The first attempt to solve this problem is to consider *diffusive scaling*: making $\Delta t \propto \Delta x^2$ guarantees that the leading order of the overall error scales like Δx^2, and in this way the LBM becomes second-order accurate in velocity, as we test in the results section.

In this way, it is possible to find the correct value of the lattice variables to run the simulations using the conversion factors to map the physical variables onto the lattice system and vice-versa.

2.6 Code implementation

For a better understanding of how LBM works, we will explain the computational procedure of the method. The LBM divides the simulation domain according to a 1D, 2D or 3D array, depending of the dimensions of the system. Each cell of the array, or node, stores the distribution functions f_i data associated with the velocity directions chosen in the lattice arrangement (the number of distribution functions is equal to the number of linkages of the model). These data are propagated toward the neighboring nodes at each time step, whereas the zero velocity distribution function is kept in the same node.

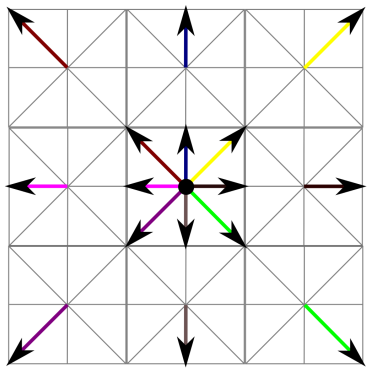

Figure 2.3: **Streaming step in a $D2Q9$ lattice arrangement.**

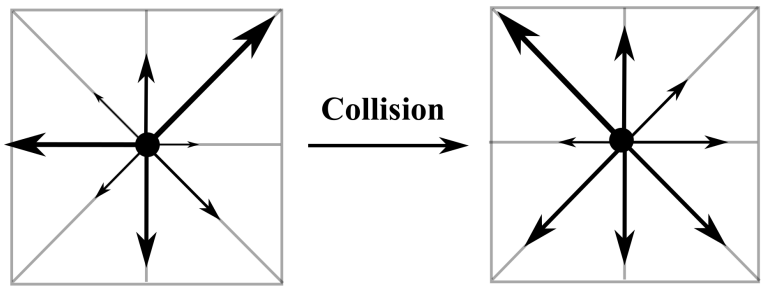

Figure 2.4: **Collision step in a $D2Q9$ lattice arrangement.**

The evolution equation of the LBM (see Eq. 2.25) can be divided into two fundamental parts.

$$f_i(\vec{x} + v_i\Delta t, \vec{t} + \Delta t) = \tilde{f}_i(\vec{x}, t) \tag{2.57}$$

$$\tilde{f}_i(\vec{x}, t) = f_i(\vec{x}, t) + \frac{1}{\tau}(f_i^{eq}(\rho, \vec{u}) - f_i(\vec{x}, t)) \tag{2.58}$$

In the streaming step, represented by Eq. 2.57, the distribution functions after the previous collision step $\tilde{f}_i$ are moved to the neighboring nodes, depending on

their direction as shown qualitatively in Fig. 2.3. In the collision step represented by Eq. 2.58, the distribution functions are relaxed (see Fig. 2.4) inside each node toward their equilibrium function f_i^{eq}, at a rate defined by the relaxation time τ.

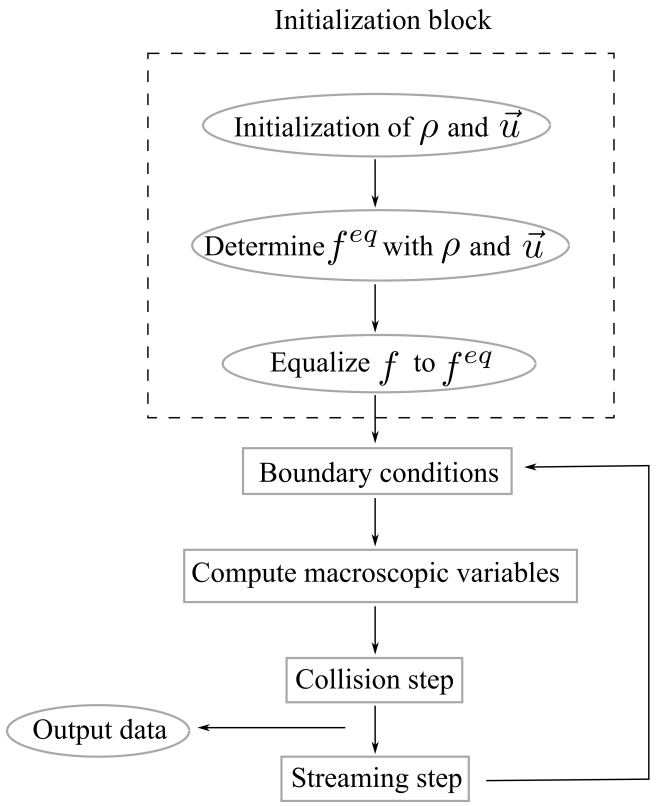

Figure 2.5: **Computational routine in the Lattice Boltzmann Method.**

These two steps are repeated in a loop until the system reaches a steady state or up to the desired time of evolution (in the case of a transient solution). At the start, it is first necessary to initialize the system - via the equilibrium function - calculating the initial distribution functions from the macroscopic variables defined by the initial conditions of the problem. The main loop then

starts computing the f_is at the boundary (see Sec. 3) and actualizing the macroscopic variables in whole system, with this new values. The collision step is performed to find the new f_is, which will propagate to the neighboring nodes in the next streaming step. Once this last step is finished, the method returns to the beginning of the loop. We can compute the macroscopic variables with the information of the f_is in each node, at each time step, through Eq. 2.18. A scheme of the computational procedure is shown in Fig 2.5.

2.7 LBM boundary conditions

The solutions of partial differential equations (PDE) like Navier-Stokes equations, can not be uniquely determined unless proper boundary and initial conditions are specified. Whatever method we may use to find a solution, these conditions must be appropriately supplied. The importance of boundary conditions should not be underestimated. Even though they apply to a small portion of the fluid domain, their influence may be felt everywhere in the flow solution. Therefore, boundary conditions should be treated with great care.

In the discrete space, a node has to be classified into one of these three categories: i) fluid nodes, where the LB equation 2.25 applies; ii) solid nodes, completely covered by the solid object where the LB equation should not be solved; iii) boundary nodes, that link fluid and solid nodes, and require special dynamic rules.

The fluid (solid) nodes can be identified as nodes connected exclusively to other fluid (solid) or boundary nodes, whilst the boundary nodes have at least one link to a solid and another to a fluid node. During the streaming step, the distribution functions belonging to fluid nodes will stream to neighboring nodes. The populations or distribution functions entering the fluid from boundary nodes are not determined by the LB equation (see the unknown populations with dashed lines f_3, f_5 and f_6 in Fig. 2.6), so it is necessary to find a set of rules to specify their values. Therefore, the role of LB boundary conditions is to calculate the right values for the incoming distribution functions.

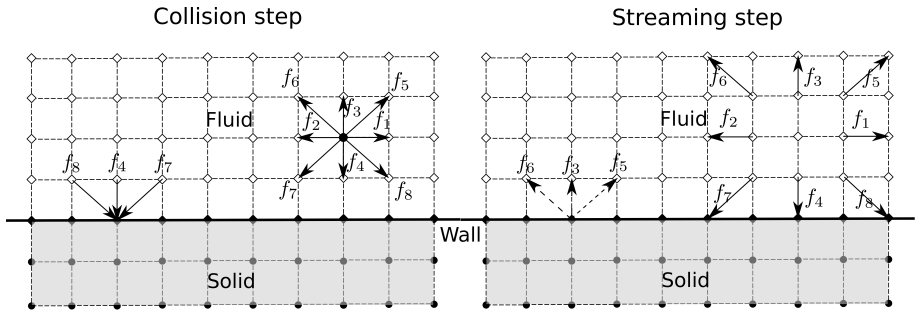

Figure 2.6: **The three types of LBM nodes at a boundary of the computational domain. At any boundary node, the post-collisional f_is are streamed from the neighboring fluid nodes, but not from the solid nodes, generating three unknowns (dashed arrows) in the D2Q9 arrangement.**

In the next sub-sections, we will explain the LB boundary conditions used in this work. This will complete the information on all the necessary elements of a LBM code (see Fig. 2.5) to simulate a flow problem with the LBM.

2.7.1 Periodic boundary conditions

Periodic boundary conditions are applied in flows with any type of symmetry, most of the cases related with cyclic flow systems. They state that the fluid leaving the domain on one side will enter at the opposite side.

During the streaming step, the unknown incoming populations after the collision step $\tilde{f}_i$ on one side are given by those leaving the domain at the opposite side:

$$\tilde{f}_i(\vec{x},t) = \tilde{f}_i(\vec{x}+\vec{L},t) \tag{2.59}$$

For $D2Q9$ arrangement, for example, the periodic flow condition along the x-axis becomes

$$\tilde{f}_i(\vec{x},t) = \tilde{f}_i(\vec{x}+\vec{L},t) \Longrightarrow \begin{cases} \tilde{f}_1(x_0,y,t) = \tilde{f}_1(x_N,y,t) \\ \tilde{f}_5(x_0,y,t) = \tilde{f}_5(x_N,y,t) \\ \tilde{f}_8(x_0,y,t) = \tilde{f}_8(x_N,y,t) \end{cases}, \tag{2.60}$$

$$\tilde{f}_{\bar{i}}(\vec{x},t) = \tilde{f}_{\bar{i}}(\vec{x}+\vec{L},t) \Longrightarrow \begin{cases} \tilde{f}_3(x_{N+1},y,t) = \tilde{f}_3(x_1,y,t) \\ \tilde{f}_6(x_{N+1},y,t) = \tilde{f}_6(x_1,y,t) \\ \tilde{f}_7(x_{N+1},y,t) = \tilde{f}_7(x_1,y,t) \end{cases}, \tag{2.61}$$

2.7.2 Solid boundaries

In hydrodynamics, the most common fluid-solid interface condition is the no-slip velocity boundary condition. Therefore, its correct implementation is crucial for modeling confined fluid flow phenomena and other problems involving solid boundaries.

The bounce-back rule implies that the particles at the boundary are reflected by the wall, preventing the flux of fluid across the boundary. Also, if the fluid does not slip on the wall i.e. there is not relative transverse velocity between fluid and boundary, the populations are specularly reflected in tangential and normal directions. The bounce-back method can be done in two different ways:

Full-way Bounce-back rule

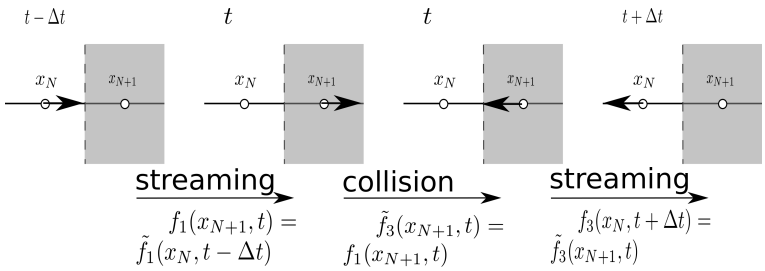

Figure 2.7: **Evolution in full-way bounce-back rule for populations at a boundary node.**

In this method [53], the particles travel from a boundary node to the neighboring solid node in one time step. Thus, the rule requires solid nodes where the populations are stored and inverted in the opposite velocity direction during the next collision step. Finally, they come back to the boundary node with an inverted direction (see Fig. 2.7). Therefore, the full-way bounce-back rule takes $2\Delta t$ to fully reflect the populations reaching the solid wall. It is often said that

the full-way bounce-back changes the collision step at solid nodes but leaves the usual streaming step unchanged.

Half-way Bounce-back rule

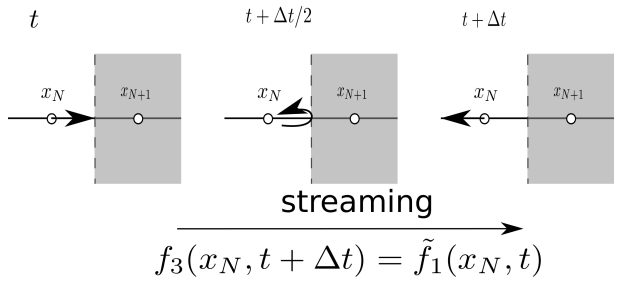

Figure 2.8: **Evolution in half-way bounce-back rule for populations at the boundary node.**

In the half-way bounce-back [30], the particles travel half of the distance between the boundary node and the solid node in half a time step, and come back to the boundary node with an opposite direction at the same streaming step (Fig. 2.8). In this way, solid nodes do not need to be implemented when half-way bounce-back boundary conditions are used. The half-way bounce-back rule effectively changes the streaming step, but does not modify the collision step.

To illustrate the half-way bounce-back rule, the streaming step for the populations leaving the boundary node $\vec{x}_b$ in the wall direction is replaced by

$$f_{\bar{i}} = (\vec{x}_b, t+\Delta t) = \tilde{f}_i(\vec{x}_b, t) \tag{2.62}$$

As an example, the half-way boundary conditions in the $D2Q9$ arrangement at the bottom wall (see Fig 2.9) can be expressed as :

$$\begin{aligned} f_3 &= (\vec{x}_b, t+\Delta t) = \tilde{f}_4(\vec{x}_b, t) \\ f_5 &= (\vec{x}_b, t+\Delta t) = \tilde{f}_7(\vec{x}_b, t) \\ f_6 &= (\vec{x}_b, t+\Delta t) = \tilde{f}_8(\vec{x}_b, t) \quad . \end{aligned} \tag{2.63}$$

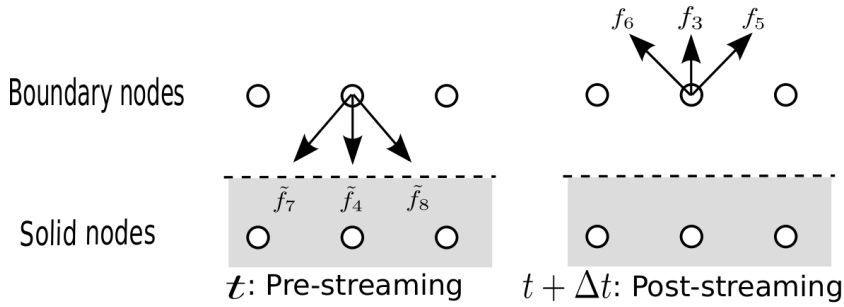

Figure 2.9: **Scheme of half-way bounce-back rule at a bottom wall.**

The idea is to calculate values for the unknown boundary populations at the boundary, such that the known and constructed populations reproduce the desired hydrodynamics. The main challenge is that typically there are more unknown boundary populations than macroscopic conditions. This explains why several techniques exist to deal with this problem. Two of the most popular approaches are: the equilibrium scheme [19, 39], and the non-equilibrium bounce-back method or better known as Zou-He method after its authors [60].

It is worth noting that the methods used to simulate a solid (resting or moving) wall in LBM, can be used to represent open boundaries, implementing a Dirichlet boundary condition for an imposed velocity or density (pressure) profile at the inlet or outlet of a fluid flow system. In the following subsection we explain how the approaches mentioned above apply to inlet/outlet boundaries.

2.7.3 Open boundaries

Open boundaries consist of inlets or outlets where the flow either enters or leaves the computational domain and where we should impose the boundary conditions given by the problem, for example, the value of the velocity or the density at the boundary (Dirichlet condition) or their derivatives (Neumann condition).

Equilibrium scheme

The equilibrium scheme enforces the post streaming populations at boundary nodes to acquire their equilibrium distribution value $f_i^{eq}(\rho_b, \vec{u}_b)$ for the desired macroscopic values to be obtained,

$$f_i(\vec{x}_b, t) = f_i^{eq}(\rho, \vec{u}) \quad . \tag{2.64}$$

The subscript b refers to the boundary node where inlet or outlet properties are imposed. Note that Eq. 2.64 applies to all populations f_i, instead of only unknown ones. The equilibrium scheme is second-order accurate only in the case where $\tau = \Delta t$ or $f^{(neq)} = 0$ [18]. Any other choice degrades its accuracy to first order. The easy implementation of the equilibrium scheme makes the extrapolation to 3D problems straightforward.

Zou-He boundary conditions

The equilibrium scheme fails to be an accurate boundary method since it neglects the non-equilibrium part $f_i^{(neq)}$ of the boundary populations f_i. As such, the next logical step of improvement is to include the non-equilibrium part. The new difficulty is how to find the non-equilibrium term for the boundary populations. As there is no unique answer to this question, several procedures have been proposed, resulting in a variety of techniques.
The reason for the higher accuracy of the Zou-He method comes from its ability to also capture the $f_i^{(2)}$ term, thus making it exact for parabolic solutions. This leads to an accuracy increase by one order, compared to standard second-order LB boundary schemes. The Zou-He method provides values for the unknown boundary populations by enforcing the bounce-back rule for their non-equilibrium part:

$$f_{\bar{i}}^{(neq)}(\vec{x}_b, t) = f_i^{(neq)}(\vec{x}_b, t) \qquad (\vec{v}_{\bar{i}} = -\vec{v}_i) \tag{2.65}$$

However, if we apply 2.65, there will be no way to guarantee that the tangential velocity attains the intended value. The condition for the tangential velocity at the boundary has not yet been linked with the prescription of the boundary populations. To establish this link, we can add an extra term to 2.65 that includes this information by modifying only the tangential component of the boundary populations. This term is called the transverse momentum correction

N_t [20]. Its sign is determined by t, a tangent unit vector along the wall,

$$f_{\bar{i}}^{(neq)}(\vec{x}_b, t) = f_i^{(neq)}(\vec{x}_b, t) - \frac{\vec{t} \cdot \vec{v}_i}{\|\vec{v}_i\|} N_t \qquad (\vec{v}_{\bar{i}} = -\vec{v}_i) \tag{2.66}$$

Unlike the equilibrium scheme previously described where the boundary scheme replaces all populations at the boundary, the Zou-He method modifies only the missing populations. This has both advantages and disadvantages. The Zou-

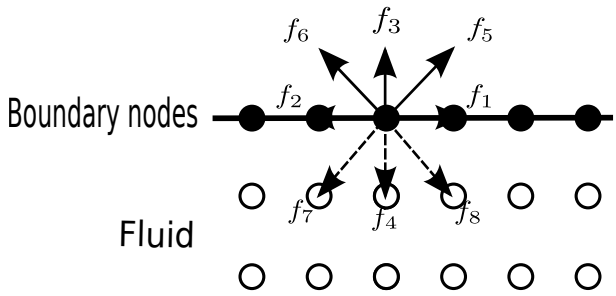

Figure 2.10: **Inlet boundary nodes. The known boundary populations are represented by continuous vectors and the unknown populations by dashed vectors.**

He method does not touch the known populations, i.e. it makes full use of all information already available. According to [25], this is believed to lead to improved accuracy. On the downside, it is difficult to generalize the scheme to arrangements with a large number of velocities. In fact, this boundary condition is cumbersome to employ in 3D [60].

Chapter 3

Finite differences for a mass transport model

The evolution of the concentration of a substance inside a fluid depends on the joint action of three processes: the advection (or transport by the existing streams in the medium), the diffusion or dispersion (which leads to a spreading of the substance of interest due to the concentration gradients) and the degradation processes (physical, chemical or biological) that act in the event that the substance is not conserved. Therefore, we are often interested in solving for the combined effect of all processes.

The combined effect of the three processes is reflected in the advection-diffusion equation, which tells us that the concentration C of the substance evolves as:

$$\frac{\partial C}{\partial t} = -\vec{u} \cdot \nabla C + \nabla \cdot D \nabla C + Q \quad , \tag{3.1}$$

where $\vec{u}$ is the fluid velocity that advects the substance and Q represents the possible sources or sinks of concentration due to chemical or biological reactions. The diffusion coefficient or diffusivity D is the quantity of a substance that, diffusing from one region to another, passes through each unit of cross section per unit of time when the volume-concentration gradient is the unity. The diffusivity depends of different factors such as flow velocity, bottom roughness, wind intensity or turbulence, and may have different values in each direction, so in a generalized manner it should be taken as a tensor. To simplify the model, the diffusivity is assumed as isotropic (it is assumed that it has a single value in all

directions) and it has the same scalar value in all directions.

Our goal is to approximate solutions to the differential Eq. 3.1, i.e., to find a function (or some discrete approximation to this function) which satisfies a given relationship between various of its derivatives on some given region of space and/or time, along with some boundary conditions along the edges of this domain. In general this is a difficult problem and only rarely can an analytic formula be found for the solution. A finite difference method proceeds by replacing the derivatives in the differential equations by finite difference (FD) approximations. This gives a large algebraic system of equations to be solved in place of the differential equation, something that is easily solved on a computer.

3.1 Lax-Wendroff method

The way to derive the Lax-Wendroff differential method is based on the idea to derive a scheme with second-order accuracy in space and time. First of all, we use Taylor series expansion in time, namely

$$C(\vec{x}_i, t_{n+1}) = C(\vec{x}_i, t_n) + \Delta t \partial_t C(\vec{x}_i, t_n) + \frac{\Delta t^2}{2} \partial_t^2 C(\vec{x}_i, t_n) + \mathcal{O}(\Delta t^2) \quad . \tag{3.2}$$

The Lax-Wendroff method uses spatial derivatives to replace higher-order temporal derivatives, obtained from the advection-diffusion equation itself 3.1. In our case, disregarding the chemical reaction term (the last term on the right hand side of the advection-diffusion equation) for simplicity, and introducing the discretization of the domain using a 3D mesh:

$$(x_i, y_j, z_k, t_n) = (i\Delta x, j\Delta y, k\Delta z, n\Delta t), \quad \forall i, j, k \in \mathbb{Z}, \quad \forall n \in \mathbb{N} \quad , \tag{3.3}$$

where Δx, Δy, Δz and Δt, denote the spatial steps in the three cartesian coordinates and the time step, respectively. We also denote by $C^n_{i,j,k}$ the approximation of $C(x_i, y_j, z_k, t_n)$. The second order Lax-Wendroff scheme based on 3.2 is given by

$$C^{n+1}_{i,j,k} = c^n_{i,j,k} + \Delta t \left(-u_x \frac{\partial C}{\partial x} - u_y \frac{\partial C}{\partial y} - u_z \frac{\partial C}{\partial z} \right) + \frac{(\Delta t)^2}{2}$$
$$\left(u_x^2 \frac{\partial^2 C}{\partial x^2} + u_y^2 \frac{\partial^2 C}{\partial y^2} + u_z^2 \frac{\partial^2 C}{\partial z^2} + 2u_x u_y \frac{\partial}{\partial x}\left(\frac{\partial C}{\partial y}\right) + 2u_x u_z \frac{\partial}{\partial x}\left(\frac{\partial C}{\partial z}\right) + 2u_y u_z \frac{\partial}{\partial y}\left(\frac{\partial C}{\partial z}\right) \right)$$
$$+ \Delta t D \left(\frac{\partial^2 C}{\partial x^2} + \frac{\partial^2 C}{\partial y^2} + \frac{\partial^2 C}{\partial z^2} \right) \quad .$$

(3.4)

By using central differences to obtain a second-order scheme, except for the cross terms where backward finite difference scheme has been used, the previous expression results in the following equation:

$$\begin{aligned} C^{n+1}_{i,j,k} &= C^n_{i,j,k} - \frac{V_x}{2}\left(C^n_{i+1,j,k} - C^n_{i-1,j,k}\right) - \frac{V_y}{2}\left(C^n_{i,j+1,k} - C^n_{i,j-1,k}\right) \\ &- \frac{V_z}{2}\left(C^n_{i,j,k+1} - C^n_{i,j,k-1}\right) + \frac{1}{2}\left(Z_x + V_x^2\right)\left(C^n_{i+1,j,k} - 2C^n_{i,j,k} + C^n_{i-1,j,k}\right) \\ &+ \frac{1}{2}\left(Z_y + V_y^2\right)\left(C^n_{i,j+1,k} - 2C^n_{i,j,k} + C^n_{i,j-1,k}\right) + \frac{1}{2}\left(Z_z + V_z^2\right)\left(C^n_{i,j,k+1} - 2C^n_{i,j,k} + C^n_{i,j,k-1}\right) \\ &+ V_x V_y\left(C^n_{i,j,k} + C^n_{i-1,j-1,k} - C^n_{i-1,j,k} - C^n_{i,j-1,k}\right) \\ &+ V_x V_z\left(C^n_{i,j,k} + C^n_{i-1,j,k-1} - C^n_{i-1,j,k} - C^n_{i,j,k-1}\right) \\ &+ V_y V_z\left(C^n_{i,j,k} + C^n_{i,j-1,k-1} - C^n_{i,j-1,k} - C^n_{i,j,k-1}\right) \quad , \end{aligned} \tag{3.5}$$

where the Courant-Friedrich-Levy numbers and the constants Z_x, Z_y, Z_z have been introduced,

$$\begin{aligned} V_x &= \frac{u_x \Delta t}{\Delta x}, \quad V_y = \frac{u_y \Delta t}{\Delta y}, \quad V_z = \frac{u_z \Delta t}{\Delta z} \\ Z_x &= \frac{2D\Delta t}{(\Delta x)^2}, \quad Z_y = \frac{2D\Delta t}{(\Delta y)^2}, \quad Z_z = \frac{2D\Delta t}{(\Delta z)^2} \quad . \end{aligned} \tag{3.6}$$

Equation 3.6 is only valid when the distance between nodes is the same in all directions. As we will explain in a later section, we used a non-uniform grid for the evolution of the concentration field seeking more stability and accuracy of the results. Considering the variability in the inter-node space (see figure 3.1),

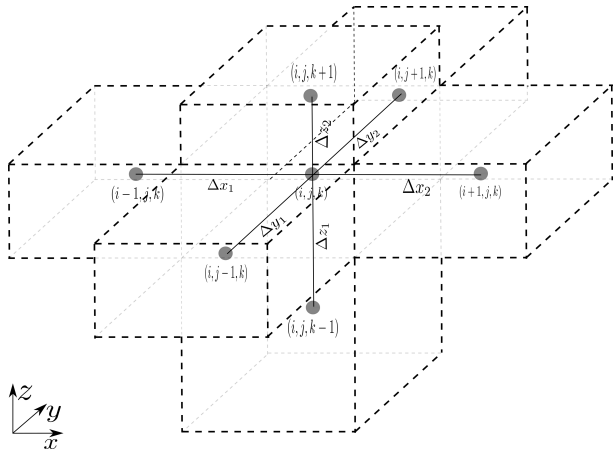

Figure 3.1: **Scheme of the stencil used in a 3D Lax-Wendroff method with a non-uniform grid.**

the second order lax Wendroff method in three dimensions is given by

$$
\begin{aligned}
C^{n+1}_{i,j,k} &= C^{n}_{i,j,k} - u_x\Delta t\left(\frac{C^{n}_{i+1,j,k}-C^{n}_{i-1,j,k}}{\Delta x_1+\Delta x_2}\right) - u_y\Delta t\left(\frac{C^{n}_{i,j+1,k}-C^{n}_{i,j-1,k}}{\Delta y_1+\Delta y_2}\right)\\
&- u_z\Delta t\left(\frac{C^{n}_{i,j,k+1}-C^{n}_{i,j,k-1}}{\Delta z_1+\Delta z_2}\right)\\
&+ \frac{1}{2}(2\Delta D+u_x^2(\Delta t)^2)\left[\left(\frac{2}{\Delta x_1+\Delta x_2}\right)\left(\frac{C^{n}_{i+1,j,k}-C^{n}_{i,j,k}}{\Delta x_2}-\frac{C^{n}_{i,j,k}-C^{n}_{i-1,j,k}}{\Delta x_1}\right)\right]\\
&+ \frac{1}{2}(2\Delta D+u_y^2(\Delta t)^2)\left[\left(\frac{2}{\Delta y_1+\Delta y_2}\right)\left(\frac{C^{n}_{i,j+1,k}-C^{n}_{i,j,k}}{\Delta y_2}-\frac{C^{n}_{i,j,k}-C^{n}_{i,j-1,k}}{\Delta y_1}\right)\right]\\
&+ \frac{1}{2}(2\Delta D+u_z^2(\Delta t)^2)\left[\left(\frac{2}{\Delta z_1+\Delta z_2}\right)\left(\frac{C^{n}_{i,j,k+1}-C^{n}_{i,j,k}}{\Delta z_2}-\frac{C^{n}_{i,j,k}-C^{n}_{i,j,k-1}}{\Delta z_1}\right)\right]\\
&+ \left(\frac{u_x\Delta t}{\Delta x_1}\right)\left(\frac{u_y\Delta t}{\Delta y_1}\right)\left(C^{n}_{i,j,k}+C^{n}_{i-1,j-1,k}-C^{n}_{i,j-1,k}-C^{n}_{i-1,j,k}\right)\\
&+ \left(\frac{u_x\Delta t}{\Delta x_1}\right)\left(\frac{u_z\Delta t}{\Delta z_1}\right)\left(C^{n}_{i,j,k}+C^{n}_{i-1,j,k-1}-C^{n}_{i,j,k-1}-C^{n}_{i-1,j,k}\right)\\
&+ \left(\frac{u_y\Delta t}{\Delta y_1}\right)\left(\frac{u_z\Delta t}{\Delta z_1}\right)\left(C^{n}_{i,j,k}+C^{n}_{i,j-1,k-1}-C^{n}_{i,j,k-1}-C^{n}_{i,j-1,k}\right)
\end{aligned}
$$

(3.7)

where Δx_1, Δx_2, Δy_1, Δy_2, Δz_1 and Δz_2 are the space steps in all directions as you can see in Fig. 3.1.

3.2 FD Boundary conditions

Solving a partial differential equation using a FD scheme may require to specify ghost points and associated ghost values for the dependent variable at these nodes. In a computational region (which may be 1, 2 or 3D) ghost nodes and their associated values occur at or adjacent to the boundaries of the region. Conditions leading to the prescription of ghost values are called boundary conditions, and are derived from the underlying physics of the situation. The correct treatment of boundary conditions is vital for accurate simulations. This is illustrated by considering the grid for a 2D region shown in Fig. 3.2. Grid nodes are indexed by $i = 1, 2, ..., N$ in the x direction and by $j = 1, 2, ..., M$ in the y direction. Indices 0, $N + 1$ and $M + 1$ indicate ghost nodes.

There are two basic ways to specify values of the dependent variable at ghost points. For clarity we will assume that the ghost node is at index $i = 0$ and hence $i = 1$ is the index of the grid point on the left boundary.
In Dirichlet boundary conditions, the value C_0^n of the concentration at the ghost point is specified. Some examples are:

- $C_0^n = constant$. e.g. $C_0^n = 0$ indicates that there is not concentration entering to the channel.
- $C_0^n = f(n)$, which is a time dependent boundary condition.
- $C_0^n = C_N^n$. This is a periodic boundary condition. This means that what passes out of the right boundary will pass in from the left boundary as though the two boundaries were joined together.

Derivative boundary conditions (Neumann conditions) specify the rate of change of the dependent variable at the grid nodes adjacent to the ghost point ($i = 1$ in our case). This can be done in two ways:

- Here the derivative of C in the x direction is specified at the boundary grid point $i = 1$. From this information C_0^n can be calculated. One way

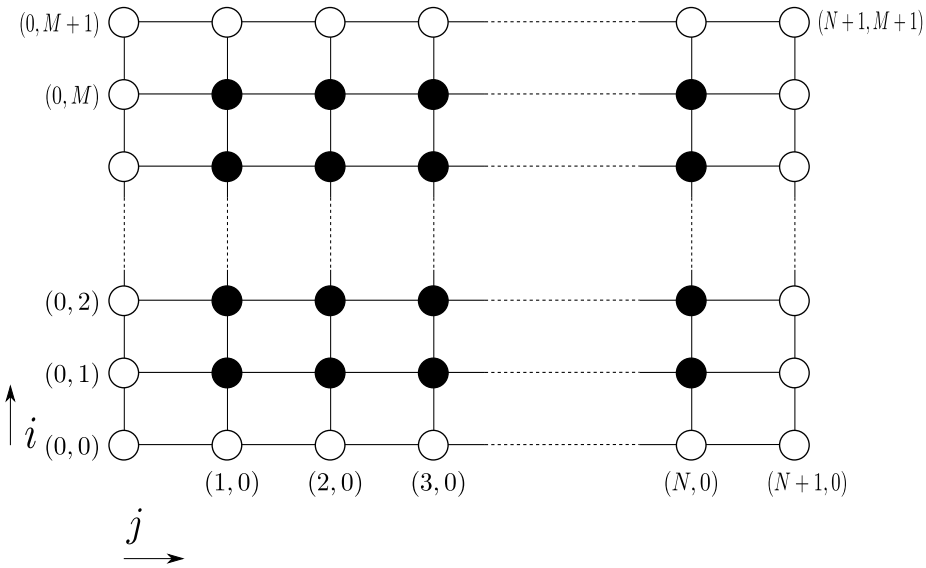

Figure 3.2: **Ghost (white) and grid (black) points for a 2D region.**

is to estimate $\partial C/\partial x$ at $i = 1$ by a central difference, giving

$$\frac{\partial C}{\partial x} = f(C) \approx \frac{C_2^n - C_0^n}{2\Delta x} \quad , \tag{3.8}$$

which arranges to give

$$C_0^n = C_2^n - 2\Delta x f(C) \quad . \tag{3.9}$$

- For the derivative of C in the normal direction, the outward pointing normal to the boundary is given at the grid point adjacent to the ghost point. Note that this direction is opposite to the x direction at the left hand boundary $i = 1$. An estimate of C_n at $i = 1$ by a central difference is

$$C_n \approx f(C) = \frac{C_0^n - C_2^n}{2\Delta x} \tag{3.10}$$

which arranges to give

$$C_0^n = C_2^n + 2\Delta x f(C) \quad . \tag{3.11}$$

In these derivative boundary condition examples, central differences were used but other estimates could have been easily used (e.g. first order backward difference for the leftmost ghost value).

Computational domains are finite, and it may happen that we need quantities simply leave a boundary that is not solid. This is often done by specifying a zero gradient normal at the boundary to the variable of interest. The global accuracy of a scheme is reduced if ghost values are calculated with less accuracy than the spatial accuracy of the scheme used for the regular nodes. I.e. a spatially third order scheme may drop to second order, if a central difference (second order) is used to calculate a ghost value.

Chapter 4

Generalized Newtonian fluids

A non-Newtonian fluid has a flow curve (shear stress vs shear rate) which is non-linear, or does not pass through the origin. Thus, an effective viscosity is generated being depending on flow conditions such as flow geometry, shear rate, and even on the kinematic history of the fluid at a given pressure and temperature. These fluids can be grouped in three classes:

- fluids for which the shear rate at each point of the system, and at a given time, is dependent only on the local shear stress at that time, such that there is an apparent viscosity determined locally by the value of the shear stress at that point. This kind of fluids is known as *Generalized Newtonian fluids*,
- complex fluids for which the relation between shear rate and shear stress also depends on the duration of the shearing and their kinematic history. These fluids are called *time-dependent fluids* and,
- fluids that show a mixed behavior between ideal fluids and elastic solids. These *visco-elastic fluids* have a partial elastic recovery after deformation.

Although, most fluids show a combined behavior of the three categories mentioned above, it is possible to find their most dominant non-Newtonian characteristics and thus be able to model each of the categories separately [6]. In this work, we will focus on the study of Generalized Newtonian fluids which in turn

can be divided into three subcategories (a scheme of the flow curves for these categories can be seen in Fig. 4.1):

- shear-thinning or pseudoplastic
- viscoplastic
- shear-thickening or dilatant

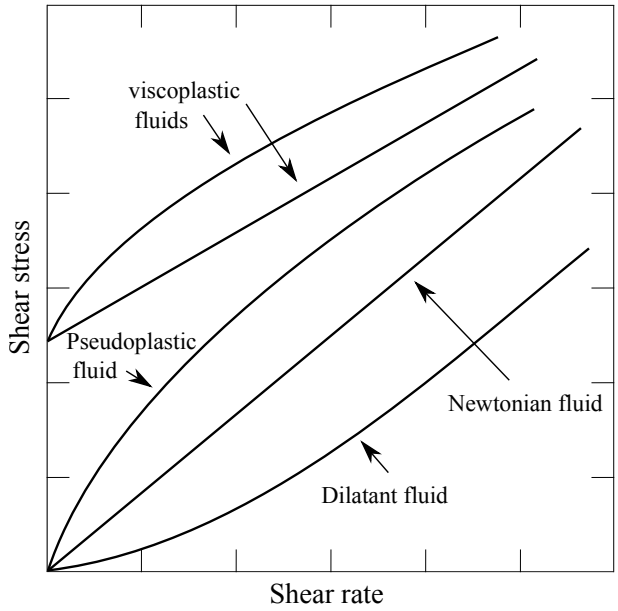

Figure 4.1: **Types of Generalized Newtonian flow behavior.**

The typical behavior of *shear-thinning fluids* shows a decreasing apparent viscosity when the shear rate is increasing. At very low, and very high shear rates, the apparent viscosity can be approximated to a constant value (Newtonian fluid). In the middle, the log-log graph is approximately linear, so the behavior can be described as a power-law (see Fig. 4.2). Many mathematical expressions of varying complexity and form have been proposed in the literature to model shear-thinnning properties. Some of the proposed models are based on physical theories (gas kinetic theory and statistical mechanics), but others are simple

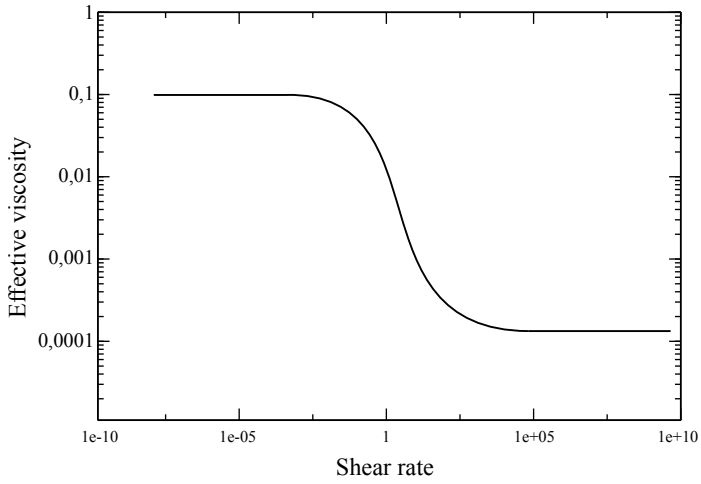

Figure 4.2: **Typical viscosity dependence on shear rate for *shear-thinning or pseudoplastic fluids.***

attempts at curve fitting, giving empirical relationships between the apparent viscosity and the shear stress (or shear rate).

The Cross model is valid throughout the complete range of shear rates and requires four parameters. The model may be expressed in the form

$$\frac{\mu - \mu_\infty}{\mu_0 - \mu_\infty} = \frac{1}{1 + K\dot{\gamma}^m} \quad , \tag{4.1}$$

where μ_0 and μ_∞ are the asymptotic values of viscosity at very low and very high shear rates, respectively, K is a constant parameter with the dimension of time and n is a dimensionless constant. The degree of shear-thinning is governed by the value of n.

A popular alternative to the Cross model, which also describes the whole flow

curve, is that due to Carreau

$$\frac{\mu-\mu_\infty}{\mu_0-\mu_\infty}=\frac{1}{(1+(K_1\dot{\gamma})^a 2)^{m_1/2}} \quad , \tag{4.2}$$

which also has a slightly more general form with five parameters known as the Carreau-Yasuda model

$$\frac{\mu-\mu_\infty}{\mu_0-\mu_\infty}=\frac{1}{(1+(K_1\dot{\gamma})^a)^{m_1/a}} \quad , \tag{4.3}$$

The Carreau and Cross models possess similar behavior at very low and very high shear rates and differ only in the shear thinning region, where $K_1\dot{\gamma}\sim 1$.

Many other models are valid over a restricted range of shear rate and may be derived from Cross or Carreau equations. If $\mu \ll \mu_0$, the Cross model reduces to the Sisko model

$$\frac{\mu_0}{\mu-\mu_\infty}=(K\dot{\gamma})^m \quad , \tag{4.4}$$

which may be expressed as

$$\mu=\mu_\infty+k\dot{\gamma}^{n-1} \quad , \tag{4.5}$$

where $k=\mu_0 K^{-m}$ and $n=1-m$. If $\mu \ll \mu_0$ and additionally $\mu \gg \mu_\infty$, the Cross equation reduces to the well known power-law model (also known as the Oswald-de Waele model),

$$\mu=k\dot{\gamma}^{n-1} \quad , \tag{4.6}$$

If $0 \leq n < 1$, the fluid is shear-thinning (pseudo-plastic). The smaller value of n, the greater the degree of shear-thinning; if $n=1$, the fluid is Newtonian with viscosity $\mu=k$; if $1<n$, the fluid is shear-thickening (dilatant).

In order to limit the wide range of viscosities that can occur when using the power law model, some numerical studies have used *ad hoc* schemes to limit the range to $\mu_0<\mu<\mu_\infty$, thus turning this model into an improved tool to reproduce the complete behavior of shear-thinning fluids in all the shear rate ranges. This gives the truncated power-law model, [43]

$$\mu=\begin{cases}\mu_0 & if\ \mu<\mu_0\\ k\dot{\gamma}^{n-1} & if\ \mu_0<\mu<\mu_\infty\\ \mu_\infty & if\ \mu>\mu_\infty\end{cases} \quad . \tag{4.7}$$

Viscoplastic fluids are characterized by the existence of a yield stress (τ_0) which must be exceeded before the fluid deforms or flows. Once the magnitude of the external stress is above the value of the yield stress, the flow curve can be linear or non-linear, but will not pass across the origin (see Fig 4.1).

One of the most used models are known as *Casson Model* to represent the flow of many biological materials like blood and others. This model has a yield stress τ_0 followed by a shear thinning region, and then a Newtonian plateau with viscosity μ_2 at high shear rates. The apparent viscosity can be described as

$$\mu = \begin{cases} \tau_0 \dot{\gamma}^{-1} + \mu_2 \dot{\gamma}^{-1/2} + \mu_2 & if \quad \tau > \tau_0 \\ \infty & if \ \tau \leq \tau_0 \end{cases} . \tag{4.8}$$

Finally, the shear-thickenning fluids are similar to pseudoplastic systems, because these show no yield stress but their apparent viscosity increases with increasing shear rate (see Fig 4.1). This type of fluid behavior was originally observed in concentrated suspensions.

Due to the shear-thinning behavior shown by the blood flow as will be explained below, various of these models have been used to study the possible influence of the blood flow properties as a cause for different cardiovascular diseases in human body.

4.1 Rheological models for blood flow

Advances in the field of haemorheology (science of the deformation and flow of materials applied to the study of flow properties of blood and its formed elements) have contributed to the fundamental understanding of the changes in the rheological properties of blood and its elements due to pathological disturbances, and are based on the evidence that they might be the primary cause of many cardiovascular diseases. Deviations in haemorheological parameters may affect tissue perfusion and be manifested as circulatory problems. Basically, pathologies with haematological origin like leukemia, and haemolytic anemia, among others, or pathologies associated with the risk factors of thrombosis and atherosclerosis are mainly related to disturbances of local homeostasis. Therefore, the mathematical and numerical study of powerful, yet simple, constitutive models that can capture the rheological response of blood over a range of flow

conditions is ultimately recognized as an important tool for clinical diagnosis and therapeutic planning [13, 33].

While plasma is nearly Newtonian in behavior, the whole blood exhibits marked non-Newtonian characteristics, particularly at low shear rates. The non-Newtonian behavior of blood is mainly explained by three phenomena: the erythrocytes tendency to form a micro-structure at low shear rates, their deformability and their tendency to align with the flow field at high shear rates [7]. Formation and breakup of this micro-structure, as well as the elongation and recovery of red blood cells, contribute to the blood's shear thinning, viscoelastic and thixotropic behavior. Aggregation and deformation of erythrocytes are complex dynamic processes in which cellular and plasma components of blood contribute as essential factors.

Experimental data under various flow conditions, particularly physiologically relevant flows, are required to develop meaningful models of these complex processes [52]. The common used value in the literature for blood density at 37°C is 1056 kg/m^3 [8]. The material parameters of blood are quite sensitive to the state of blood constituents as well as temperature, as can be appreciated in Table 4.1, where the dependence on haematocrit is included for the power-law model parameters obtained for human blood. The differences between the parameters for the same value of haematocrits is due to the difference in temperatures used in experiments [32, 57]. Table 4.2 summarizes some of the most common generalized Newtonian models that have been considered in the literature for the shear dependent viscosity of the whole human blood.

Ht (%)	n	k (Pa s^n)	Background
40.5	0.828	0.00927	From Kim et al. [51] for unadulterated human blood at 37°C using a rotating viscometer for $\dot{\gamma} \in [30, 375]\ s^{-1}$ and scanning capillary viscometer for $\dot{\gamma} \in [1, 375]\ s^{-1}$.
35	0.825	0.00888	From Walburn and Schneck [57] for anticoagulated blood at 37°C using a cone and plate viscometer for $\dot{\gamma} \in [23.28, 232.80]\ s^{-1}$.
40	0.800	0.0115	
45	0.775	0.0148	
45	0.61	0.042	From Liepsch and Moravec [32] for human blood at 23°C using a rotational rheometer for $\dot{\gamma} \in [0.2, 400]\ s^{-1}$.

Table 4.1: **Material constants for power-law model obtained by various researchers using fit of Eq. 4.6 to human blood data at different haematocrits.**

Model	$\frac{\mu(\dot{\gamma})-\mu_\infty}{\mu_0-\mu_\infty}$	Material constants for blood
Powell-Eyring	$\frac{\sinh^{-1}(\lambda\dot{\gamma})}{\lambda\dot{\gamma}}$	$\lambda = 5.383\ s$
Cross	$\frac{1}{1+(\lambda\dot{\gamma})^m}$	$\lambda = 1.007\ s, \quad m = 1.028$
Modified Cross	$\frac{1}{(1+(\lambda\dot{\gamma})^m)^a}$	$\lambda = 3.736\ s, \quad m = 2.406 \quad a = 0.254$
Carreau	$(1+(\lambda\dot{\gamma})^2)^{(n-1)/2}$	$\lambda = 3.313\ s, \quad n = 0.3568$
Carreau-Yasuda	$(1+(\lambda\dot{\gamma})^a)^{(n-1)/a}$	$\lambda = 1.902\ s, \quad m = 0.22 \quad a = 1.25$

Table 4.2: **Material constants for various generalized Newtonian models for blood with $\mu_0 = 0.056\ Pa\,s$, $\mu_\infty = 0.00345\ Pa\,s$.** (Taken from [28]).

Chapter 5

LBM for steady state power-law flow

In this section, numerical simulations performed with the LB code are presented to study the capability of the method to reproduce the main physical properties of truncated power-law non-Newtonian flows in a steady state. The simplicity and the wide range of experimental data found in the literature on the truncated power-law model make it a good benchmark to simulate biological flows. First, a steady state flow made by a driven-force is used to find the accuracy of the method and later, the flow is driven through a velocity inlet to compare the properties of the hydrodynamic fields for different degrees of shear-thinning behavior. At the same time, a description of blood flows passing through biological channels (like aorta, brachial, carotid and arterioles) is made to define the optimal conditions concerning the construction of the hybrid model.

5.1 2D truncated power-law non-Newtonian flow

For a given fluid with dynamic viscosity μ (in the case of Generalized Newtonian fluids $\mu(\dot{\gamma})$) and under the assumptions of laminar, incompressible, parallel, and steady viscous flow through a uniform channel, with constant cross-section shape, the stream-wise component of the momentum equation in cartesian coordinates ($u(x, y)$ in a two-dimensional system) reduces to the following Poisson

equation [2]:

$$\frac{1}{\rho}\frac{\partial P}{\partial x} = \nu \frac{\partial^2 u}{\partial y^2} \quad , \tag{5.1}$$

with driving pressure gradient $\partial P/\partial x$, and kinematic viscosity $\nu = \mu/\rho$. The transverse component of the momentum equation becomes

$$\frac{1}{\rho}\frac{\partial P}{\partial y} = 0 \quad . \tag{5.2}$$

Assuming the higher pressure region is on the left side of the channel, the gradient pressure $\partial P/\partial x$ would be negative if the direction of the fluid goes to the right side, meaning that the fluid is moving from the higher pressure region to the lower pressure one.

Applying a non-slip boundary condition $\vec{u} = 0$ on the channel walls (see Fig. 5.1), is possible to find an analytical solution for a power-law flow [49],

$$u(y) = \left(\frac{G}{2m}\right)^{\frac{1}{n}} \left(\frac{n}{n+1}\right) \left[\left(\frac{W}{2}\right)^{\frac{n+1}{n}} - \left(\left|\frac{W}{2} - y\right|\right)\right] \quad , \tag{5.3}$$

where W is the channel diameter and $G = -\frac{\partial P}{\partial x}$ is the pressure gradient driving the flow, and $m = k/\rho$. The Eq. 4.7 can be non-dimensionalized to produce a dimensionless number analogous to the Reynolds number

$$Re_{PL} = \frac{u_{max}^{(2-n)} W^n}{m} \quad . \tag{5.4}$$

5.1.1 Simulation setup

A driven-force flow is imposed using Eq. 2.29 as the evolution rule for the MRT-LBM. The length chosen in this simulation L_p was five times the width of the channel W_p (see Fig. 5.1). A non-slip full-way bounce-back boundary condition was imposed at the walls, and periodic boundaries were used at the inlet and outlet of the channel such that the fluid leaving the domain re-enters it at the other side, at each time step.

To compare the profiles of different degrees of non-Newtonian behavior, the velocity at the center of the channel in lattice units was chosen as $u_{max_{lb}} = 0.01$.

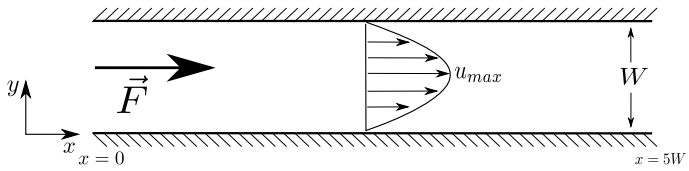

Figure 5.1: **Scheme of a two-dimensional channel with driven-force flow.**

As you can see in Eqs. 5.3 and 5.4, the kinematic viscosity and thus the relaxation parameter τ depend of the degree of shear-thinning of the fluid n. For values of n close to 0, the relaxation parameter will be close to 0.5, thereby, the maximum velocity chosen must be low enough to make sure that the simulation will have not stability issues.

In these simulations, the Reynolds number used was $Re = 100$ and the physical width of the channel was $W_p = 0.0254\ m$, being typical values found in the aorta artery. Simulations were carried out for different number of nodes $W_{lb} = 20, 50, 80, 100, 125, 200$, thus the distance between nodes in the physical system can be calculated from $\Delta x = W_p/W_{lb}$. With the aim to determine the order of the error of the LBM, diffusive scaling was used to determine the value of the time step $\Delta t = \Delta x^2$ in each case. There are other relations to determine the appropriate time step to make the simulation most efficient, some of these will be explained in next sections. Using the recommended values for the independent lattice parameters $\Delta x_{lb} = \Delta t_{lb} = \rho_{lb} = 1$, it is easy to compute the conversion factors for the mapping between physical and lattice systems, by means of Eqs. 2.51 and 2.52.

Using Eq. 2.29, a driven-force is introduced in the MRT-LBM, generating an effective gradient-pressure on the fluid $F = G_{lb}$. The flow will reach a steady state if the constant body force is applied across the whole channel. The simulations were run until the following criterion was satisfied

$$\sum_{\vec{x}} \|\vec{u}(\vec{x}, t) - \vec{u}(\vec{x}, t-1)\| < \varepsilon \quad , \tag{5.5}$$

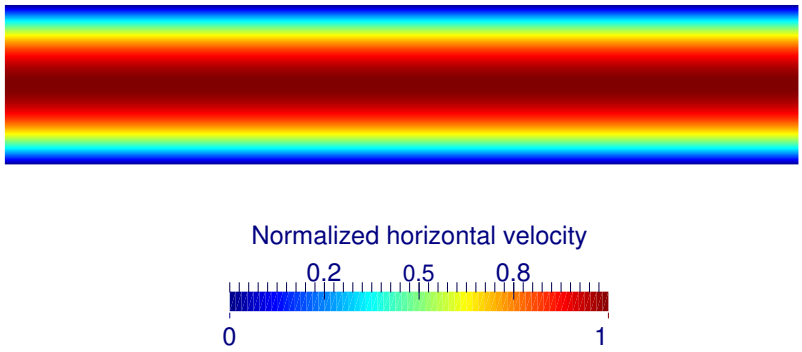

Figure 5.2: **Horizontal normalized velocity field in a force driven flow for the truncated power-law model with $n = 1$ (Newtonian Fluid).**

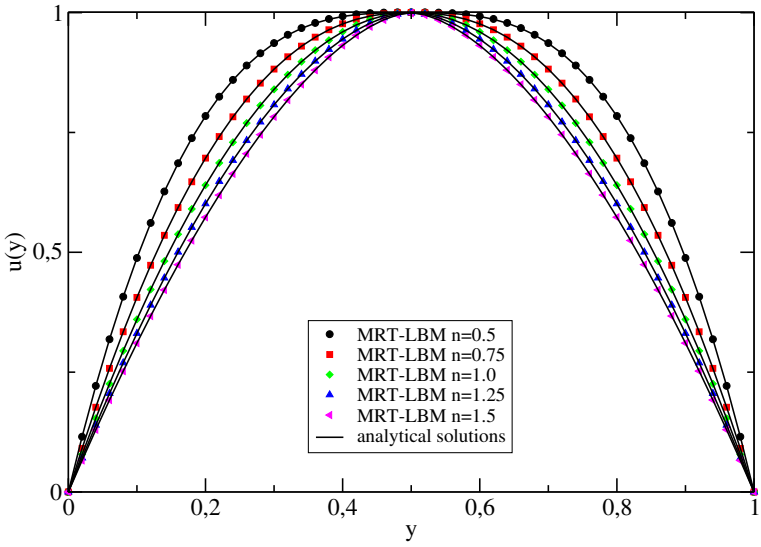

Figure 5.3: **Normalized velocity profiles for different degrees of Generalized Newtonian fluids in the Power-Law model.**

where ε was a small number taken as $\varepsilon = 1 \times 10^{-9}$. With this approach, the flow does not have a transient behavior before being totally developed, unlike the velocity-driven flow case, as shown below (see Fig. 5.2).

In Fig. 5.3, the analytical solution of the normalized velocity profile across the channel at $x = L/2$, for different values of n, is compared with the MRT-LBM results for $W_{lb} = 50$ in the steady state. The error in all cases was calculated as

$$\xi = \frac{\sum_{y=0}^{W_{lb}} \|\vec{u}_{lb}(y) - \vec{u}_a(y)\|}{\sum_{y=0}^{W_{lb}} \|\vec{u}_a(y)\|} \quad , \tag{5.6}$$

where the subscript a refers to the exact analytic solution and lb refers to the simulated value. The LB simulations show good accuracy when reproducing the velocity field of power-law flows; not only for shear-thinning, but also for Newtonian ($n = 1$) and shear-thickening fluids in the steady state.

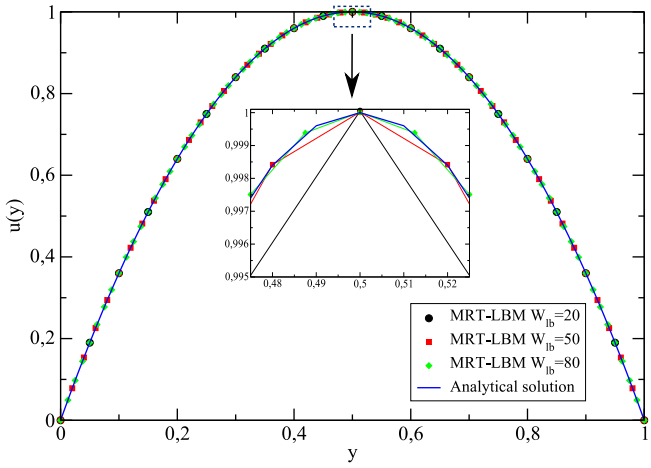

Figure 5.4: **Normalized velocity profiles with $n = 1.0$ (Newtonian fluid) for different resolutions.**

Additionally, we observe how the velocity profile approaches the analytical solution when the resolution of the mesh increases. In Fig. 5.4, the normalized velocity profiles at the middle of the channel $x = L/2$ for three different resolutions $W_{lb} = 20, 50, 80$ are shown. The periodic boundary conditions implemented at the inlet and outlet of the channel avoid the special treatment of corner nodes, producing high accuracy and stability of the method even when a coarse grid is used.

Results for the error calculated for $n = 1$ (Newtonian fluid), are shown in

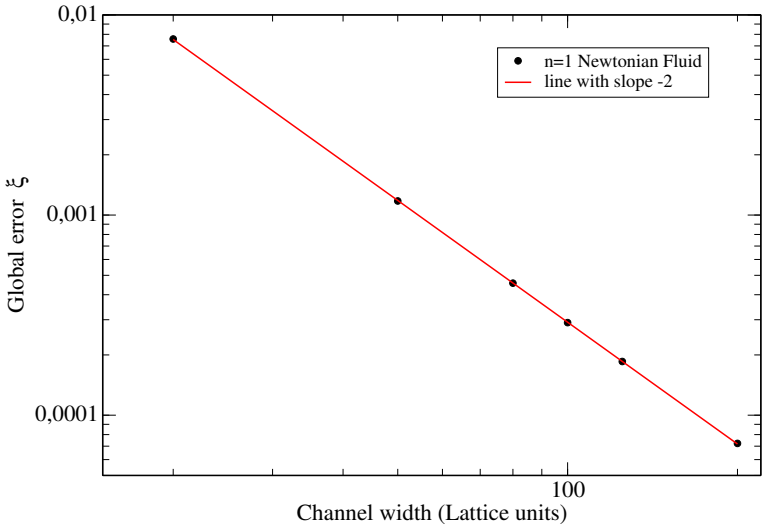

Figure 5.5: **Error for force-driven power-law model.**

Fig. 5.5. The red line represents the slope -2. The data closely match this trend line, indicating a second-order global error for our MRT-LBM, as we expected from the theory.

The shear rate across the channel reaches its minimum value at the center of the channel and the maximum near the walls, as we expected from the theory. In the case of $n = 1$ (Newtonian fluid) we can compare the result with the analytical solution. This is depicted in Fig. 5.6, where good agreement between both is observed. In shear-thinning fluids, the shear rate shows smaller gradients at the center of the channel and more pronounced gradients at the walls (concave form

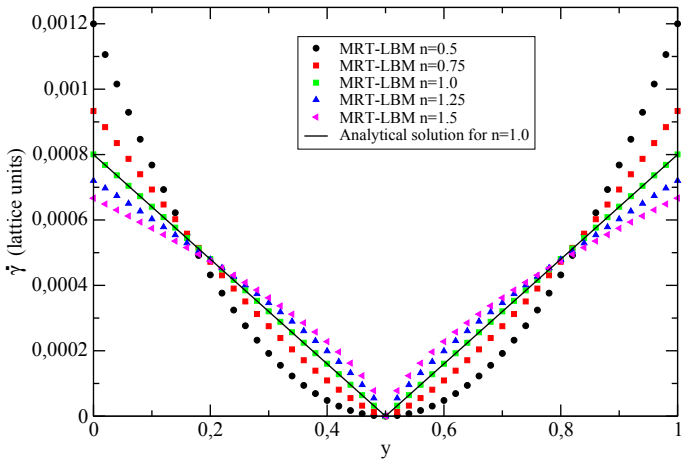

Figure 5.6: **Shear rate profiles for different degrees of Generalized Newtonian fluids in the Power-Law model.**

when $n < 1$). Conversely, shear-thickening fluids ($n > 1$) show larger gradients at the center of the channel but these decrease as we approach the walls (see Fig. 5.6).

The viscosity dependence of the shear rate can be seen in Fig. 5.7. The kinematic viscosity remains constant across the channel only for Newtonian fluids. In the other cases, the viscosity has a maximum (shear-thinning) or a minimum (shear-thickening) value at the center of the channel. These values are bounded by μ_0 and μ_∞, parameters defining the truncated power-law model (see Eq. 4.7).

This study of Power-Law non-Newtonian steady flows in the force-driven implementation of MRT-LBM shows the capability of the method to reproduce the hydrodynamic variables as velocity, shear rate, shear stress and kinematic viscosity for this kind of fluids. The main advantage of the force-driven implementation is generating a virtual gradient pressure without differences in the

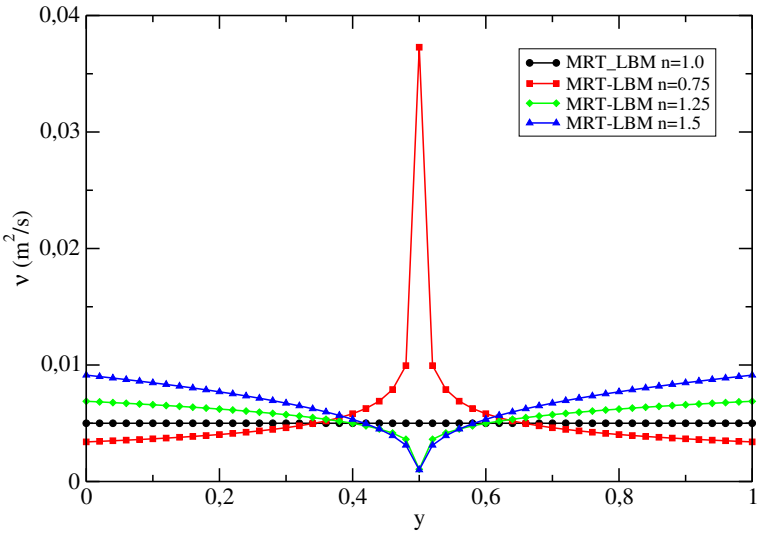

Figure 5.7: **Kinematic viscosity profiles for different degrees of Generalized Newtonian fluids in the Power-Law model.**

density (pressure) field, avoiding the stability issues inherent to the method. For the same reason, the length of the channel does not need to be controlled: in Fig. 5.2 the velocity profile is unchanged along the whole channel. At the same time, it is not possible to analyze the pressure field, that being a limiting factor.

As an alternative, we produced an effective pressure gradient over the fluid by imposing a constant velocity at the inlet of the channel ($u_{max_{lb}} = 0.01$ in these simulations). The length is ten times the width of the channel and a bounce-back half-way scheme is used to simulate the non-slip boundary condition at the walls. Zou-He boundary conditions were used to impose a constant velocity at the inlet but also to impose a constant density (pressure) at the outlet of the channel (see Sec. 2.7.3).

The parameters used in the simulations were the typical values found in the aorta artery as in the previous case, $W_p = 0.0254\ m$, $Re = 100$ and $W_{lb} = 50$. The positions along the channel selected as control points to analyze the veloc-

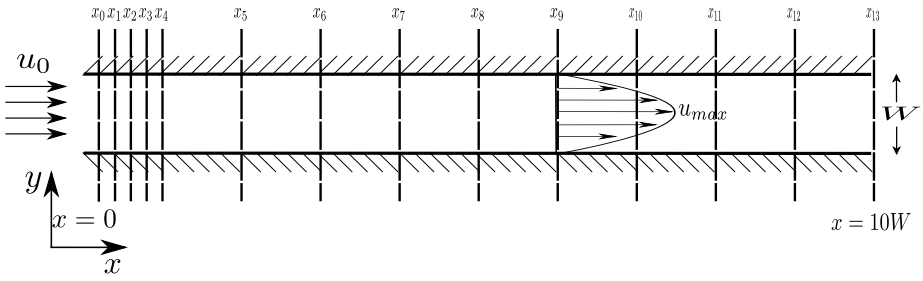

Figure 5.8: **Scheme of a two-dimensional channel with driven-velocity inlet flow, and positions along the channel where data were taken.**

ity profiles were $x = (0.2, 0.4, 0.6, 0.8, 1.0, 2.0, 3.0, 4.0, ..., 10.0)W$ as shown in the scheme of Fig. 5.8. The steady state flow for the power-law model (see Eq. 5.3) is compared bolow with the MRT-LBM results obtained with the velocity-driven implementation for different degrees n of shear-thinnning and shear-thickenning.

In Fig. 5.9, the velocity at the center of the channel shows different magni-

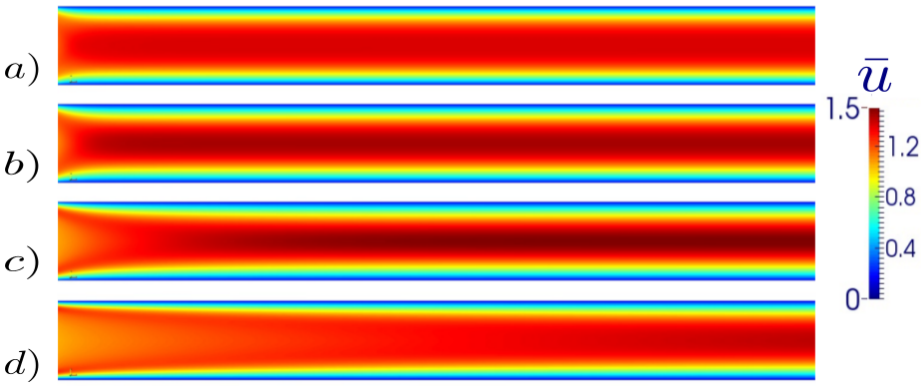

Figure 5.9: **Normalized velocity fields in a velocity-driven flow for different degrees n for the truncated power-law model. a)** $n = 0.5$**, b)** $n = 0.75$**, c)** $n = 1.0$**, d)** $n = 1.25$**.**

tudes for different values of n. A transition zone is found near the inlet before a

fully developed flow is obtained. Its length is different for each non-Newtonian fluid; its characteristic value needs to to be determined in order to compare the velocity profiles with the analytical solution properly.

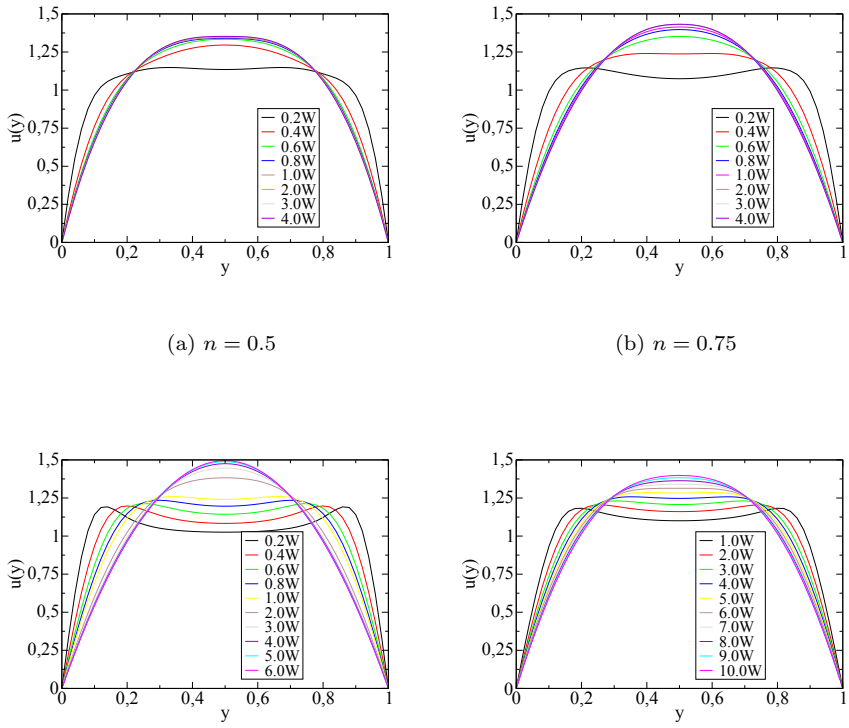

(a) $n = 0.5$ (b) $n = 0.75$

(c) $n = 1.0$ (d) $n = 1.25$

Figure 5.10: **Velocity profiles for different values of n. The profiles are measured at several positions along the channel (see Fig 5.8).**

In Fig 5.10, the velocity profiles across the channel at different distances from the inlet (see Fig. 5.8) are shown once they reach a steady state for n =

$0.5, 0.75, 1.0, 1.25$ respectively. The length of the transition zone is not a constant for Non-Newtonian fluids. Flows with high shear-thinning behavior $n \to 0$ have a faster convergence, producing small transition zones. Taking measurements in the middle of the channel $x = 5W$ ensures fully developed flow for Newtonian fluids, $n = 1$. For $n = 1.25$ (see Fig. 5.10(d)), data taken at the outlet of the channel $x = 10W$ show that the transition zone covers the whole computational domain. We recommend making a specific study for the modeling of shear-thickening with an inlet velocity.

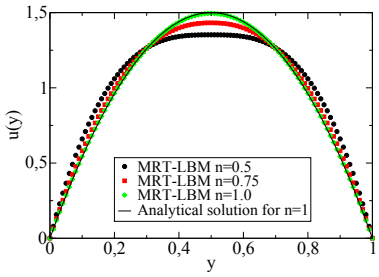

(a) Normalized velocity profiles for different values of n in a velocity-driven flow.

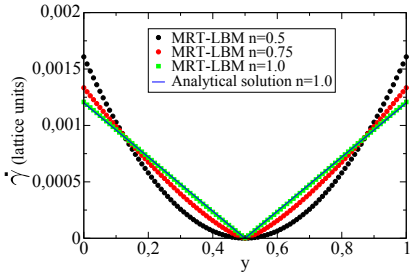

(b) Shear rate profiles for different values of n in a velocity-driven flow.

Figure 5.11: **Normalized velocity and shear rate profiles in a velocity-driven power-law flow.**

To guarantee reliable results, data are taken at $x = 5W$ for shear-thinning and Newtonian flows. In Fig. 5.11 the velocity and the shear rate are shown for different values of n. The velocity at the center of the channel for $n = 1$ is $u_{max} = 3/2\, u_0$ as we expected, and a good agreement with the analytical solution was attained for both velocity and shear rate profiles. For $n < 1$, the maximum velocity decreased as n decreased. The flat shape found in shear-thinning velocity profiles is well reproduced by the method as in the force-driven case.

5.2 3D Truncated Power-Law non-Newtonian flow

With the objectives of this work in mind (mass transfer in 2D and 3D micro-device), we need to guarantee that our code is capable to reproduce the main characteristics of the three-dimensional non-Newtonian flows. The $D3Q19$ LB arrangement (see Fig. 2.2) was implemented to reproduce the velocity profiles for different fluid behaviors (dilatant, Newtonian and pseudo-plastic). The 3D flow of non-Newtonian fluids following the truncated power-law model was simulated (using force-driven flow) in two different geometries: a 3D tube and a rectangular channel.

First, we consider a 3D tube along the x-direction. The velocity fields for different values of n are shown in Fig. 5.13. For a truncated power-law fluid, the steady state velocity profile in a 3D tube has an analytical solution given by [3]

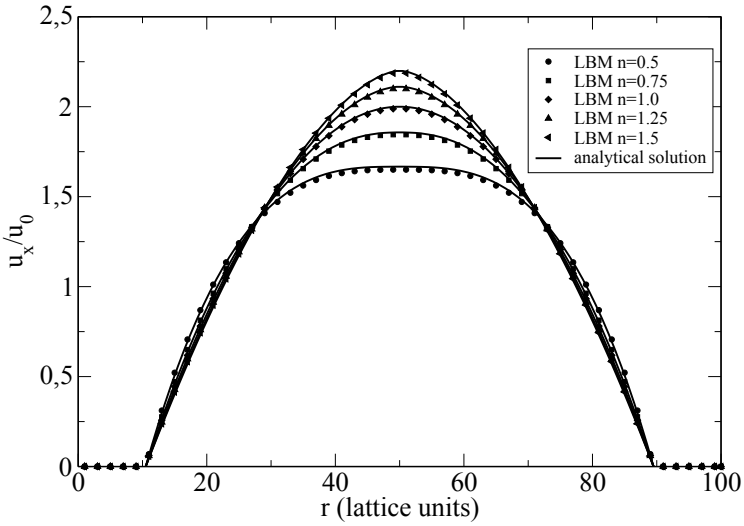

Figure 5.12: **Normalized velocity profiles for truncated power-law flow in a 3D tube, for different values of n.**

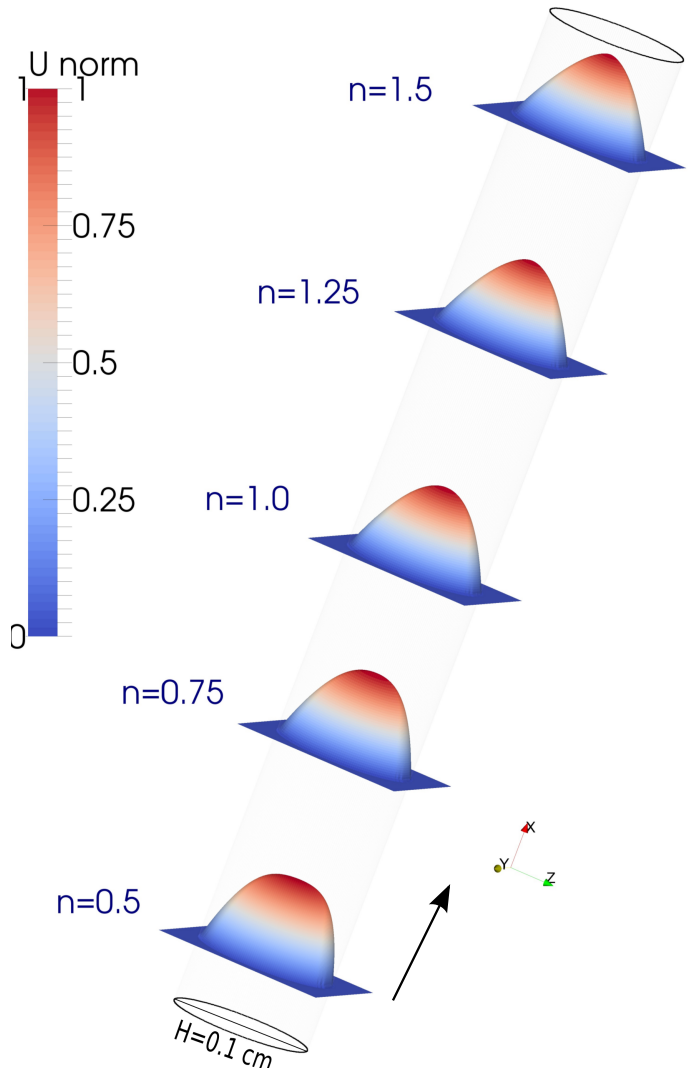

Figure 5.13: **Normalized velocity field for truncated power-law flow in a 3D tube, for different values of n.**

$$\frac{u_x(r)}{u_0} = \frac{3n+1}{n+1}\left[1 - \left(\frac{r}{R}\right)^{1+1/n}\right] \quad , \tag{5.7}$$

as a function of the radial coordinate r, where $R = 0.1\ m$ is the radius of the tube and u_0 is the mean velocity. The lattice spacing used in the simulations was $0.001\ m$ and the flow was driven by an x-direction constant body force of $F = 0.01\ m/s^2$. Periodic boundaries were used on the inlet and the outlet and a bounce-back boundary condition was applied on the channel walls. A range $0.5 < n < 1.5$ for the power-law degree was analyzed to validate both pseudoplastic and dilatant flows in $3D$. Fig 5.12 shows good agreement between the simulated profiles with respect to their respective analytical solutions given by Eq. (5.7). The shear-thickening cases result in a triangular flow profile across the tube, whereas the shear-thinning cases result in a flat plug-flow profile. The errors are shown in Table 5.1.

	$n = 0.5$	$n = 0.75$	$n = 1.0$	$n = 1.25$	$n = 1.5$
L2 error	0.0093	0.0070	0.0062	0.0059	0.0056

Table 5.1: **L2 error of the simulated velocity profiles in a 3D tube for different values of the non-Newtonian power-law exponent n.**

As a second example, we consider a three-dimensional non-Newtonian power-law flow in a rectangular channel along the x-axis, of width W in the y-direction, and height H in the z-direction. The analytical solution of the velocity profiles is known only for Newtonian fluids ($n = 1$), and is given by [55]

$$u_x(y,z) = \frac{u_{max}}{A}\left[z(H-z) - \frac{8H^2}{\pi^3}\sum_{m}^{odd}\frac{1}{m^3}\frac{\cosh[m\pi(y-W/2)/H]}{\cosh(m\pi W/2H)}\sin\left(\frac{m\pi z}{H}\right)\right] \quad , \tag{5.8}$$

where the origin of the coordinate system is in one of the corners of the channel. The pressure gradient has been replaced as a variable in favor of the maximum velocity developed in the center of the channel $\partial P/\partial x = -2\eta u_{max}/\Sigma$, where A

is a normalization factor depending on the geometry,

$$A = \frac{H^2}{4} - \frac{8H^2}{\pi^3} \sum_{m}^{odd} \frac{1}{m^3} \frac{\sin(m\pi/2)}{\cosh(m\pi W/2H)} \quad . \tag{5.9}$$

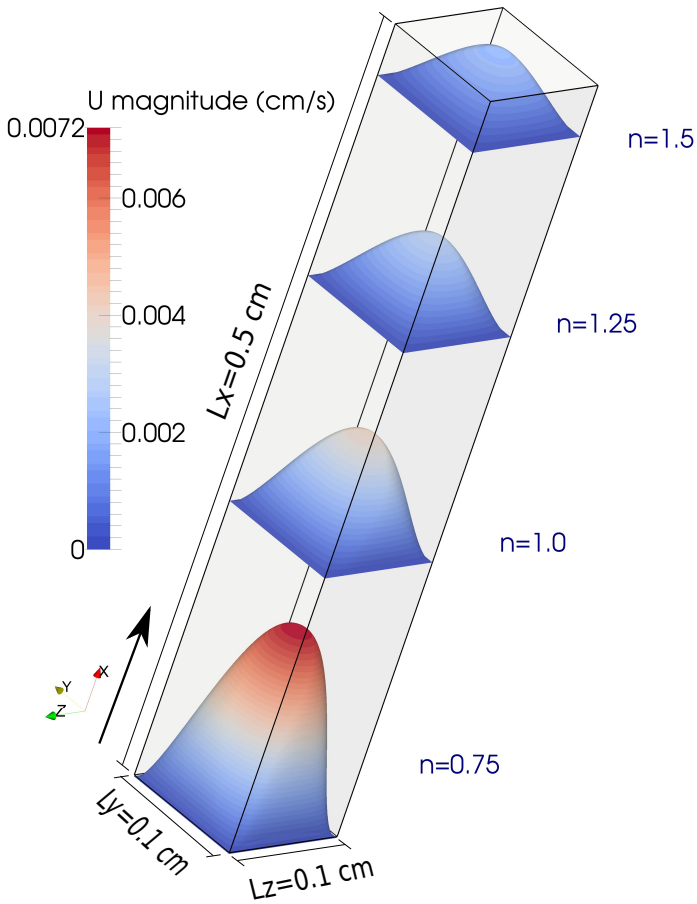

Figure 5.14: **Velocity field for truncated power-law flow in a 3D rectangular channel, for different values of n.**

For 3D rectangular channel, both width W and height H were set to 0.1 m, the reference value of the kinematic viscosity ν_p was 0.0025 m/s^2 and the Reynolds number, $Re = Hu_{max}/\nu_p$ was 10. The value of the driving force was calculated with Eq. (5.9), and the boundary conditions were the same as in the former example. In Fig. 5.15 the velocity profiles for different values of n are shown. When the fluid is Newtonian ($n = 1$) the comparison with the analytical expression 5.8 gives less than 1% of error, showing the accuracy of the method. In all the other cases (non-Newtonian fluids) for which the analytical velocity profiles are not known, there is a qualitative agreement with the characteristics of shear-thinning and shear-thickening flows.

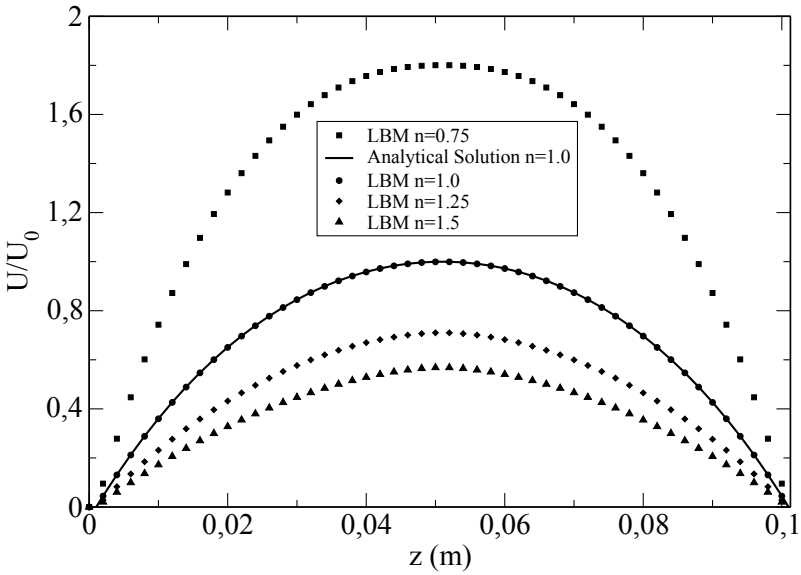

Figure 5.15: **Normalized velocity field for truncated power-law flow in a 3D rectangular channel, for different values of n.**

Chapter 6

LBM for pulsatile power-law model flow

Womersley or pulsatile flow denotes a Poiseuille-like flow (channel width W, viscosity ν) with an oscillating pressure drop along the length L of the channel: $\Delta p(t) = \Delta p_0 \cos(\omega t)$ with angular frequency $\omega = 2\pi/T$, period of oscillation T and amplitude of the pressure gradient Δp. The Reynolds number for an oscillatory flow is usually defined through the velocity one would observe for $\omega = 0$: $Re = u_0 W/\nu$. The amplitude of the velocity u_0 is related to Δp_0 according to

$$u_0 = \frac{\Delta p w^2}{8 L \rho \nu} \tag{6.1}$$

for a 2D channel. Due to the frequency ω, which is obviously zero for simple Poiseuille flow, an additional dimensionless number is required to characterize the flow. There are different ways to construct such a number: we just have to write down a dimensionless combination containing ω and other suitable parameters. The Womersley number is defined as

$$\alpha = \sqrt{\frac{\omega}{\nu}} W \quad . \tag{6.2}$$

Unlike shear-thinning flows modeled with a truncated power-law, which do not have an exact solution, the velocity field for the Womersley flow of Newtonian

fluids ($n = 1$) is given by [23]

$$u(y) = \Re\left[\left(\frac{-G}{\rho\omega}\right) e^{(i\omega t)} \left(\frac{1 - \cosh(\sqrt{b}(y - L/2))}{\cosh(\sqrt{b}L/2)}\right)\right] \quad . \tag{6.3}$$

Applying $\sigma_{\alpha\beta} = \eta(\partial_\alpha u_\beta + \partial_\beta u_\alpha)$ (see Eq. 2.44), it is possible to find a theoretical expression for the stress tensor in this type of flow. This pulsatile flow behavior is an approximation to the rhythms or the changes in the gradient pressure produced by the heart over our whole blood system.

6.1 Simulation setup

Let us consider a micro-flow with Reynolds number $Re = 0.01$ and channel width $W_p = 0.00004$ m which are typical values for blood flow in arterioles. The stability of the simulations will depend on the period of the oscillation, T. To produce an stable oscillating gradient pressure, the pressure steps at the boundary or the changes in the inlet-velocity boundary at each time step should be as small as possible, but should also maintain the computational costs under reasonable terms.

A lower bound for the oscillation time to ensure that all the time scales are resolved in a proper way, can be calculated from $T >> ts_{lb} \sim L_{lb}/c_{slb}$, where ts_{lb} is the characteristic acoustic time scale and c_{slb} the speed of sound. L_{lb} is the length of the channel, in our case $L_{lb} = 250$ and $L_{lb} = 5W_{lb}$. Choosing $T = 10ts_{lb}$, the different scales will be well-resolved. However, this may not be enough to generate a suitable time-dependent boundary condition at the inlet of the channel.

As a first step to avoid the possible stability problems associated with the time-dependent boundary condition, a virtual pressure gradient has been applied to the fluid as an external force in the lattice Boltzmann equation 2.29. The parameters and conversion factors are found using the information in Sec. 2.5. In our simulations, $ts_{lb} \simeq 433$ time steps, thus a reasonable choice for the period may be $T >= 10ts_{lb} = 10000$ time steps. With the oscillation period, it is easy now to find the oscillation frequency and the kinematic viscosity ν_{lb}, using the Womersley number in Eq. 6.2. The pressure difference can be calculated from Eq. 6.1.

Different Womersley $\alpha = 3, 5, 7, ..., 15$ and Reynolds numbers $Re = 0.01$, 0.03, 0.07, 0.1,..., 1.0 were considered. For the fluid, we used the parameters for the power-law model found by Kim et al. [51] and shown in Tab.4.1. The non-Newtonian behavior was compared to that of Newtonian flow ($n = 1$). All simulations were run until the following criterion was satisfied:

$$\sum_{\vec{x}} \|\vec{u}(\vec{x}, \kappa T) - \vec{u}(\vec{x}, (\kappa - 1)T)\| < \varepsilon \quad , \tag{6.4}$$

with $\kappa \in \mathbb{N}$ being the number of periods simulated, and the tolerance $\varepsilon = 1 \times 10^{-7}$. Once the above criterion was reached, the simulation was run for one additional period, and data recorded at ten equally spaced times.

Normalized velocity profiles across the channel width for different Womersley numbers for Newtonian fluids $n = 1$ are shown in Fig. 6.1. These profiles were compared with the corresponding analytical solutions given by Eq. 6.3, and a good agreement was found. For small Womersley numbers, the oscillating velocity profiles have a parabolic form, with the maximum value found at the center of the channel (Fig. 6.1). For higher Womersley numbers, the profile has a flat shape, and by $\alpha \geq 7$ two maxima are already visible. As α is further increased, the two velocity peaks approach the channel walls Fig. 6.1. Also, as the Womersley number increases the amplitude of the oscillating velocity decreases.

In Fig. 6.2, normalized velocity profiles for the power-law model with material constants obtained by Kim et al. [51] ($n = 0.828$ and $k = 0.00927$ Pa·s^n) are shown for different values of α. The peak values of the velocity are smaller than in the case of Newtonian flow. As before, the velocities decrease with increasing α, but now at a much smaller pace: a difference of one order of magnitude is observed at $\alpha = 3$, while for $\alpha = 15$ the velocities of the Newtonian and non-Newtonian cases have almost similar values. The flat shape shown by Newtonian velocity profiles at $\alpha \geq 9$ is almost lost for this particular shear-thinning degree $n = 0.828$. There is a preference by power-law flows to maintain the parabolic shape for the entire range of α studied.

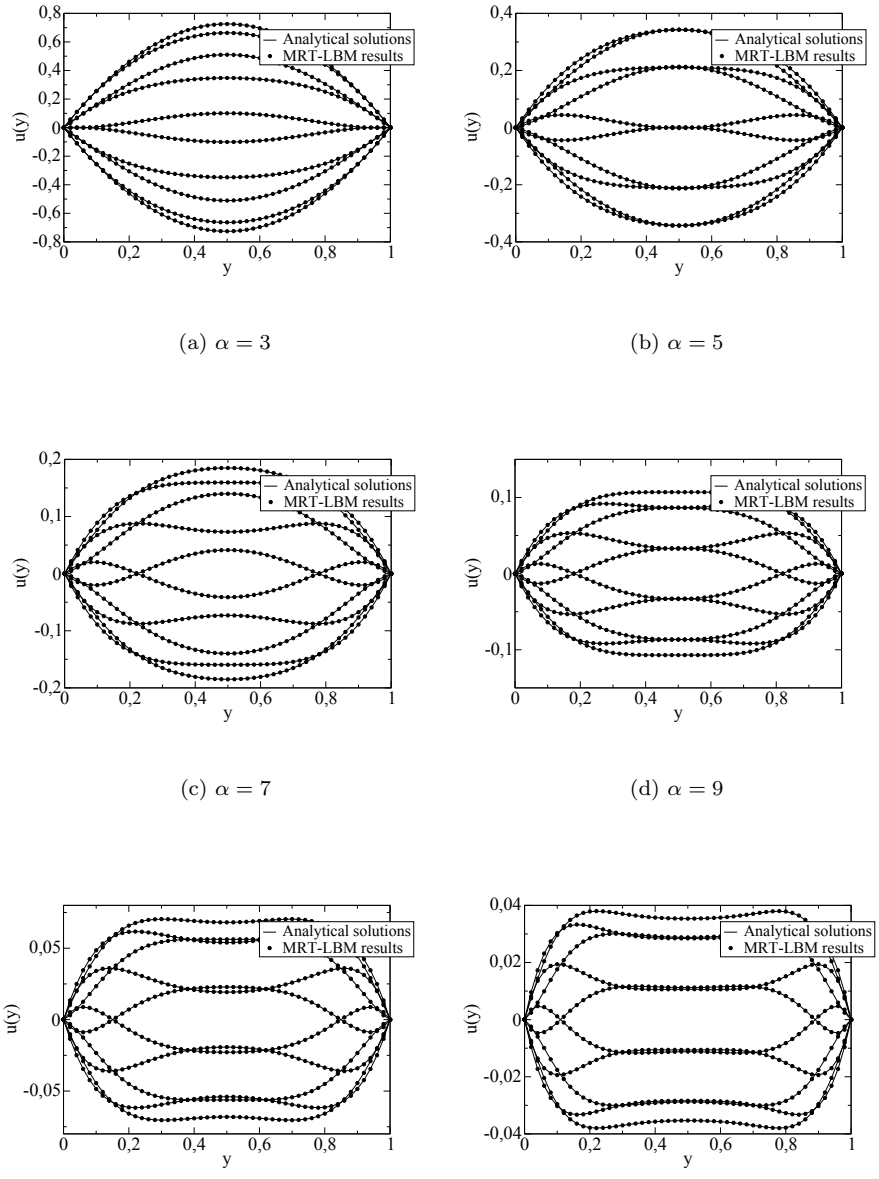

(a) $\alpha = 3$ (b) $\alpha = 5$

(c) $\alpha = 7$ (d) $\alpha = 9$

(e) $\alpha = 11$ (f) $\alpha = 15$

Figure 6.1: **Normalized velocity profiles in a complete period T in a Womersley flow ($n = 1$) for different values of the Womersley number α.**

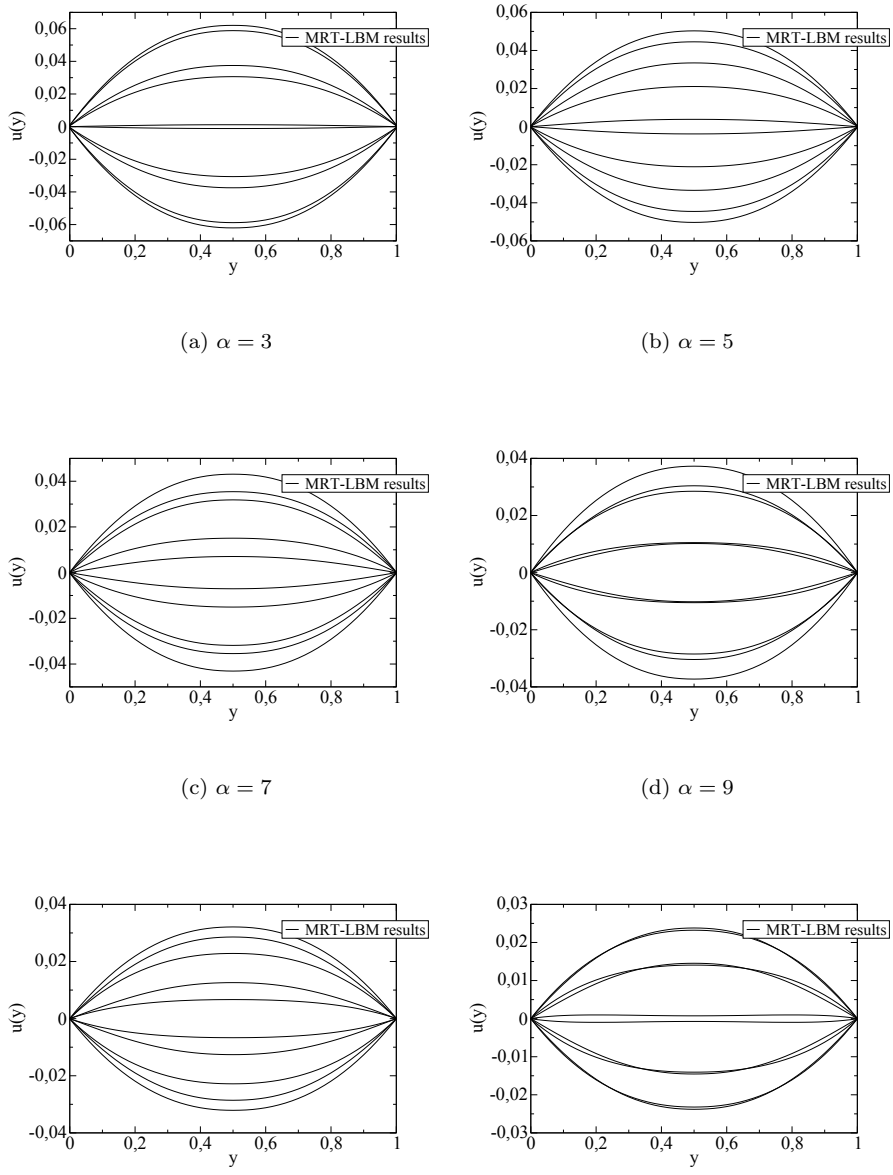

(a) $\alpha = 3$ (b) $\alpha = 5$

(c) $\alpha = 7$ (d) $\alpha = 9$

(e) $\alpha = 11$ (f) $\alpha = 15$

Figure 6.2: **Normalized velocity profiles in a complete period T in a pulsatile flow ($n = 0.828$) for different values of α.**

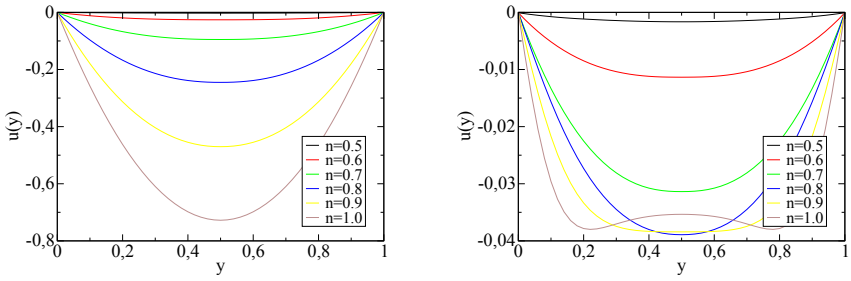

(a) $\alpha = 3$ (b) $\alpha = 15$

Figure 6.3: **Normalized velocity profiles at $t = 0.5T$ in a pulsatile flow for different values of n.**

A parametric study for different degrees n was made to visualize this behavior. In fig. 6.3 the velocity profiles for different shear-thinning degrees n are displayed at exactly the same times for a) $\alpha = 3$ and b) $\alpha = 15$. As one can see in Fig. 6.3(b), the inflection point is near $n = 0.9$. For $n < 0.9$ the two peaks vanish and the profile has a parabolic shape.

The MRT-LBM is also capable to properly reproduce the shear stress components and the shear rate by performing only local calculations, unlike conventional computational fluid methods. The off-diagonal components of the stress tensor and the shear rate obtained numerically are compared with the analytical solution in Fig. 6.4 and Fig. 6.6 for different values of α, in the case $n = 1$. One can observe how the shear stress is affected by the shear-thinning degree n in Fig. 6.5. In these simulations, $Re = 100$ and $\alpha = 15$.

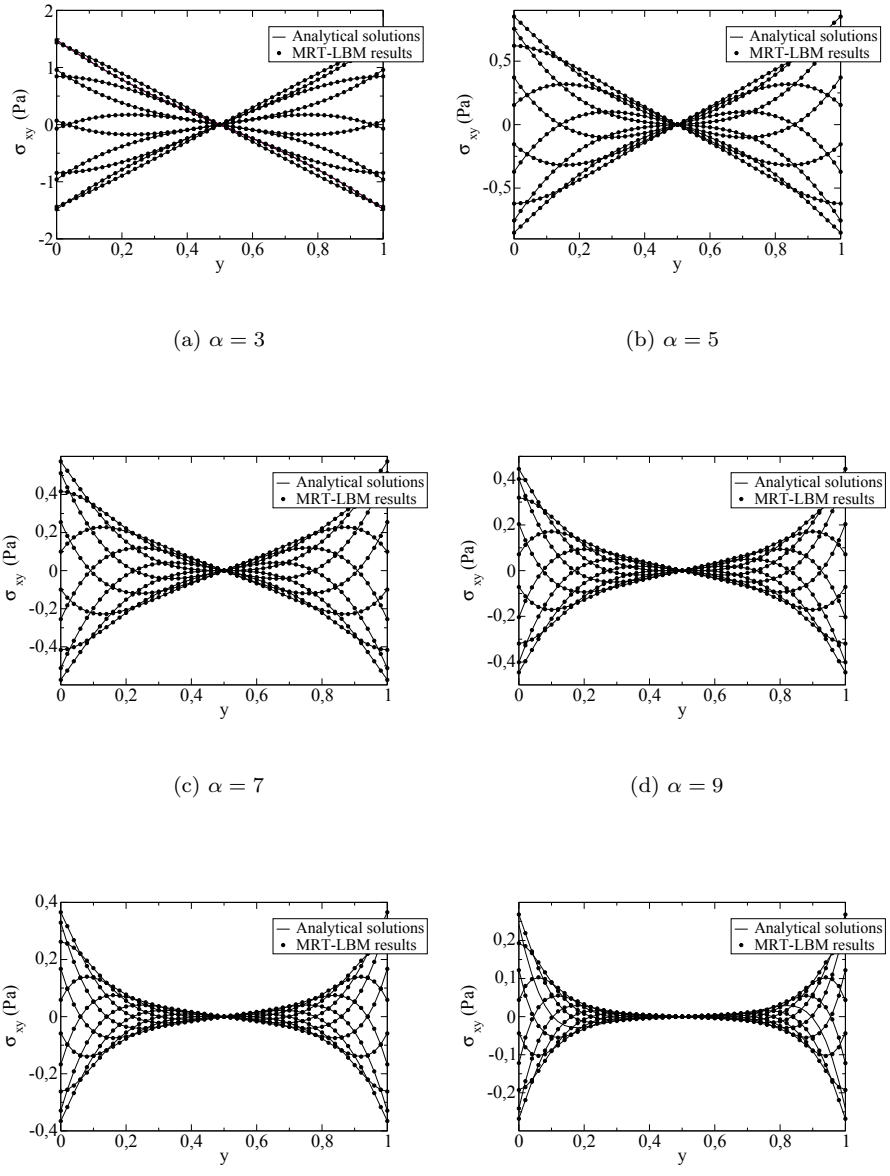

(a) $\alpha = 3$ (b) $\alpha = 5$

(c) $\alpha = 7$ (d) $\alpha = 9$

(e) $\alpha = 11$ (f) $\alpha = 15$

Figure 6.4: **Shear stress profiles in a complete period T for a Womersley Newtonian flow ($n = 1$) for different values of α.**

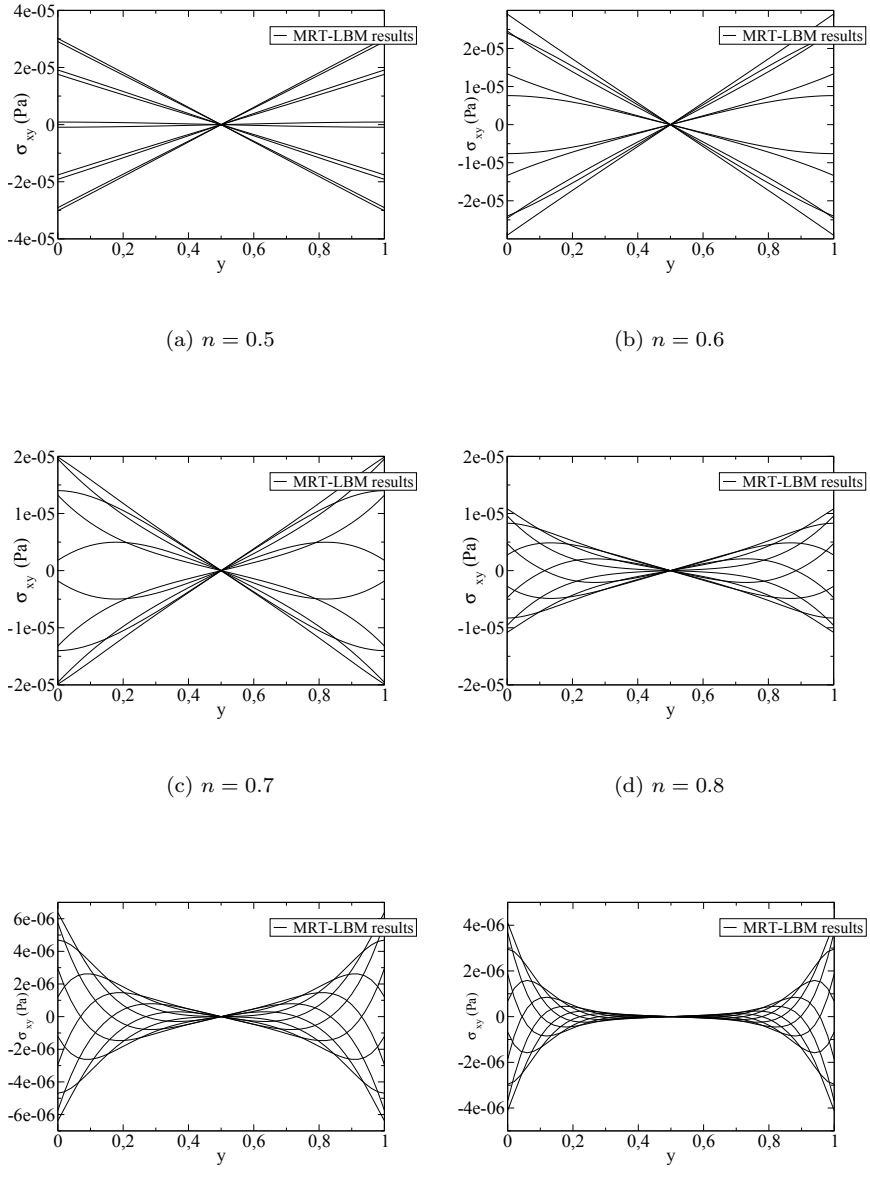

(a) $n = 0.5$ (b) $n = 0.6$

(c) $n = 0.7$ (d) $n = 0.8$

(e) $n = 0.9$ (f) $n = 1.0$

Figure 6.5: **Shear stress profiles in a complete period T for a Womersley flow with $\alpha = 15$, for different values of n.**

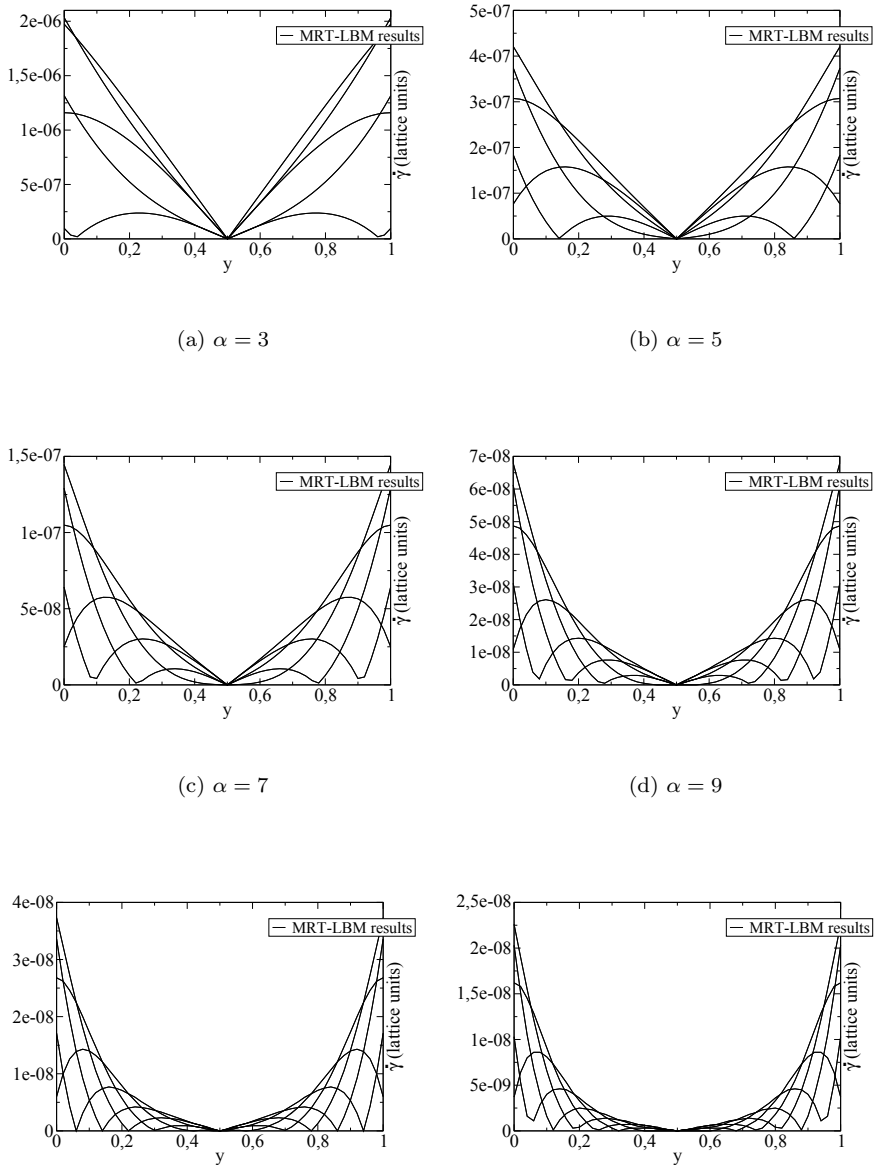

(a) $\alpha = 3$ (b) $\alpha = 5$

(c) $\alpha = 7$ (d) $\alpha = 9$

(e) $\alpha = 11$ (f) $\alpha = 13$

Figure 6.6: **Shear rate profiles in a complete period T for a Womersley flow ($n = 1$) for different values of α.**

The main characteristic of non-Newtonian fluids is their apparent viscosity, producing a complex flow where the kinematic viscosity depends of the shear rate at each location. Taking advantage of the facilities offered by the method to calculate the shear stress tensor, the apparent viscosity of the flow is found at each node and time step generating viscosity profiles as those shown in Fig. 6.7.

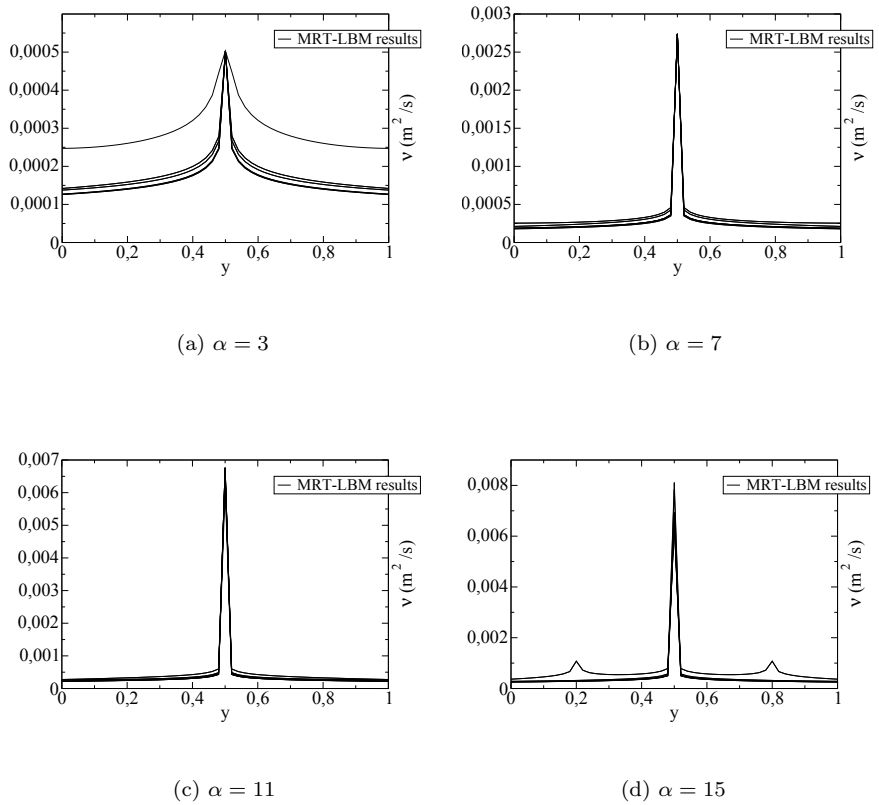

(a) $\alpha = 3$

(b) $\alpha = 7$

(c) $\alpha = 11$

(d) $\alpha = 15$

Figure 6.7: **Apparent viscosity profiles in a complete period T for a pulsatile flow ($n = 0.828$) for different values of α.**

The largest viscosity values are found at the center of the channel, although for $\alpha = 15$ two additional (smaller) peaks appear near the channel walls. Probably these are responsible of the flat velocity profiles characteristic of pulsatile flows at high Womersley values. This can be appreciated in Fig. 6.8, where for $t = 0.1T$ and $\alpha = 15$ the location of these viscosity peaks matches that of the maximum values of the velocity. Nevertheless the amplitude of this normalized velocity profile is the smallest as compared with those at different times within the period.

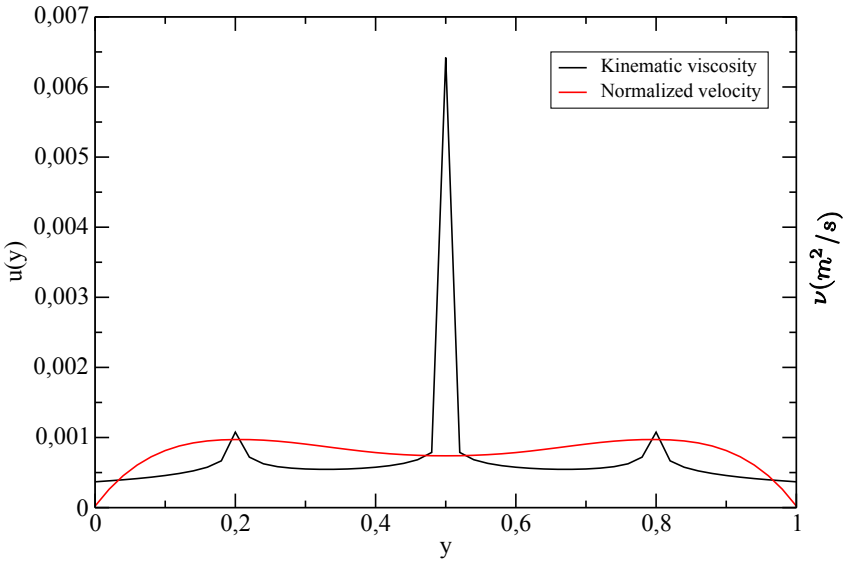

Figure 6.8: **Comparison of the normalized velocity profile (red line) with the kinematic viscosity profile (black line) at $t = 0.1T$.**

The maximum velocity developed in non-Newtonian flows is reduced significantly as compared with the Newtonian velocity profiles. However, the ampli-

tude or maximum normalized velocity in a period increases when increasing the Reynolds number. In Fig. 6.9, we show the normalized velocity profiles in a whole period, with $\alpha = 3$ for different Reynolds numbers.

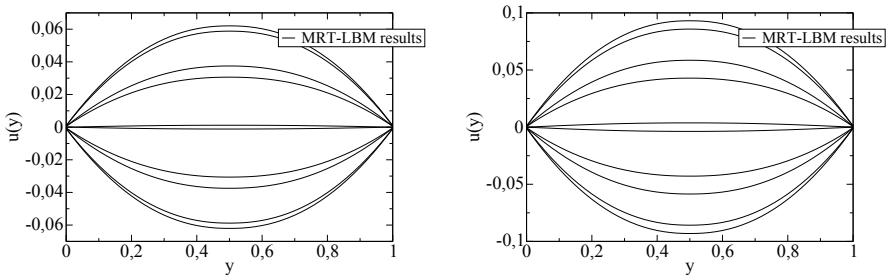

(a) $Re = 0.01$ (b) $Re = 0.07$

(c) $Re = 0.3$ (d) $Re = 1.0$

Figure 6.9: **Normalized velocity profiles in a complete period T in a pulsatile flow ($n = 0.828$) with $\alpha = 3$ for different values of the Reynolds number.**

As an attempt to characterize the increase of the amplitude of the velocity os-

cillation with the Reynolds number, the maximum of the velocity developed for different values of α is drawn as a function of the Reynolds number in a log-log plot (Fig. 6.10). The amplitude is greater for low Womersley numbers, in accordance with the behavior of Newtonian pulsatile flow (see Fig. 6.1). Additionally, for Womersley numbers $\alpha < 9$ the log-log graphic shows an exponential correlation, whereas for ($\alpha > 9$) the tendency starts to change. Although a relation indeed exists, quantifying the general relation between the maximum velocity and the Reynolds and Womersley numbers does not look straightforward.

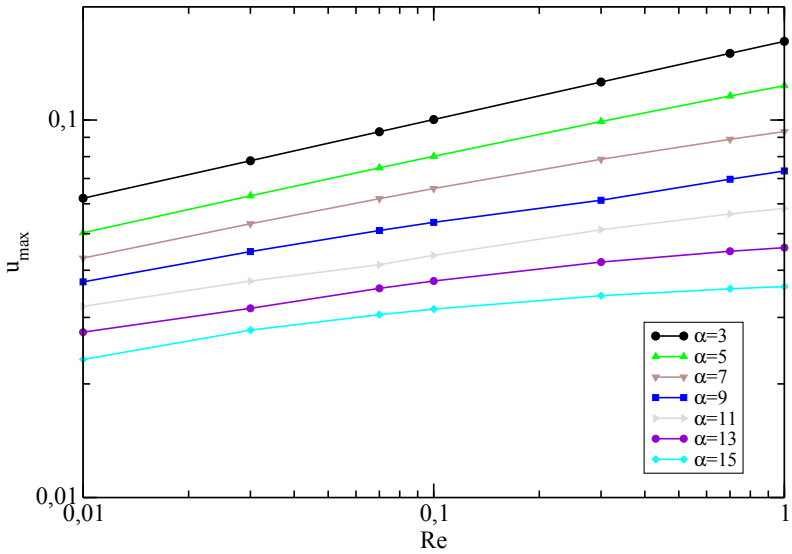

Figure 6.10: **Log-log plot of the normalized maximum velocity over one period vs Reynolds number.**

Chapter 7

Lax-Wendroff method in transport applications

In this chapter, heat and mass transfer processes are simulated using the Lax-Wendroff (L-W) finite difference method (see Chap. 3) for solving the advection-diffusion equation 3.1. The main aim of this part of the work is to test the abilities and accuracy of the chosen method to account for the mass transport processes in our micro-device. The conventional method implements a uniform grid to solve these problems. It will allow us to focus on basic knowledge, like stability criterion, accuracy and boundary conditions among others, to have a complete understanding of the method performance.

7.1 Advection-diffusion of a Gaussian pulse

The initial problem of a Gaussian pulse diffusing in a flow with a constant velocity can be solved analytically. If the initial value of a scalar field obeys the Gaussian distribution (Gaussian pulse) in two dimensions, we have

$$c(x, y, 0) = \frac{c_0}{2\pi\sigma_0^2} e^{\left(-\frac{1}{2}\frac{(x^2+y^2)}{\sigma_0^2}\right)}, \tag{7.1}$$

where c_0 is the initial concentration and σ_0^2 is the initial variance. The analytical solution at any time can be expressed by

$$c(x,y,t) = \frac{c_0}{2\pi(\sigma_0^2 + 2Dt)} e^{\left[-\frac{1}{2}\left(\frac{(x-u_x t-x_0)^2+(y-u_y t-y_0)^2}{\sigma_0^2+2Dt}\right)\right]}. \tag{7.2}$$

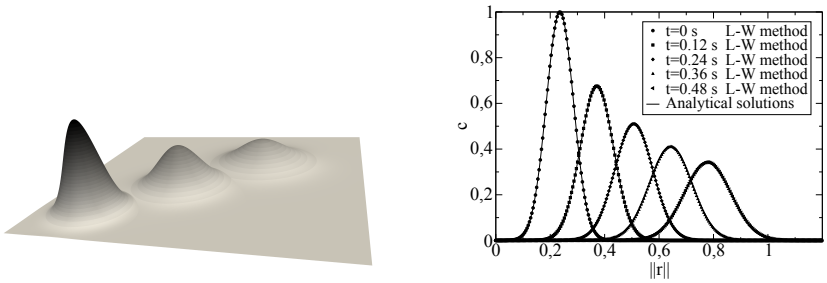

(a) Concentration field at different times

(b) Concentration profiles at several times along $x = y$

Figure 7.1: **Advection-diffusion of a Gaussian pulse with $u_x = 0.8$ and $u_y = 0.8$ lattice units.**

In the numerical test, the domain is $x \in [0,1]$ and $y \in [0,1]$, which is divided in a 320×320 grid mesh. The initial concentration is $c_0 = 2\pi\sigma_0^2$ with $\sigma_0 = 0.05$. The velocity of the flow field in lattice units is $\vec{u} = (0.8, 0.8)$, the initial central position of pulse is located at $(1/6, 1/6)$, and the lattice diffusivity used in this simulation was $D = 0.005$. Five times were selected $t = 0, 0.12, 0.24, 0.36, 0.48$ s, in order to compare the L-W results with the analytical solution 7.2.

	t=0 s	t=0.12 s	t=0.24 s	t=0.36 s	t=0.48 s
L2 error	$1e{-}10$	0.0016064	0.00253531	0.00394769	0.0059070

Table 7.1: **Error of the solution obtained by the Lax-Wendroff method.**

Concentration profiles along the line $x = y$ (L-W results and analytical solution at different times) are shown in Fig. 7.1. The advection process is well accounted for, as the location of the peak of the Gaussian pulse shows (b). Similarly, the diffusion process that governs the rate of spreading of c into the medium is well modeled by the method. The $L2$ error is shown in Table 7.1. As it can be seen, there is a good agreement with the analytical results as well as a good accuracy. However, as time advances, the L2 error increases, not in a large proportion but it may be necessary to keep this in mind if accuracy issues become critical.

7.2 Heat transfer by convection-diffusion in a moving bar

The classical two-dimensional test problem of a moving bar was used [40] to consolidate the capability of our L-W model (see Fig. 7.2). It is standard problem for heat transfer by convection-diffusion in a long bar of length l, moving with a constant velocity u_x with scalar variable values specified in the edges $T(0, y) = 1$ and $T(l, y) = 0$. Despite the problem is bi-dimensional, using the proper boundary conditions in the additional coordinate, we have implemented a three-dimensional scheme to solve this problem, aiming at validating the hybrid code that we will use in the next chapter.

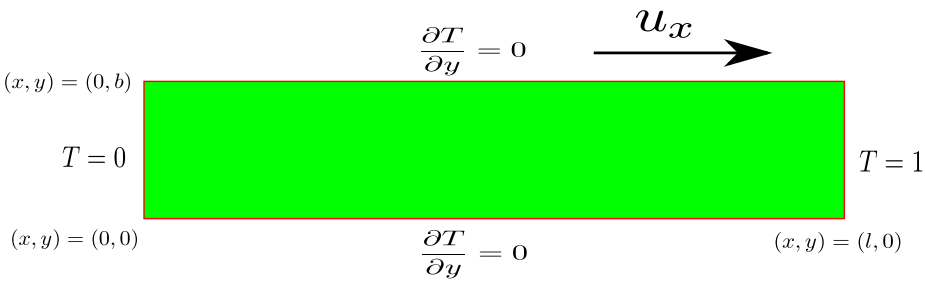

Figure 7.2: **Geometrical properties of the numerical model for a moving bar, with boundary conditions.**

The system domain is defined as $\Omega = [(x, y, z) : x \in (0, l), y \in (0, b), z \in (0, h)]$, and the rest of boundary conditions are $\partial T/\partial y(x, 0, z) = \partial T/\partial y(x, b, z) = 0$. In

our simulation the dimensions were $l = 1$ $b = 0.3$ and $h = 0.05$, with spacings $\Delta x = \Delta y = \Delta z = 0.01$. The diffusivity was taken as $D = 1$ and the Péclet number was assumed to be $Pe = u_x$, working in dimensionless units.

The exact solution is given by:

$$T(x,t) = T_0 \left[\frac{1 - e^{Pe(x/l-1)}}{1 - e^{-Pe}} \right] \tag{7.3}$$

where Pe is the Péclet number, that relates the convection or advection velocity of the flow to the rate of diffusion.

Péclet number	0.01	0.1	1	10	20	30
L2 error ($\times 10^{-4}$)	3.22	3.25	2.96	1.34	3.68	6.63

Table 7.2: **Error in the numerical solution of the long bar problem.**

The plots in Fig. 7.3 show the temperature distribution along the moving bar for different values of the Péclet number, the same as in Table 7.2. As one can see, the three-dimensional Lax-Wendroff method is able to solve with good accuracy convection-diffusion problems for a medium range of Péclet numbers without resorting to techniques to improve the performance of the method. In the next chapter, a non-uniform grid (of stretching type) is implemented to extend the Péclet values in which our code works properly.

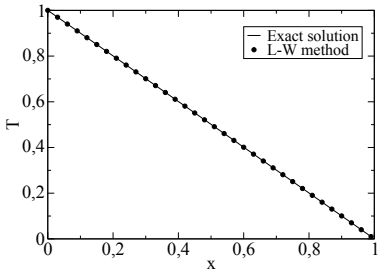

(a) $Pe = 0.01$

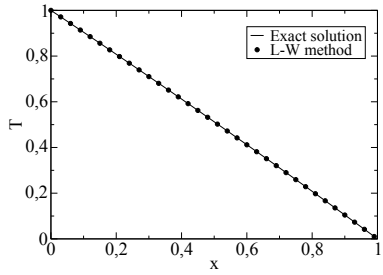

(b) $Pe = 0.1$

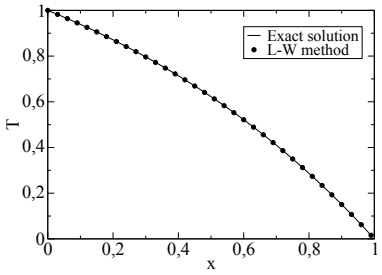

(c) $Pe = 1.0$

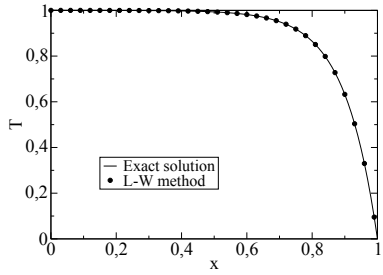

(d) $Pe = 10$

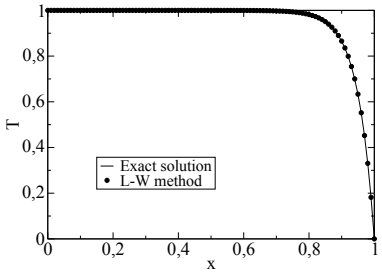

(e) $Pe = 20$

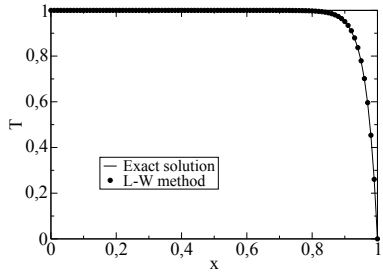

(f) $Pe = 30$

Figure 7.3: **Temperature distribution along the bar for different Péclet numbers.**

Chapter 8

Hybrid LBM-FD model

Mass transport in fluid flow can be modeled by coupling different numerical methods (hybrid model). In our case, the hydrodynamic equations (Navier-Stokes equations) were solved using the lattice Boltzmann method which is able to compute local shear rate through a simple algorithm. Therefore, the simulation of non-Newtonian fluids becomes natural as was shown in previous sections. Concurrently, the mass transport was modeled using Lax-Wendroff scheme which is a finite difference (FD) method. Such schemes have been widely used due to its simplicity and low computational cost. Additionally, they offer the possibility of implementing non-uniform grids to avoid instabilities and better accuracy of the results.

The velocity field computed by the LBM is used for the Lax-Wendroff scheme to compute the concentration field of the substance which is transported by advection and diffusion. For this purpose, the FD scheme must be coupled to the LBM routine (see Fig. 2.5). After computing the macroscopic variables in the LBM, the evolution routine of the concentration field (FD scheme) is called to use the recently calculated LBM velocity field. A scheme of the hybrid routine can be seen in Fig. 8.1.

Unlike the LBM, the finite difference model is here implemented in a non-uniform grid. A geometric series was used to have a better resolution in regions with larger concentration gradients (for example areas near the walls or inside the micro-porous membrane). The difference between the grids used in both models means that the nodes do not have matching positions, making an inter-

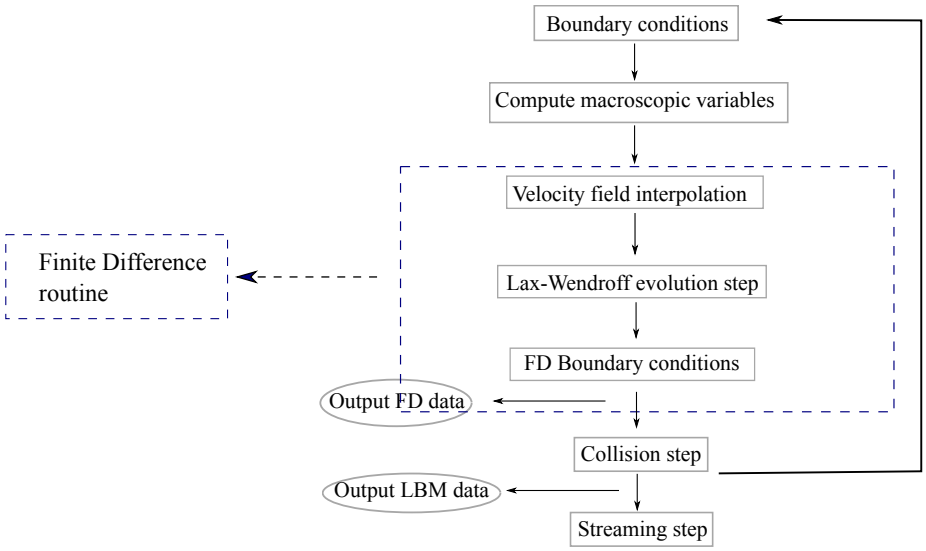

Figure 8.1: **Computational routine in the LBM-FD hybrid model.**

polation of the velocity data necessary, for its use in the non-uniform material grid.

8.1 Non-uniform grid (stretching)

Storage requirements, computer time, and run cost of numerical simulations are largely controlled by the number of nodes in the grid. Thus, it is desirable to use the smallest number of nodes which will yield the accuracy required for the solution. Additionally, a refinement in those areas where the concentration gradients are larger can provide greater stability, and therefore better results. Adequate refinement in areas near the walls or inside of the micro-porous membrane can improve the simulation.

A refinement of the coarse grid, denser in critical areas can be done by means of a geometric series. For $r \neq 1$, the sum of the first n terms of a geometric

series is

$$a + ar + ar^2 + ar^3 + ... + +ar^{n-1} = \sum_{k=0}^{n-1} ar^k = a\left(\frac{1-r^n}{1-r}\right) \tag{8.1}$$

where a is the first term of the series, and r is the common ratio that determines the progression ratio of successive terms in the series. If $r \to 1$ the grid is uniform, but as r moves away from 1, the rate of increase of the distance between neighboring nodes will be bigger. In this way, it is possible to generate a stretching of the grid to have a better resolution in desired areas, sacrificing the resolution in areas of less interest.

8.2 Bilinear interpolation in two dimensions

As a consequence of the spatial discretization, the results obtained can be considered as approximations to a function $f(\vec{x})$ known at a set of discrete points $\vec{x_1}, \vec{x_2}, ..., \vec{x_N}$. However we do not have the analytical expression of $f(\vec{x})$ that would let us calculate its values at arbitrary points. In our case, the velocity field from LBM consists in values of a function $u(\vec{x})$ known only at discrete positions. From these velocity values, values at other positions can be interpolated, that coincide with the location of the nodes of the non-uniform grid used in the FD scheme. The bilinear interpolation is frequently used as a first approximation in two-dimensional problems, giving us a tool to connect both grids. Finally, we will end up having a complete routine for our hybrid LBM-FD model (see Fig. 8.1).

Imagine as an example, a two-dimensional problem where we are given a matrix of functional values $ya = [1..M][1..N]$. We are also given two arrays $x1a[1..M]$ and $x2a[1..N]$ where M and N are the number of columns and rows respectively. The relation of these input quantities to an underlying function $y(x_1, x_2)$ is [56]

$$ya[j][k] = y(x1a[j], x2a[k]) \tag{8.2}$$

We want to estimate, by interpolation, the function y at some untabulated point (x_1, x_2). The key concept is the vicinity of the point (x_1, x_2), that is, the four tabulated points that surround the desired interior point. More precisely, if

$$\begin{aligned} x1a[j] \leq x_1 \leq x1a[j+1] \\ x2a[k] \leq x_2 \leq x2a[k+1] \end{aligned} \tag{8.3}$$

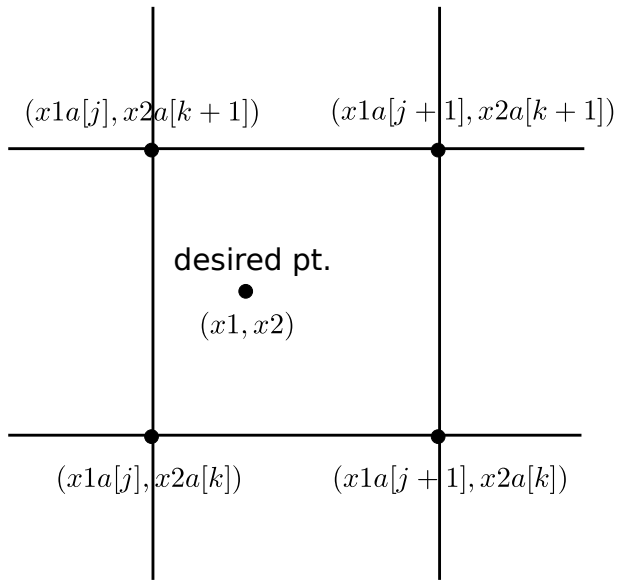

Figure 8.2: **Points used in the two-dimensional bilinear interpolation.**

defines j and k, then

$$\begin{aligned} y_1 &\equiv ya[j][k] \\ y_2 &\equiv ya[j+1][k] \\ y_3 &\equiv ya[j+1][k+1] \\ y_4 &\equiv ya[j][k+1] \end{aligned} \tag{8.4}$$

The bilinear interpolation on the grid square is given by the formulas

$$\begin{aligned} t &\equiv (x_1 - x1a[j])/(x1a[j+1] - x1a[j]) \\ u &\equiv (x_2 - x2a[k])/(x2a[k+1] - x2a[k]) \end{aligned} \tag{8.5}$$

(so that t and u each lie between 0 and 1), and

$$y(x_1, x_2) = (1-t)(1-u)y_1 + t(1-u)y_2 + tuy_3 + (1-t)uy_4 \quad , \tag{8.6}$$

Using the bilinear interpolation in two dimensions, the velocity values at the nodes of the non-uniform FD grid can be found and subsequently, the evolution

of the concentration can be computed at each time step.

Once we have implemented all the elements in our LBM-FD hybrid model, the well-known Graetz-Leveque problem of boundary layer mass flux can be reproduced. The goal is to obtain a model capable to simulate mass transport at high Péclet numbers, as we will see in the next section.

8.3 Graetz-Leveque problem of boundary layer mass flux

The mass transfer across the membrane can be characterized by the mean Sherwood number $< Sh >$ along the membrane length L

$$< Sh >= \frac{1}{L} \int Shdx \quad , \tag{8.7}$$

where Sh is the local non-dimensional mass transfer rate or Sherwood number, $Sh = \frac{hK}{D}$. The mass transfer coefficient K can be calculated from the local mass transfer rate $N^{''}|_s$ through a surface, which is defined as

$$N^{''}|_s = -D\frac{\partial C}{\partial z}|_s = K(C_0 - C_w) \quad , \tag{8.8}$$

where C_0 is the bulk concentration and C_w is the concentration at the active region of the surface or membrane.

The study will be carried out by measuring the value of the average Sherwood number $< Sh >$ as a function of the Péclet number in the permeate channel, defined as

$$Pe = ReSc = \frac{u_{max}H}{D} \quad , \tag{8.9}$$

where Re is the Reynolds number. A dimensional analysis of the convective mass transfer in simple flows and geometries (flat plate, single sphere, spherical bubble swarms, through pipes, wetted-wall columns, etc.) shows the influence of the Schmidt, Reynolds and Péclet numbers, $Sh = f(Rey, Sc) = f(Pe)$ [26]. If mass transfer occurs through a microporous membrane, variables such as porosity or tortuosity may also play an important role in packed and fluidized beds.

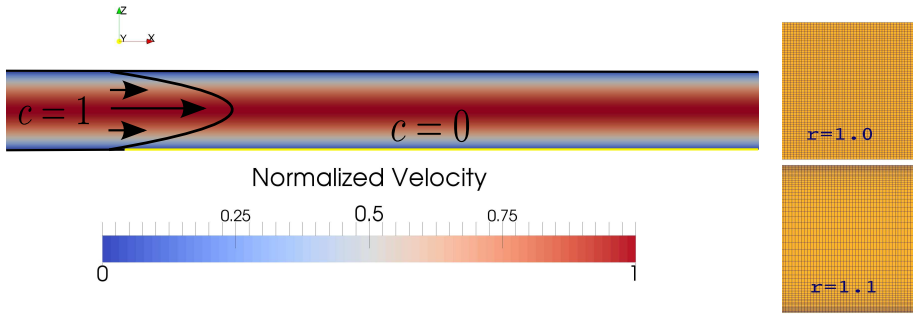

Figure 8.3: **Sketch of the model set-up (left) and the non-uniform grid discretization (right) used for the solution of the Graetz-Leveque problem.**

At low Reynolds numbers, with a no-slip boundary condition on the walls, a Poiseuille flow is developed inside the channel. An electrode is located at the bottom boundary, its length being ten times larger than the channel height H. The length of the undisturbed region at the inlet is equal to H. In this way, the length of the catalyst along the flow direction is $L = 9$ (see Fig 8.3-left). If the reaction is infinitely fast, one can assume that the concentration vanishes at this boundary, $C = 0$. Inflow concentration is $C = 1$. In the outflow a convective flux condition $\partial C/\partial x = 0$ is chosen.

Seeking better stability and accuracy at high Péclet numbers, we use a non-uniform grid for the evolution of the concentration field, coarser in the center of the channel and more refined approaching the walls. For this purpose a mesh is built based upon a geometric series in the upper half of the channel; the bottom half is constructed symmetrically (see Fig 8.3-right). We use three values for the common ratio $r = 1.0$ (uniform grid), $r = 1.05$ and $r = 1.1$ in the geometric series. The time step is chosen constant throughout the mesh and is determined by the Courant-Friedrich-Levy stability condition.

Simulations are performed for different values of the Péclet number. Fig 8.4 shows the concentration inside the channel when the steady state is attained.

At high Pe, convection is dominant and a material boundary layer is established at the catalyst boundary, which becomes thinner with increasing Péclet number.

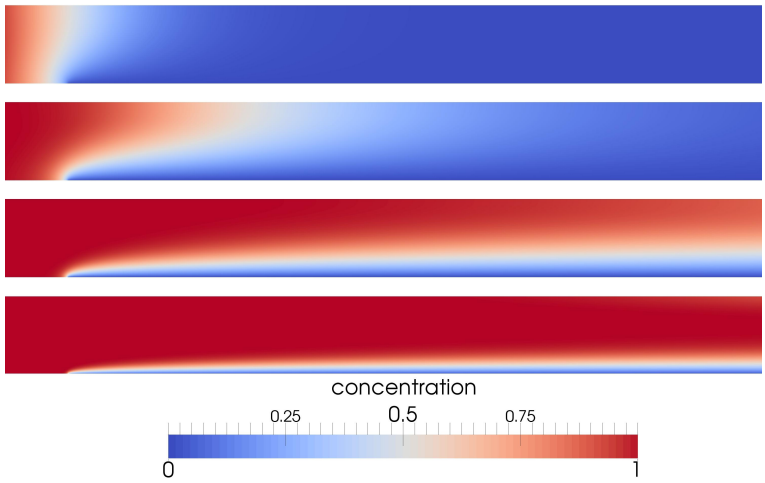

Figure 8.4: **Steady concentration field for different Péclet numbers in the Graetz-Leveque problem; from top to bottom: Pe=1,10,100,1000.**

In Fig 8.5, we show $< Sh >$ calculated with Eq. (8.7) as a function of Pe, obtained for different values of the common ratio r used to refine the mesh near the walls and the results are compared with the values reported by Holzbecher [21]. Two distinct regions can be appreciated; for high Pe, the Sherwood number obeys the Leveque one-third power law. The transition zone between the two asymptotics appears for Pe between 0.3 and 30. Only the highest refinement $r = 1.1$ is capable to reproduce accurate results for Pe $\gtrsim 10^6$.

The validated LBM-FD hybrid code will serve to model the mass transfer through a hydrophobic membrane with rectangular through-holes in a micro-device with two parallel micro-channels. The 2D case is interesting on its own, as it retains the basic features of the full three dimensional problem at a much smaller computational cost. In the same way, the 3D model of the micro-device gives us a more realistic description of the processes involved.

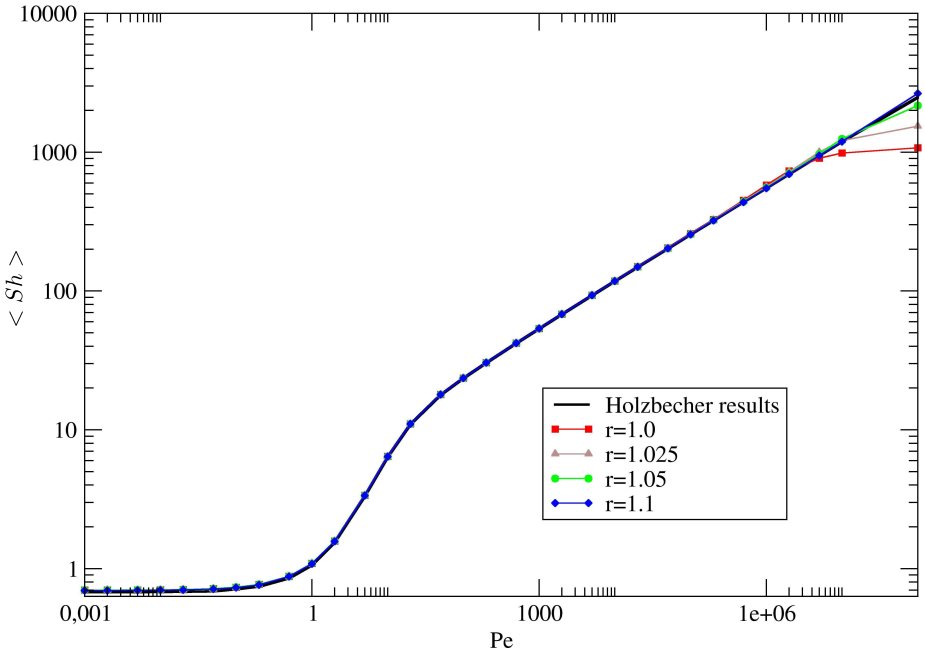

Figure 8.5: **Péclet vs Sherwood numbers for a catalyst length L=9 for different common ratio values of the mesh refinement.**

Chapter 9

Mass transport through membranes

9.1 Mass transport in a 2D upper membrane wall channel

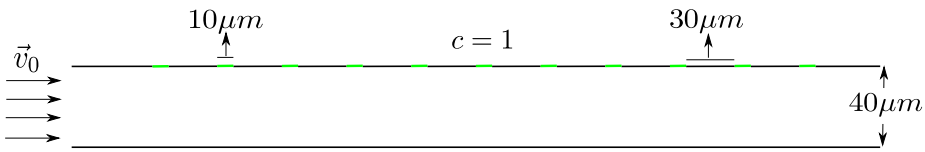

Figure 9.1: **Scheme of a 2D upper membrane wall channel with a constant concentration $c = 1$ entering in a power-law blood velocity-driven flow.**

Our first situation consist of a blood flow (power-law model) passing through a rectangular channel. The blood parameters used in these simulations were taken from Table 4.1 where the parameters have been determined experimentally by means of different techniques. Three particular cases have been taken and labeled as: case 1, taken from Kim et.al. [51] ($n = 0.828$, $k = 0.00927$ Pas^n), case 2, taken from Walburn and Schneck [57] ($n = 0.775$, $k = 0.0148$ Pas^n), and case 3: taken from Liepsch and Moravec [32] ($n = 0.61$, $k = 0.042$ Pas^n). In all cases, a constant velocity-driven flow is implemented using Zou-He

boundary conditions at the inlet to impose a constant velocity ($u_{0lb} = 0.0001$) and a constant density at the outlet ($\rho_{lb} = 1$). The width of the channel is $W_p = 40$, μm and $Re = 0.1$, all being characteristic values of blood flows in arterioles. We used $W_{lb} = 50$ and the number of pores implemented in the channel was 24. The first pore is located at a sufficient distance from the inlet to ensure a fully developed flow at a distance of $5W_{lb}$ from the entrance, as we found from the study of shear-thinning power-law flows accomplished in Sec. 5. A no-slip full-way bounce-back boundary condition is used at the walls $\vec{u} = 0$.

On the other hand, a constant concentration is entering the channel through a set of micro-pores located on the upper wall, where a Dirichlet boundary condition $c = 1$ is implemented. The width of each pore is 10 μm and the distance between them is 30 μm as seen in Fig. 9.1. A non-uniform grid is used in the channel for the mass transport simulation with a common ratio $r = 1.1$. In this way, a parametric study was done varying the Péclet number of the system, and once the concentration reached a steady state, the mean Sherwood number across the active zone (pores) was measured.

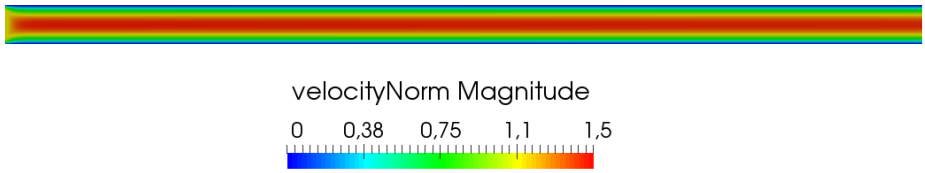

Figure 9.2: **Normalized velocity field of the upper wall membrane flow in its steady state for $n = 0.828$ (case 1).**

Fig 9.2 shows the normalized velocity field once the steady state is reached. As in the previous section, a transition zone is located around the inlet, its

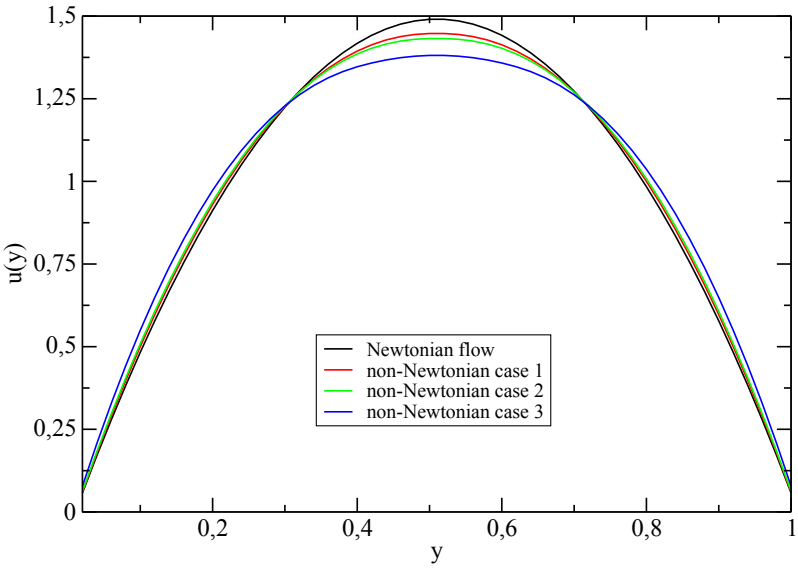

Figure 9.3: **Velocity profiles for different blood parameters.**

length depending of the sher-thinning degree. Once this zone is past, a fully developed flow zone is found until the end of the channel. In Fig. 9.3 the velocity profiles measured in the fully developed flow zone are shown. Case 3, with a higher shear-thinning behavior ($n = 0.61$) has a more prominent flat shape and its magnitude is the lowest among all cases. On the opposite side, case 1 ($n = 0.828$) shows a behavior closer to Newtonian flow, as we expected. Although there are differences in the maximum velocities, the largest difference between them is close to 8% as compared with the Newtonian case (case 3). As a consequence of these small differences, the difference in the measured mass transport (mean Sherwood number) between the three cases is also small.

Once the velocity field reaches the steady state, a constant concentration is introduced in the channel through the pores (see Fig. 9.1). A set of simulations

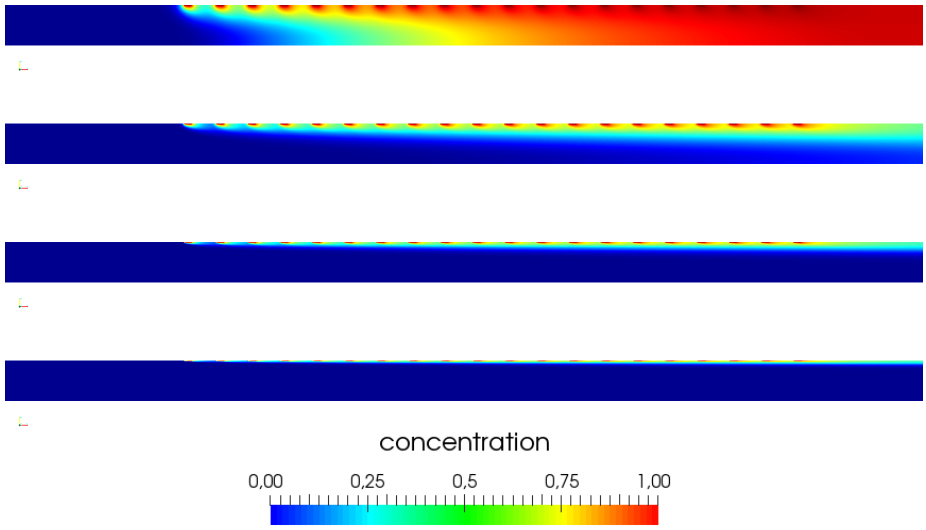

Figure 9.4: **Concentration fields in the steady state for** $n = 0.828$ **(case 1); from top to bottom:** $Pe = 10, 100, 1000, 10000$**.**

varying the Péclet number ($1 \leq Pe \leq 100000$) were made. The concentration field for different values of the Péclet number in the steady state is shown in Fig. 9.4 for $n = 0.828$ (case 1). As in the Graetz-Leveque problem, at high Pe, convection is dominant and a material boundary layer is established at the catalyst boundary, which becomes thinner with increasing the Péclet number.

The mean Sherwood number as a function of the Péclet number shows two zones, as can be seen in Fig. 9.5. For $Pe \leq 10$, the diffusion process dominates the evolution of the concentration, filling the whole channel and producing the same mean Sherwood values as a result. In the next zone ($Pe > 10$) the advection process of the flow starts to acquire relevance, and determines the mass transport in the channel. As we expected, the largest difference found in the mean Sherwood number between the Newtonian flow and the three blood parameters cases is close to 5% for $case3$, which has the largest shear-thinning degree. For the parameters used in this work, characteristic of blood flow, the

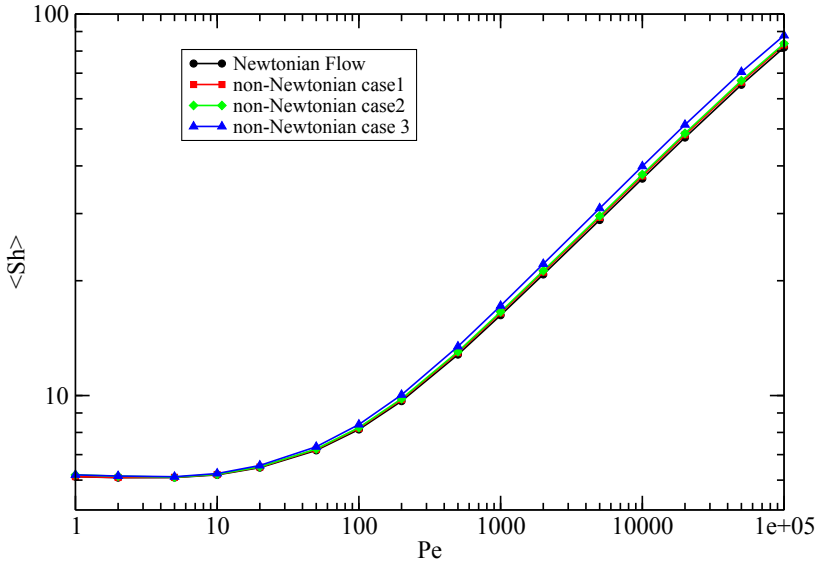

Figure 9.5: **Sherwood vs Péclet numbers for the three blood parameters cases compared with the Newtonian case.**

relative differences are small (5%), due to the fact that the velocity profile is not too far from the Newtonian case.

The same system was used to reproduce the mass transport in a 2D upper membrane wall channel with a pulsatile flow, $Re = 0.1$ and $W_p = 40\ \mu m$ (see Fig. 9.1). An oscillatory velocity-driven flow was implemented at the inlet of the channel by means Zou-He boundary conditions with a period of $T = 200000$ time steps to ensure the stability of the method. At the outlet, a constant pressure was fixed using the same boundary condition (Zou-He). The blood parameters found by Kim et.al. were used in the simulations ($n = 0.828$, $k = 0.00927$ Pa·s^n).

Once the convergence criterion is reached (see Eq. 6.4) for the velocity field, a

constant concentration $c = 1$ is allowed to enter continuously through the pores in the upper wall of the channel. The simulations were carried out for different values of the Péclet $1 \leq Pe \leq 10000$, and the mean Sherwood number was measured across the membrane.

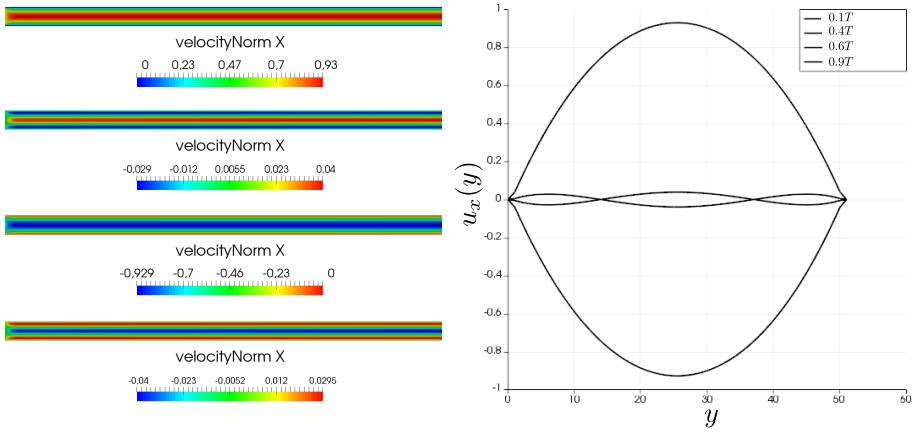

Figure 9.6: **Normalized velocity field (left) and normalized velocity profiles (right) for four different times in a period, from top to bottom:** $t = 0.1T, 0.4T, 0.6T, 0.9T$ **for** $n = 1$ **(Newtonian fluid) and** $\alpha = 3$**.**

In Fig. 9.6 and Fig. 9.7 we show the normalized velocity fields for different times in a period, for Womersley number $\alpha = 3$. The $n = 1$ and $n = 0.828$ cases are shown. For the times when the velocity is a maximum ($t = 0.1T$ and $0.6T$), there are no significant differences between both cases. But for intermediate amplitudes of the velocity ($t = 0.4T$ or $t = 0.9T$), the $n = 1$ profiles change the sign approaching the walls, with respect to the value at the center of the channel.

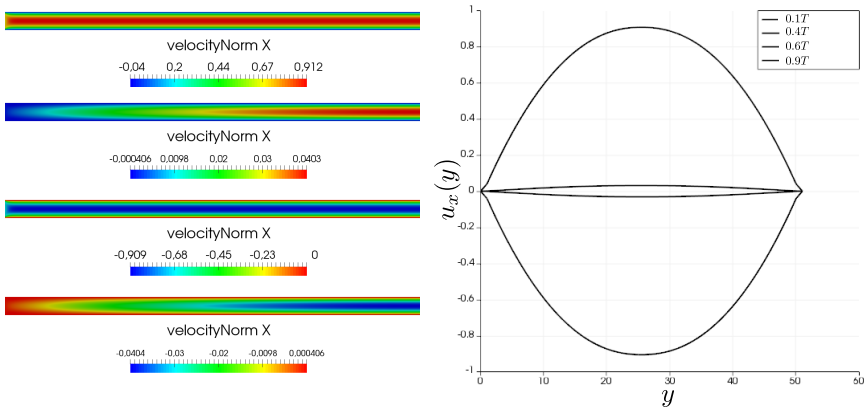

Figure 9.7: **Normalized velocity field (left) and Normalized velocity profiles (right) for four different times in a period, from top to bottom:** $t = 0.1T, 0.4T, 0.6T, 0.9T$ **for** $n = 0.828$ **and** $\alpha = 3$**.**

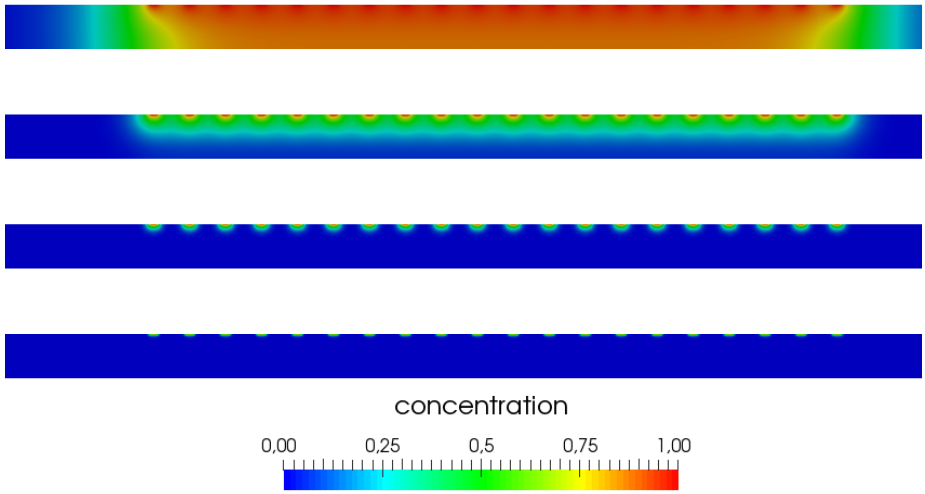

Figure 9.8: **Concentration fields at** $t = 20T$ **for (from top to bottom):** $Pe = 1, 10, 100, 1000$**.**

Changes of direction are not observed for the same times in the velocity profiles of the power-law case $n = 0.828$. These differences could be caused by an insufficiently developed flow in the middle of the channel (where the data were taken), but in the area near the outlet of the channel, where the flow should be completely developed, the situation is the same. We can find a possible explanation in the results obtained for power-law fluids in a velocity-driven flow (see Fig. 5.10) where we observed a dependence of the length of the transition zone on the shear-thinning degree. Although for $n < 1$ the length of the transition zone is less than five times the width of the channel, in a pulsatile flow, the complexity of a time-dependent flow may change these conditions. Our study of power-law pulsatile flow in Sec. 6, showed that the choice of a force-driven flow eliminated the transition zone of the velocity field.

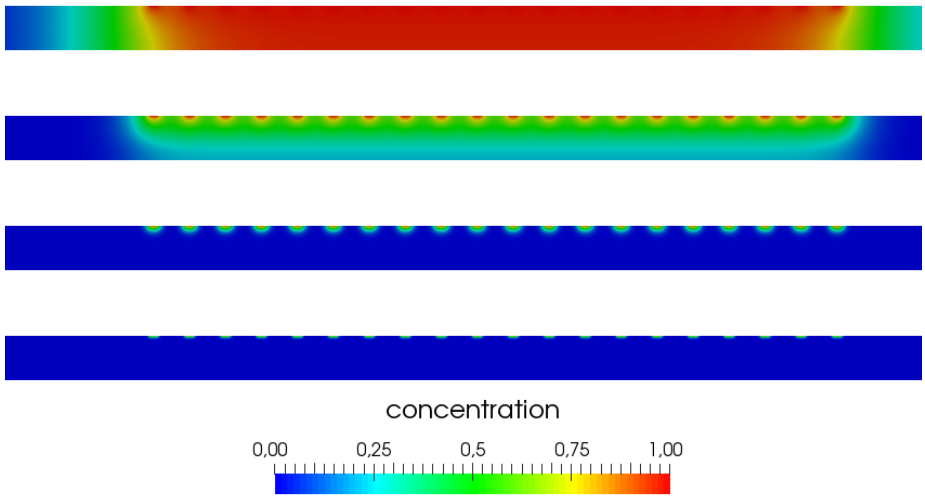

Figure 9.9: **Concentration fields at $t = 40T$ for (from top to bottom): $Pe = 1, 10, 100, 1000$.**

The concentration fields at times $t = 20T$ and $t = 40T$ are shown in Fig. 9.8 and Fig. 9.9, for different Péclet numbers. For lower Péclet numbers, where the diffusion processes are more relevant, the concentration is not affected significantly by the flow and the dispersion into the channel is fast. For the highest

Péclet numbers, the diffusion of the concentration is extremely slow, taking a high computational cost even with the improvements implemented in the hybrid code. Although there is a pulsatile flow advecting the concentration, the mean displacement found in the horizontal direction seems not to be affected. As the pulsatile flow is only in x-direction, the dispersion in the transversal direction (y-direction) should be the same for all the different Péclet numbers.

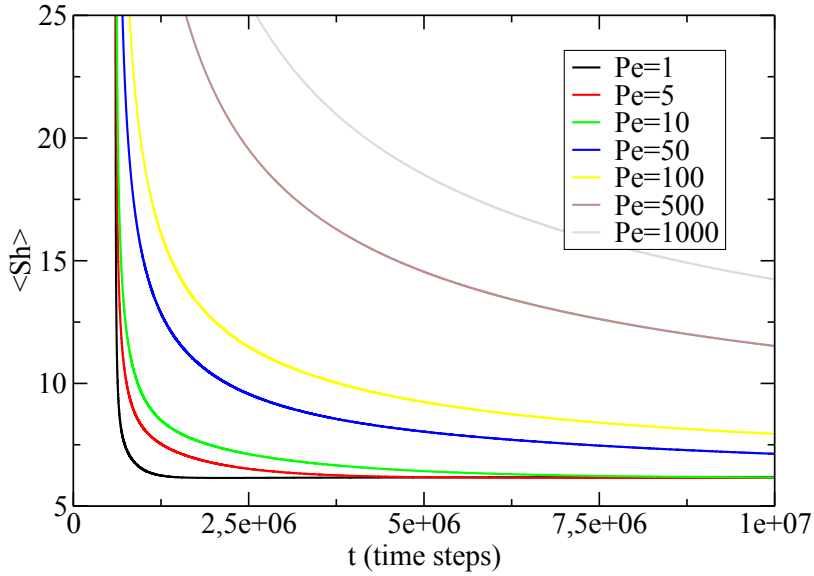

Figure 9.10: **Evolution of the mean Sherwood measured across the pores for several Péclet numbers with $n = 1$.**

The measurements of the mean Sherwood number across the pores for different Péclets are shown in Fig. 9.10 and Fig. 9.11 for $n = 1$ and $n = 0.828$ respectively. As we expected, the pulsatile flow is not affecting the diffusion in the y-direction, in such a way that the mean Sherwood number converges to the same value for all Péclet numbers. The only difference is the time needed by

each simulation to reach a constant mean Sherwood. As a future work, the study and characterization of the transient local Sherwood number is proposed to completely determine the mass transfer in a pulsatile flow.

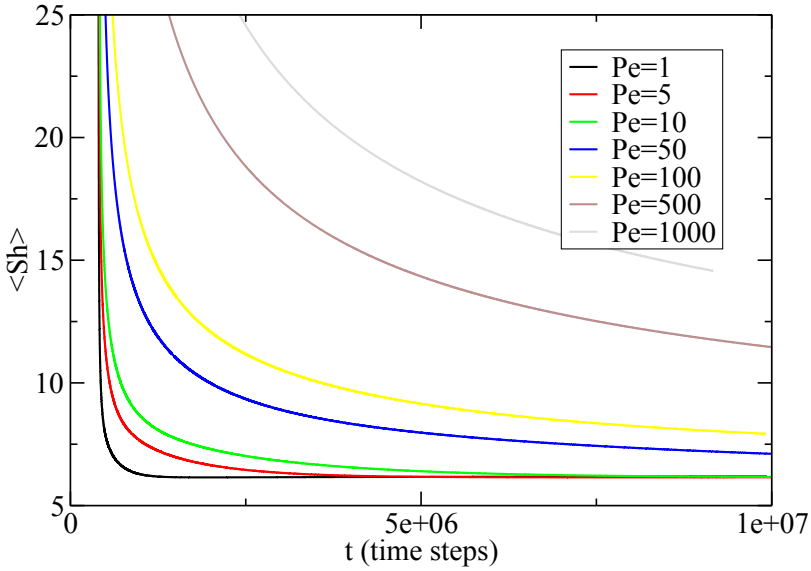

Figure 9.11: **Evolution of the mean Sherwood measured across the pores for several Péclet numbers with** $n = 0.828$**.**

9.2 Mass transfer in a parallel flow micro-device

Inspired by experimental models [11], we consider a microfluidic device with two parallel microchannels separated by a micro-porous membrane with rectangular through-holes. First, a two-dimensional version of such system is analyzed. The 2D system is sketched in Fig 9.12. Each channel has a height $H = 30\ \mu m$

and the thickness of the membrane is $H_m = 10\ \mu m$. The length of each microchannel is assumed to be five times longer than the height. This is a minimal setup to contain a sufficient number of micropores. There is parallel flow in both channels, which are open at the outlet.

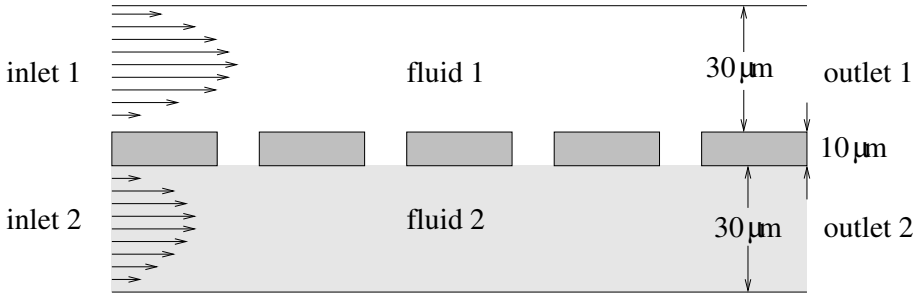

Figure 9.12: **Scheme of our 2D numerical model for the parallel flow micro-device with feed and permeate channels separated by a microporous membrane.**

Once the flow in both channels has reached a steady state, a constant source of concentration is imposed at the inlet of the feed channel. The Froude number ($Fr = u_0/\sqrt{gl_0}$) is relatively high in our model, therefore the effect of gravity is considered to be negligible. Due to the concentration gradient, the material advected by the flow is transferred across the membrane toward the permeate channel. In this study, mass transfer is a blend of convection and diffusion processes and any sort of chemical reaction is neglected.

The system is sketched in Fig. 9.12 and the boundary conditions applied are specified in Fig. 9.13. The kinematic viscosity in the upper channel was $\nu_1 = 0.179\ cm^2/s$ and the Reynolds number was 10. In the lower channel, the viscosity was $\nu_2 = 0.0388\ cm^2/s$ and$Re = 5$. The steady solution for the velocity is the Poiseuille flow in each channel. The mass transfer across the membrane is a pure diffusion process (there is no flow across the pores) where a concentration source $c = 1$ is permanently activated at the inlet of the feed channel (see Fig 9.13). At the solid boundaries and on the membrane walls there is a no-flow condition, and a convective-flux condition is imposed at the channel outlets $\partial C/\partial x = 0$. We studied the mass transfer across the membrane varying the Péclet number in the permeate channel (fluid-1 channel), for a constant

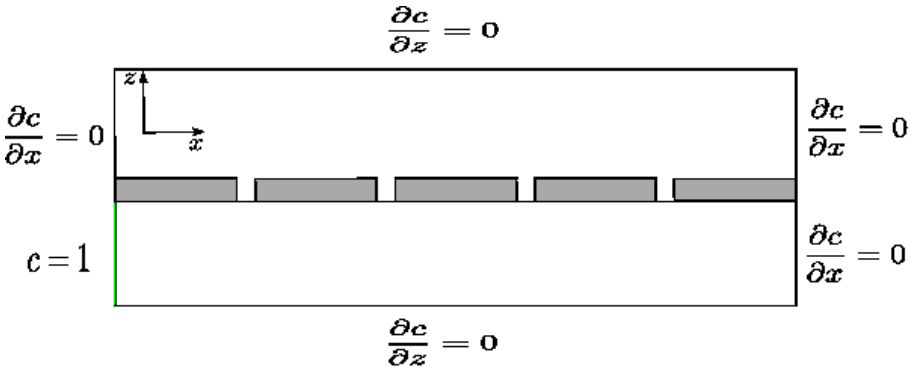

Figure 9.13: **Views of the micro-device with boundary conditions imposed on the concentration field.**

value of the Schmidt number $Sc = 1000$ in the feed channel (fluid-2 channel), see Fig 9.12. Two different membrane porosities were considered: one with five open pores, and another with ten pores, with constant channel length and a pore width of 5 μm.

We used a non-uniform grid with a higher refinement near the membrane in the vertical z-direction, as in the Graetz-Leveque problem. Three different meshes with $r = 1.0$ (uniform grid), $r = 1.05$ and $r = 1.1$ were used, although $r = 1.05$ suffices to give convergent results for $Pe \lesssim 10^5$ as shown in section 8.3. The boundary condition at the interface between both fluids is $J_{fluid_1} = J_{fluid_2}$, where J stands for the diffusion flux across the interface (see Fig 9.14), i.e. in z-direction, as there is no fluid flow through the membrane pores.

In Figs. 9.15 and 9.16, we plot the steady concentration for different values of Pe. At low Péclet numbers the diffusion process dominates the mass transfer toward the permeate channel. As Pe increases, convection increases the mass transfer through the membrane.

The correlations between the average Sherwood number $< Sh >$, calculated from (8.7), and the Péclet number found for the five- and ten-pore membranes are

$$< Sh >= 2.20(3)(PeH/L)^{0.336(5)} \quad , \tag{9.1}$$

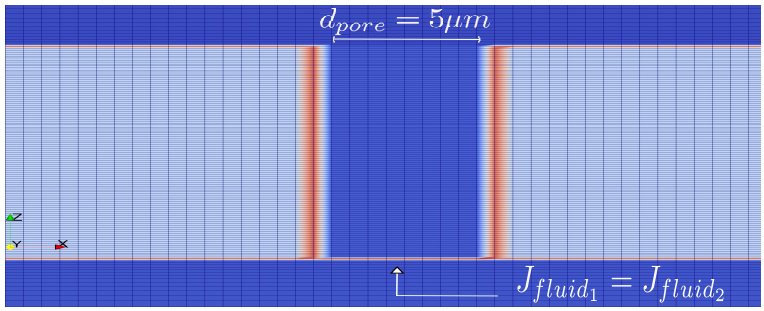

Figure 9.14: **Simulation grid around the pore with the boundary condition specified at the interface between the two fluids.**

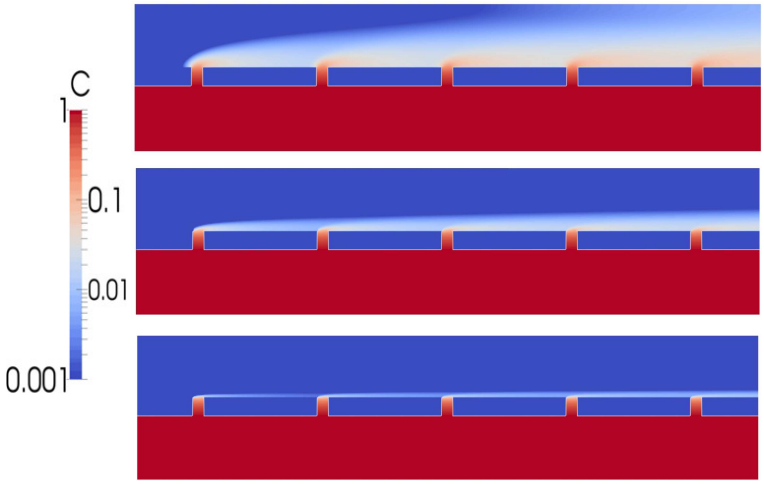

Figure 9.15: **Concentration field for different Péclet numbers for a five-pore membrane in the steady state; from top to bottom: Pe=100, 1000, 10000.**

$$< Sh >= 4.35(3)(PeH/L)^{0.349(5)} \quad , \tag{9.2}$$

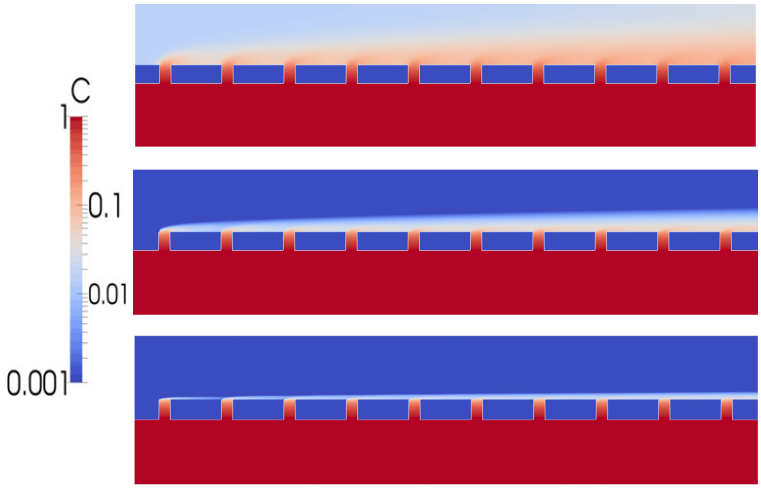

Figure 9.16: **Concentration field for different Péclet numbers for a ten-pore membrane in the steady state; from top to bottom: Pe=100, 1000, 10000.**

respectively, valid for $Pe > 100$. These correlations confirm a linear scaling of $< Sh >$ with the number of pores in this problem. Results obtained with non-uniform grids ($r = 1.05$ and $r = 1.1$) obey the Leveque 1/3 power law as shown in Fig 9.17, unlike those obtained with the uniform mesh $r = 1.0$ (not shown) and as opposed to the Graetz-Leveque problem analyzed in the former section, where the uniform grid sufficed to obtain accurate results for $Pe \lesssim 10^5$ (see Fig. 8.5). On the other hand, the differences found between the results obtained with $r = 1.05$ and $r = 1.1$ are not significant, implying that the concentration gradients near the membrane are well reproduced with $r = 1.05$.

Finally, we study the mass transfer across a membrane in a parallel flow micro-device in three dimensions. The computational model is very similar to the 2D version, with the same total 70 μm in the vertical direction and five times longer in the horizontal direction. The system is 35 μm deep in the third dimension. The 3D parallel flow micro-device is sketched in Fig. 9.18. We carried out simulations varying the Péclet number in the range $50 < Pe < 10000$ in the

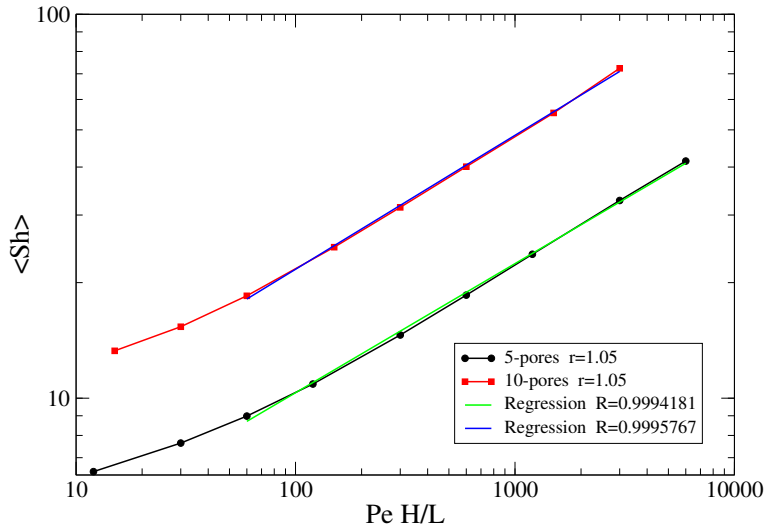

Figure 9.17: **Average Sherwood number vs Péclet number in the two membranes analyzed, calculated after the steady state is reached.**

permeate channel (upper channel), the values of the viscosities being the same as in the 2D case as well as the value of the Schmidt number in the feed channel.

The interleaved pore configuration, as appears in the sketch of the model in Fig. 9.18, is used for a more realistic (and truly 3-dimensional) geometry, in the line of the Lung-on-a-chip micro-device developed in [11]. We have focused on the central part of the micro-device, by using periodic boundary conditions for the momentum and the concentration on the front and rear walls (perpendicular to y). Thus, the steady state flow is a parabolic velocity profile as in the 2D model . On the top and bottom walls, a zero velocity condition is imposed (no-slip boundary condition), see Fig. 9.20. Once the flow in both channels has reached a steady state, a constant source of concentration is imposed at the inlet of the feed channel. The boundary conditions used for the concentration field are shown in Fig. 9.19

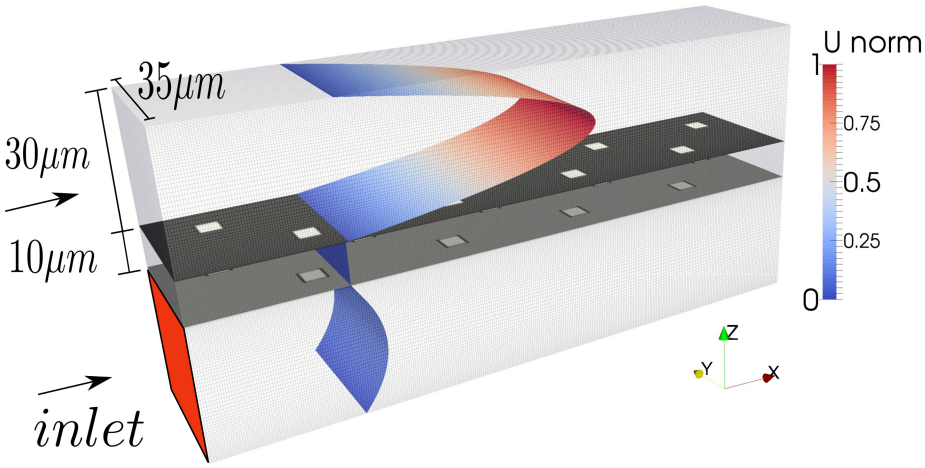

Figure 9.18: **Scheme of our 3D parallel flow micro-device with two rectangular channels separated by a microporous membrane.**

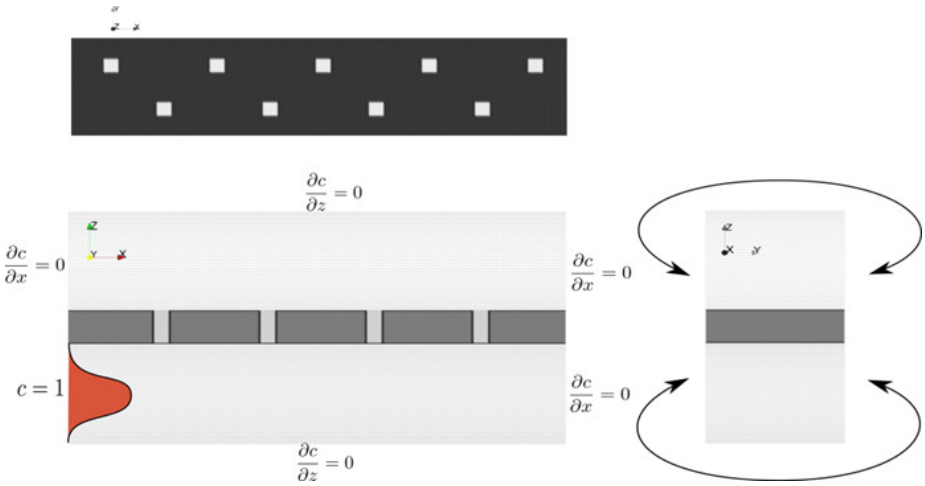

Figure 9.19: **Views of the micro-device with boundary conditions imposed to the concentration field.**

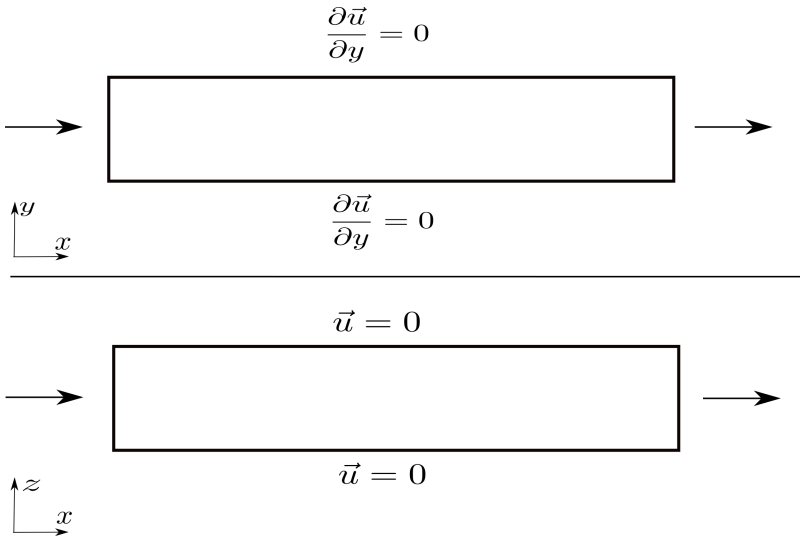

Figure 9.20: **Views of the micro-device with boundary conditions imposed to the velocity field in both channels.**

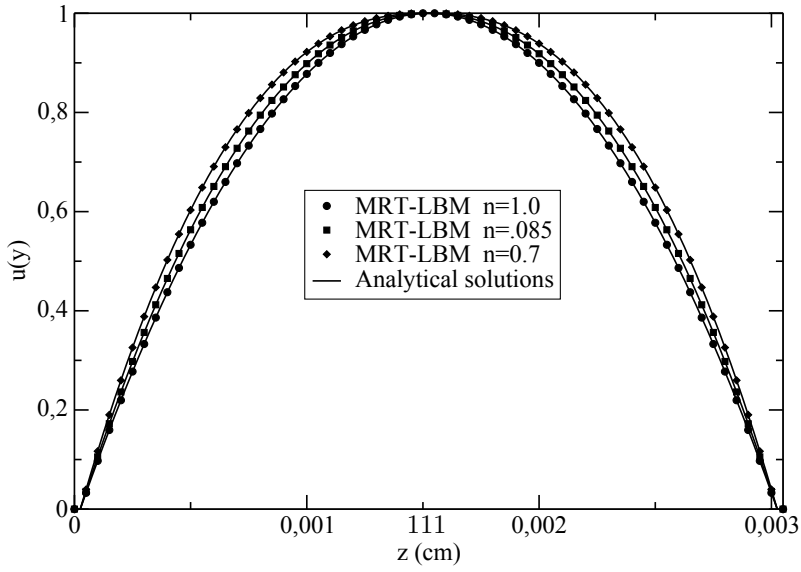

Figure 9.21: **Normalized velocity profiles in the middle of the permeate channel (fluid 1 channel) for different values of n.**

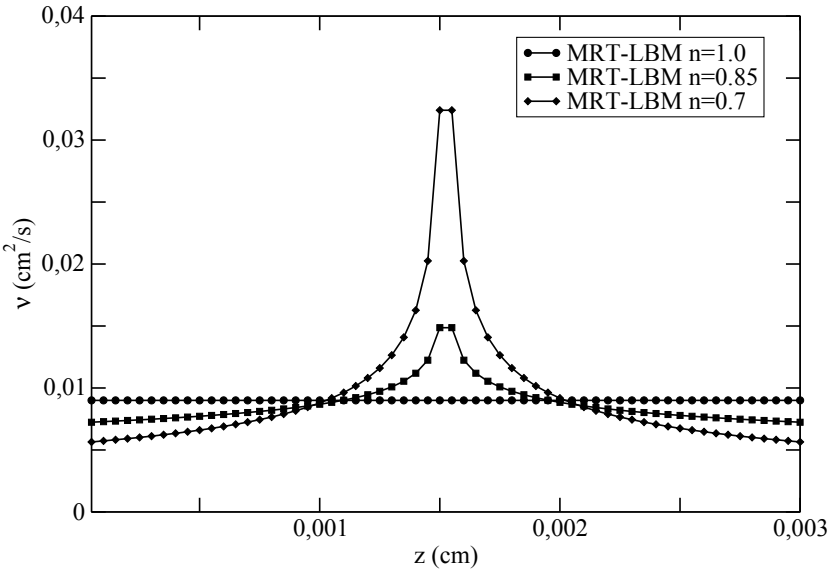

Figure 9.22: **Viscosity profiles in the middle of the permeate channel (fluid 1 channel) for different values of n.**

We made simulations with two different power-law degrees for the non-Newtonian fluid 1, $n = 0.70$ and 0.85, as well as a simulation with $n = 1.0$ (Newtonian fluid 1). Fluid 2 was considered Newtonian in all cases. As one can see in Fig. 9.21 and Fig. 9.22, the velocity and viscosity profiles across the permeate channel (fluid 1) are reproduced according to the bi-dimensional theory, because the simulations correspond to the central part of the micro-device where there is not influence of the rear and front walls over the flow.

A constant concentration $c = 1$ is imposed at the inlet of the lower channel (feed channel). The concentration for different values of the Péclet number is shown in Fig. 9.23 when the mass transfer across the membrane reaches the steady

state. As in the two-dimensional case, the convection process has a major relevance for high values of the Péclet number, sweeping the material towards the outlet and hindering diffusion along the vertical direction.

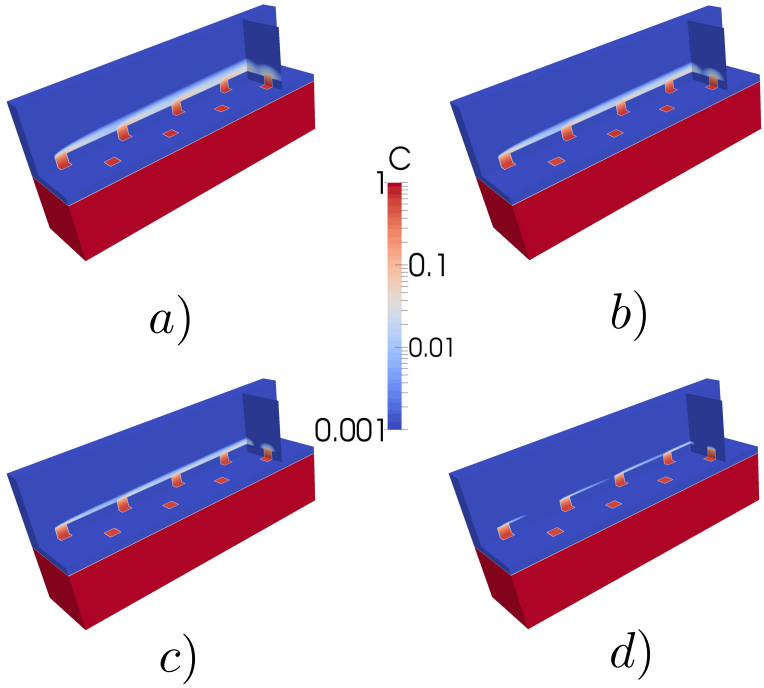

Figure 9.23: **Concentration field for a)** $Pe = 1000$**, b)** $Pe = 2000$**, c)** $Pe = 5000$**, d)** $Pe = 10000$ **in the permeate channel, and Newtonian fluid flow** ($n = 1.0$) **in both channels.**

In Fig. 9.25 (left), we show the concentration profiles just above the membrane pores in the permeate channel, for different values of the Péclet number (see line 3 of Fig 9.24). The higher the Péclet number, the lower the peaks of the concentration. This is due to the convective forces exerted by the fluid, stronger than the diffusive transport when the Péclet number increases. The mass transport inside the pore is only a diffusive process; the concentration gradient across the membrane depends only on the difference of diffusivities between both channels

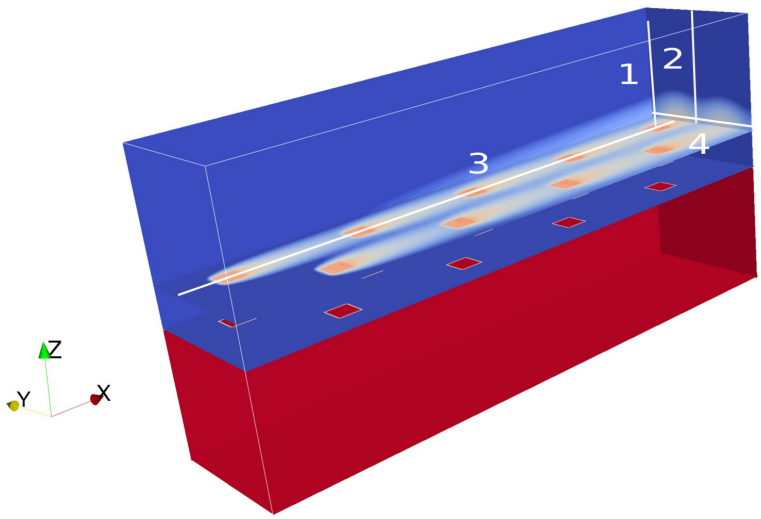

Figure 9.24: **Scheme of the three-dimensional parallel-flow micro-device indicating the cuts selected for plotting the data.**

(see 9.25 right).

We plot in Fig. 9.26 the concentration profiles at the outlet of the permeate channel. Along line 2 of Fig 9.24), the concentration decreases with height, and also with increasing the Péclet number, Fig. 9.26 (left). Two peaks of concentration are observed along line 4 of Fig 9.24, see Fig. 9.26 (right). The difference in the values of the concentration peaks is due to the interleaved distribution of the pores. This difference is reduced when the Péclet number increases. The convection forces generated by the flux do not facilitate the mass transport in the z-axis, and for high Péclet numbers the fluid quickly drags the substance towards the outlet.

The correlations found for different values of the non-Newtonian fluid index n in the permeate channel are (see figure 9.27):

$$< Sh >= 30.367(Pe\,H/L)^{0.32(6)} \quad \text{for} \quad n_{fluid_1} = 0.7, \tag{9.3}$$

$$< Sh >= 31.002(Pe\,H/L)^{0.31(9)} \quad \text{for} \quad n_{fluid_1} = 0.85, \tag{9.4}$$

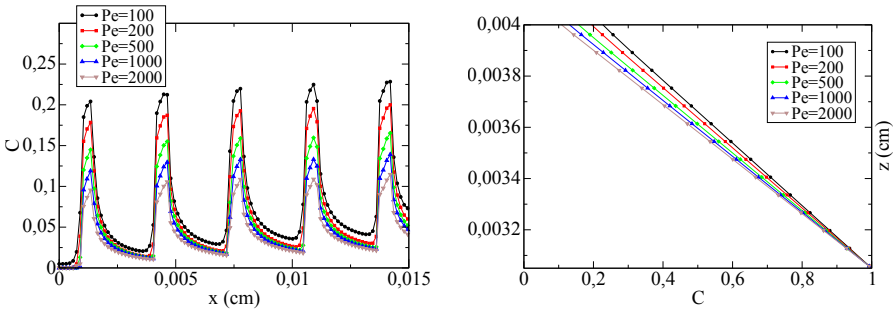

Figure 9.25: **Concentration profiles for different Péclet numbers along the x-axis, just above the pores in the permeate channel (left), and inside the pore (right).**

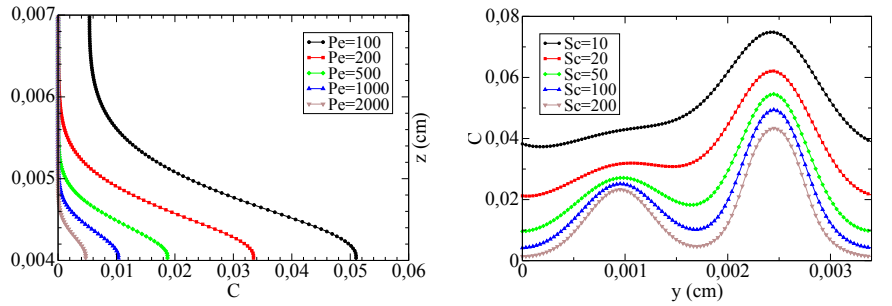

Figure 9.26: **Concentration profiles for different Péclet numbers at the outlet of the permeate channel, along line 2 of Fig. 9.24 (left), and along line 4 (right).**

$$< Sh >= 30.998(Pe\,H/L)^{0.31(5)} \quad \text{for} \quad n_{fluid_1} = 1.0, \tag{9.5}$$

There is a slight although systematic increase of the correlation exponent as the

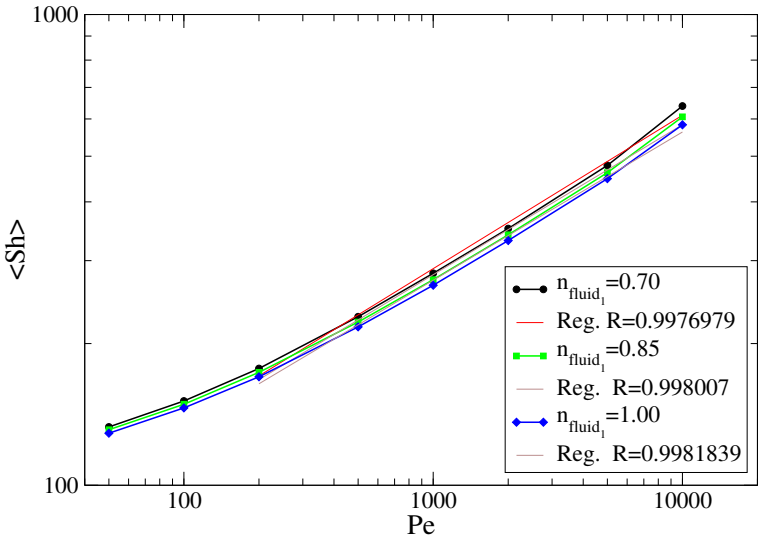

Figure 9.27: **Péclet vs Sherwood for different values of the non-Newtonian fluid index n in the permeate channel, with $n = 1.0$ in the feed channel.**

value of n in the permeate channel goes below 1. We found an increase of around 5% in the mass transfer when the fluid has a value of $n = 0.7$ as compared to $n = 1.0$, for $500 < Pe < 10000$. The different non-Newtonian fluids in the feed channel (liquid channel) have no relevance in the mean Sherwood results when the system reaches the steady state. We expect to find more differences when the transient part of the system is studied.

Chapter 10

Conclusions and Remarks

In the following sections we resume the most relevant conclusions of the thesis and provide some remarks derived from this work.

A hybrid LBM-FD Fortran90 code with a non-uniform grid that simulates mass transfer processes in non-Newtonian flows has been developed. To implement a robust and stable model which is able to simulate mass transport processes in complex fluids, significant modifications were made to the conventional models (LBM and L-W method).

On the one hand, the conventional LBM is used to reproduce the isothermal and quasi-compressible Navier-Stokes equations with a constant kinematic viscosity value (Newtonian Flows). LBM is well suited for the calculation of local shear rates, as compared with other numerical methods. A module which computes the local kinematic viscosity from the local shear rate at each time step, was developed to reproduce the non-Newtonian flow behavior. There are several mathematical expressions to model the properties of this kind of flows. For simplicity, we focused our study in the reproduction of the blood flow using the well-known truncated power-law model, but the code can be easily modified to reproduce any non-Newtonian fluid model. Additionally, since the kinematic viscosity is directly related with the relaxation parameter, an improved LBM (MRT-LBM) routine that provides stability and accuracy in a wide range of viscosities was implemented.

Force and velocity-driven truncated power-law flows were simulated in a two-

dimensional rectangular channel. In the steady state case, mechanical properties like velocity, shear rate, stress tensor, among others, show a good agreement with the analytical solutions. The force-driven flow implementation shows a second order convergence, and exhibits a fully-developed flow solution along the channel (there is no transition zone). The length of the transition zone is not a constant for Non-Newtonian fluids in the velocity-driven flow case. Flows with high shear-thinning behavior ($n \to 0$) have a faster convergence, producing smaller transition zones. In the dependent-time case, a pulsatile flow was reproduced implementing an oscillating body force over the fluid. A $D3Q19$ MRT-LB model was used to simulate the flow in a 3D tube and in a 3D rectangular channel for different power-law fluids. We tested the capability of the model to reproduce three-dimensional flows, and the results showed good agreement with the analytical solutions.

The Lax-Wendroff method was used to simulate heat and mass transfer processes solving the advection-diffusion equation. The advection-diffusion of a Gaussian pulse and the heat transfer in a moving bar were reproduced to validate the method. The results obtained in both problems show a good agreement with exact solutions. A uniform grid was used in both cases, in order to have a proper understanding of the method performance.

A LBM-FD hybrid routine which is able to couple LBM and L-W methods was built. Unlike the LBM grid, the finite differences model is implemented in a non-uniform grid. A geometric series was used to have better resolution in the regions with larger concentration gradients, seeking better stability and accuracy at high Péclet numbers. The use of two different grids makes it necessary an interpolation of the velocity data obtained by the LBM to be used into the L-W method. The LBM-FD hybrid code was validated solving the Graetz-Leveque problem of boundary layer mass flux. Simulations were performed for different values of the Péclet number and the mass transfer was measured through the mean Sherwood number along the catalyst boundary. We used three different common ratios $r = 1.0, 1.05, 1.1$ to test the advantages of the non-uniform grid implementation. The results were compared with the Holzbecher study [21], and a good concordance was obtained in the mean Sherwood number for a range of Péclet numbers. Only the highest refinement ($r = 1.1$) was capable to reproduce accurate results for $\mathrm{Pe} \gtrsim 10^6$, which showed the advantages of a non-uniform grid.

As a first application, the LBM-FD hybrid model was used to simulate the

mass transport in a 2D upper membrane wall channel. In the steady state case, three power-law blood experimental parameters cases were used (Kim et.al. [51], Walburn and Schneck [57] and Liepsch and Moravec [32]) in the constant velocity-driven flow simulations. Once the velocity field reached the steady state, a constant concentration was continuously entered through the pores into the channel. The largest difference found in the mean Sherwood number between the Newtonian flow and the three blood parameters cases was close to 5% for case 3. This case had the most prominent shear-thinning behavior. For the blood parameters used in this work, the relative difference found in the mass transport was small (5%), because the magnitude and the shape of the velocity profiles were not too different from the Newtonian flow profiles.

With an oscillatory velocity-driven pulsatile flow, the differences between Newtonian flow ($n = 1$) and a power-law ($n = 0.828$) flow are more significant at intermediate velocity amplitudes (intermediate phases of the oscillation period). We could observe that the velocity-driven method produces less uniform profiles as compared with the force-driven method when simulating pulsatile flows. The material diffusion in the direction of the flow was not affected, because the flow was periodic. In the transverse direction, the mean Sherwood number converged to the same value for all Péclet numbers, the only difference being the time that each simulation needed to reach a constant value. The study and characterization of the transient local Sherwood number across the membrane is proposed as a future work to have a complete understanding of the mass transfer in this system.

Finally, the LBM-FD hybrid model was applied to simulate the mass transport through a hydrophobic micro-porous membrane between a co-current flow passing through rectangular channels, inspired by the micro-device used in Lung-On-a-Chip research. The code was used to perform a parametric study to find the empirical correlation between the Péclet number in the permeate channel and the mass transfer across the membrane characterized by the mean Sherwood number. The mean Sherwood number increased with the Péclet number in the permeate channel. The correlations in the two-dimensional micro-device confirmed the linear scaling of $< Sh >$ with the number of pores. The correlations gave the value 1/3 (similar to the corresponding parameter of the Graetz-Leveque problem) for the scaling exponent of the average Sherwood number with Pe, in both 2D and 3D models.

In the three dimensional micro-device, we found an increase of about 5% for

$n = 0.7$ in the steady-state mass transfer, as compared with the Newtonian fluid case ($n = 1.0$). Only the steady regime was studied, and only for a non-Newtonian power-law fluid in the permeate section of the device. We expect to find significant differences when the transient part is studied.

Bibliography

[1] S. Corneyb B. M. Johnston, P. R. Johnstona and D. Kilpatrick. Non-newtonian blood flow in human right coronary arteries: steady state simulations. *J. Biomech.*, 37:709–720, 2004.

[2] G. K. Batchelor. *An introduction to fluid dynamics.* Cambridge university Press, Cambridge, 2000.

[3] D. R. J. Owen C. R. Leonardi and Y. T. Feng. Numerical rheometry of bulk materials using a power law fluid and the lattice boltzmann method. *J. Non-Newton. Fluid*, 66(12-13):628–638, 2011.

[4] C. Cercignani. *Mathematical methods in kinetic theory.* Plenum, 1990.

[5] H. Chen and W. H. Mathaeus. New cellular automaton model for magnetohydrodynamics. *Phys. Rev. Lett.*, 58:1845, 1987.

[6] R. P. Chhabra and J. F. Richardson. *Non-Newtonian flow and applied rheology: engineering applications.* Elsevier, Oxford, 2011.

[7] S. Chien. Shear-dependent deformation of erythrocytes in rheology of human blood. *Am. J. Prhysiol.*, 219:136–142, 1970.

[8] Y. I. Cho and K. R. Kensey. Effects of the non-newtonian viscosity of blood on flows in a diseased arterial vessel. part i: Steady flows. *Biorheol.*, 28:241–262, 1991.

[9] T. J. Chung. *Computational fluid dynamics.* Cambridge University Press, 2010.

[10] M. Krafczyk P. Lallemand D. d'Humieres, I. Ginzburg and L. S. Luo. Multiple relaxation-time lattice boltzmann models in three dimensions. *Phil. Trans. R. Soc. A*, 360(1792):437–451, 2002.

[11] A. Mammoto M. Montoya-Savala H. Y. Hsin-D. E. Ingber. D. Huh, B. D. Matthews. Reconstituing organ-level lung functions on a chip. *Science*, 328:1662–1668, 2010.

[12] J. G. Georgiadis D. J. Holdych, D. R. Noble and R. O. Buckius. Truncation error analysis of lattice boltzmann methods. *J. Comput. Phys.*, 193(2):595–619, 2004.

[13] L. Dintenfass. *Blood microrheology: viscosity factors in blood flow, Ischaemia and Thrombosis*. Butterworth, London, 1971.

[14] B. Belaissaoui E. Chabanon and E. Favre. Gas-liquid separation processes based on physical solvents: opportunities for membranes. *J. Membr. Sci.*, 459:52–61, 2014.

[15] A. Lautenschleger E. Y. Kenig, Y. Su and M. Grünewald. Micro-separation of fluid systems: A state-of-the-art review. *Sep. Purif. Technol.*, 120:245–264, 2013.

[16] Y. C. Fung. *Biomechanics: Mechanical properties of living tissue*. Springer, New York, 1993.

[17] C. G. Garo. Vascular fluid dynamics and vascular biology and disease. *Math. Methods appl. Sci.*, 24(17-18):1311–1324, 2001.

[18] I. Ginzburg. Truncation errors, exact and heuristic stability analysis of two-relaxation-times lattice boltzmann schemes for anisotropic advection-diffusion equation. *Commun. Comput. Phys.*, 11:1439, 2012.

[19] X. He and L. S. Luo. Theory of the lattice boltzmann method: From the boltzmann equation to the lattice boltzmann equation. *Phys. Rev. E*, 56:6811–6817, 1997.

[20] M. Hecht and J. Harting. Implementation of on-site velocity boundary conditions for d3q19 lattice boltzmann simulations. *J. Stat. Mech. Theory Exp.*, page P01018, 2010.

[21] E. Holzbecher. Numerical solutions for the leveque problem of boundary layer mass or heat flux. *Excerpt from the Proceedings of the COMSOL Conference Hannover*, 2008.

[22] K. Huang. *Statistical mechanics*. John Wiley & sons, 1987.

[23] J. Buick J. Boyd and S. Green. Analysis of the casson and carreau-yasuda non-newtonian blood models in steady and oscillatory flows using the lattice boltzmann method. *Phys. of Fluids*, 19:093103, 2007.

[24] M. Perić J. H. Ferziger. *Computational methods for fluid dynamics.* Springer, 1997.

[25] O. Malaspinas M. Deville A. Michler J. Latt, B. Chopard. Straight velocity boundaries in the lattice boltzmann method. *Phys. Rev. E*, 77:056703, 2008.

[26] R. Wilson J. Welty, C. Wicks and G. Rorrer. *Fundamentals of momentum, heat, and mass transfer.* John Wiley & Sons, Inc., 2000.

[27] W. Dzwinel K. Boryczko and D. A. Yuen. Dynamical clustering of red blood cells in capillary vessels. *J. Mol. Model.*, 9:16–33, 2003.

[28] A. Quarteroni L. Formaggia and A. Veneziani. *Cardiovascular mathematics: Modeling and simulation of the circulatory system.* Springer, Italy, 2009.

[29] D. Gland H. Auradou L. Talon, D. Bauer and I. Ginzburg. Assessment of the two relaxation time lattice-boltzmann scheme to simulate stokes flow in porous media. *Water Resour. Res.*, 48:W04526, 2012.

[30] A. J. C. Ladd. Numerical simulations of particulate suspensions via a discretized boltzmann equation. *J. Fluid Mech.*, 271:285, 1994.

[31] L. D. Landau and E. M. Lifshitz. *Fluid mechanics.* Pergamon Press, Oxford, 1987.

[32] D. Liepsch and St. Moravec. Pulsatile flow of non-newtonian fluid in distensible models of human arteries. *Biorheol.*, 21:571–586, 1984.

[33] D. O. Lowe. *Clinical blood rheology, Vol I, II.* CRC Press, Boca Raton, 1998.

[34] S. A. Marzouk M. A. Al-Zarooni M. Al Marzouqi, M. H. El-Naas and N. Abdullatif. Modeling of co2 absorption in membrane contactors. *Sep. Purif. Technol.*, 59:286–293, 2008.

[35] A. Mezrhab-J. P. Fontaine M. Jami, F. Moufekkir and M. Bouzidi. New thermal mrt lattice boltzmann method for simulations of convective flows. *Int. J. Therm. Sci.*, 100:98–107, 2016.

[36] Marco Domenico Mazzeo. *Lattice-Boltzmann Simulations of Cerebral Blood Flow*. PhD thesis, University College of London, 2009.

[37] S. Melchionna, D. Moroni, J. P. Hansen, and S. Succi. On the use of lattice fokker-planck models for hydrodynamics. *Europhysics Letters*, 75(3):399–405, 2006.

[38] M. Mendoza. Modelos de lattice-boltzmann para electrodinámica y magnetohidrodinámica. Master's thesis, Universidad Nacional de Colombia, 2007.

[39] A. A. Mohamad and S. Succi. A note on equilibrium boundary conditions in lattice boltzmann fluid dynamic simulations. *Eur. Phys. J.*, 171:213, 2009.

[40] J. Mu˘zík. Boundary knot method for convection-diffusion problems. *Procedia Engineering*, 111:582–588, 2015.

[41] De Leon N. and De Leon M. N. Aerodynamic simulation of indoor flight. *Eur. J. Phys.*, 28:255–265, 2007.

[42] Lockard D. P., Luo L. S., and Singer B. A. Evaluation of the lattice-boltzmann equation solver powerflow for aerodynamic aplications. Technical report, NASA/CR-2000-210550ICASE Report No. 2000-40, 2000.

[43] T. N. Phillips and G. W. Roberts. Lattice boltzmann models for non-newtonian flows. *IMA J. Appl. Math.*, 76(5):790–816, 2011.

[44] A. Puig Aranega. *Review of boundary conditions and investigation towards the development of a growth model: a lattice Boltzmann method approach.* PhD thesis, Universitat Rovira i Virgili, 2016.

[45] Y. L. He Q. Liu and Q. Li. Multiple-relaxation-time lattice boltzmann modeling of incompressible flows in porous media. *Physica A*, 429:215–230, 2015.

[46] Y. H. Qian, D. d'Humieres, and P. Lallemand. Lattice bgk models for navier-stokes equation. *Europhys. Lett.*, 17(6):479, 1992.

[47] W. Shyy R. Mei, D. Yu and L. S. Luo. Force evaluation in the lattice boltzmann method involving curved geometry. *Phys. Rev. E*, 65:041203, 1995.

[48] D. C. Rapaport. *The art of molecular dynamics simulation.* Cambridge University Press, 2004.

[49] J. A. Robson. *A finite element approximation of non-Newtonian flow.* PhD thesis, University of Manchester, 2003.

[50] S. Chen-G. Doolen S. Hou, Q. Zou and A. C. Cogley. Simulation of cavity flow by the lattice boltzmann method. *J. Comput. Phys.*, 118:329, 1995.

[51] A. H. Jeon B. Hogenauer S. Kim, Y. I. Cho and K. R. Kensey. A new method for blood viscosity measurement. *J. Non-Newtonian Fluid Mech.*, 94:47–56, 2000.

[52] R. Skalak and S. Chien. Theoretical models of rouleaux formation and dissagregation. *Ann. N. Y. Acad. Sci.*, 416:138–148, 1983.

[53] M. C. Sukop and D. T. Thorne. *Lattice Boltzmann modeling: An introduction for geoscientists and engineers.* Springer, New York, 2006.

[54] A. Kuzmin O Shardt G. Silva T. Kruger, H. Kusumaatmaja and E. M. Viggen. The lattice boltzmann method: Principles and practice. *Commun. Comput. Phys.*, 11:1439, 2012.

[55] F. Varnik T. Kruger and D. Raabe. Shear stress in lattice boltzmann simulations. *Phys. Rev. E*, page 046704, 2009.

[56] W. T. Vetterling W. H. Press, S. A. Teukolsky and B. P. Flannery. *Numerical Recipes in C.* Cambridge University Press, 1992.

[57] F. J. Walburn and D. J. Schneck. A constitutive equation for whole human blood. *Biorheol.*, 13:201–210, 1976.

[58] C. H. Wuang and J. R. Ho. A lattice boltzmann approach for the non-newtonian effect in the blood flow. *Comput. Math. Appl.*, 62:75–86, 2011.

[59] J. G. Zhou. *Lattice Boltzmann methods for Shallow Water Flows.* Springer, 2003.

[60] Q. Zou and X. He. On pressure and velocity boundary conditions for the lattice boltzmann bgk model. *Phys. Fluids*, 9(6):1591–1598, 1997.

UNIVERSITAT ROVIRA I VIRGILI
NUMERICAL STUDY OF BIO-FLUIDS AND MASS TRANSFER PROCESSES THROUGH MEMBRANES
Jonathan Florez Giraldo

UNIVERSITAT ROVIRA i VIRGILI